Correlations and Currents in ^{3}He Studied with the $(e, e'pp)$ Reaction

David L. Groep

Distributed by NIKHEF, Amsterdam
ISBN 90-6488-013-1

Correlations and Currents in ^{3}He Studied with the $(e, e'pp)$ Reaction

Correlaties en stromen in ^{3}He
onderzocht met de $(e, e'pp)$ reactie

(met een samenvatting in het Nederlands)

Proefschrift ter verkrijging van de graad van doctor aan
de Universiteit Utrecht op gezag van
de Rector Magnificus, Prof. Dr. H.O. Voorma,
ingevolge het besluit van het College voor Promoties
in het openbaar te verdedigen op
maandag 31 januari 2000 des middags te 16:15 uur

door

David Leo Groep

geboren op 6 september 1973, te Zaandam

Promotor:	Prof. Dr. P.K.A. de Witt Huberts Faculteit der Natuur– en Sterrenkunde
Copromotor:	Dr. E. Jans NIKHEF

ISBN: 90-6488-013-1

The work described in this thesis is part of the research programme of the "Stichting voor Fundamenteel Onderzoek der Materie (FOM)", which is financially supported by the "Nederlandse Organisatie voor Wetenschappelijk Onderzoek (NWO)"

This work was sponsored by the Stichting Nationale Computerfaciliteiten (National Computing Facilities Foundation, NCF) for the use of supercomputer facilities, with financial support from the Nederlandse Organisatie voor Wetenschappelijk Onderzoek (Netherlands Organization for Scientific Research, NWO).

Contents

I Introduction

At the femtometre length scale, the atomic nucleus can be adequately described as a system of protons and neutrons without having to regard their substructure. The strong interactions which at energy scales above a few GeV have to be described in terms of the nucleonic constituents, *i.e.*, quarks and gluons, can in the case of the present experiment be treated in terms of effective interactions between nucleons, mesons and Δ isobars. The two-body part of the nucleon-nucleon (NN) interaction provides the dominant part of the binding in nuclei. It has a complicated structure, depending, *e.g.*, on the value and relative orientation of spin and isospin of the interacting nucleons, that is attractive at distances above approximately 1 fm, but strongly repulsive at short inter-nucleon distances. The long-range behaviour can be theoretically described by the exchange of a single pion, while the correlated exchange of multiple mesons is used in the description of the intermediate-range part. The short-range part has to be treated in a phenomenological way, either explicitly or described by exchange of heavier mesons like ρ and ω with phenomenological form factors, since at this scale the description of the nucleus in terms of nucleons and mesons is no longer adequate and a theoretical treatment based on quantum chromodynamics is not available. The use of a realistic NN interaction induces correlations among the nucleons in the nuclear wave function.

Several potential models of the NN interaction are available describing the deuteron binding energy and the phase shifts deduced from nucleon-nucleon scattering experiments with a χ^2 per datum of approximately one, *i.e.*, they are phase-shift equivalent. The Bonn potential model [Mac89] is based on the exchange of single and multiple mesons. Since its energy dependence poses difficulties in many-body calculations, derived forms like the Bonn-B interaction are commonly used. The Bonn-B model is constructed in momentum space and is non-local at scales around the nucleons Compton wavelength when expressed in coordinate space (*i.e.*, it contains 'instantaneous' interactions of spatially separated particles). Recently, a new, charge-dependent model CD-Bonn [Mac96] was introduced which provides a better fit to the existing NN scattering data. The Argonne v_{18} potential [Wir95] also uses one-pion exchange for the description of the long-range part, but employs a completely local description. The intermediate- and short-range parts have a more phenomenological nature and the non-local character of the potential is limited. The interactions developed by the Nijmegen group [Sto94] are also local in the description of the one-pion exchange. Of the various models, Nijmegen-II is entirely local and Nijmegen-I and -93 are only mildly non-local in the short- and intermediate-range part. Thus, although close to equivalent in the description of NN scattering data, the models for the two-body interaction describe both long- and especially short-range characteristics in a different way.

Exact calculations of nuclear ground-state properties, based on the aforementioned NN interaction models, are currently possible for $A \leq 7$ [Car98], while in heavier nuclei approximations have to be made. Exact calculations are feasible for breakup reactions in which no more than three nucleons are involved and for energies below approximately 350 MeV [Glö96]. The study of nuclear ground-state properties like, *e.g.*, the binding energy of three-nucleon systems, already provides a means to study the characteristics of the NN interaction; calculations of the triton binding energy reveal differences of up to 375 keV between the various potential models [Nog97] and a discrepancy of 530–900 keV with the experimental value. Additional binding of the triton is provided by the introduction of three-nucleon forces, *e.g.*, based on $\pi - \pi$ exchange, of which the strength is adjusted depending on the NN interaction used.

Exclusive nuclear-breakup processes and the investigation of spin degrees-of-freedom offer more possibilities for the investigation of the structure and dynamics of the few-nucleon systems, as they are sensitive to, *e.g.*, short-range features or small components of the nuclear wave function. They are also sensitive to the off-shell behaviour of the NN interaction, *i.e.*, the total energy of the nucleons involved in the reaction is not the same in the final state and the initial state, something that cannot be probed by elastic nucleon-nucleon scattering experiments. Electron- and photon-induced breakup of the few-nucleon system is suited for such studies, as the electromagnetic part of the interaction is well known. In addition, the use of virtual photons offers the possibility to vary independently the energy and momentum transfer to the system and to use the longitudinal polarization of the virtual photon.

Experimental studies of electromagnetically-induced two-body and three-body breakup of the three-nucleon system have mainly been performed on ^{3}He, because of the experimental difficulties associated with the use of tritium. The experiments include the electron-induced two-body breakup reaction $^3\mathrm{He}(e,e'p)d$ [Jan87, Kei87, Mar88, Duc93, LeG97, Flo99] and the semi-inclusive three-body breakup $^3\mathrm{He}(e,e'p)pn$ [Jan87, Mar88, LeG97, Flo99]. Also two-body breakup experiments of the type $^3\mathrm{He}(e,e'd)p$ have been performed [Kei85, Kei87, Tri96, Spa98]. In these experiments, momentum distributions were obtained up to 500 MeV/c, while at 90 and 260 MeV/c also a longitudinal-transverse separation was performed. Although the cross section is strongly influenced by contributions from meson-exchange currents and final-state rescattering, signatures of NN correlations were observed in these studies for momenta above 300 MeV/c. The proton-proton density distribution was extracted for relative momenta from 200 to 550 MeV/c in a model-dependent analysis of inclusive $^3\mathrm{He}(e,e')$ data by Beck [Bec90].

Exclusive $^3\mathrm{He}(\gamma,p)d$ [Isb94] and semi-inclusive $^3\mathrm{He}(\gamma,p)pn$ [Hos89] reactions were performed using bremsstrahlungs photons. Also photon-induced exclusive three-body breakup, $^3\mathrm{He}(\gamma,pp)n$, was investigated in detail. Measurements by Audit *et al.* [Aud89, Aud91] were performed in a kinematic domain selected to emphasize the production of on-shell pions on the struck nucleon that are subsequently reabsorbed on the nucleon pair. The results were evaluated in a theoretical framework based on a diagrammatic expansion of the reaction amplitude [Lag85]. These measurements indicate an important role for two-step processes in which three nucleons are involved, in particular sequential pion exchange. Such processes were also observed at lower energy transfers, in which the initial pion is assumed to propagate off-shell [Sar93].

The use of tagged photon beams opened the possibility of kinematically complete measurements of the full breakup cross section. Measurements with the large-solid-angle detector DAPHNE [Aud97], again in the Δ resonance region, showed that the cross section for photon-induced breakup at $E_\gamma < 500$ MeV is dominated by two-step three-nucleon processes in those regions of phase space where final-state rescattering effects are minimal. No neutron momentum distribution could be extracted from this dataset. The role of three-nucleon mechanisms was also identified by Kolb *et al.* [Kol96] at lower photon energies. Neutron momentum distributions extracted by Emura *et al.* [Emu94a, Emu94b] in the Δ resonance region (E_γ=200–500 MeV) showed that both two-nucleon and three-nucleon photo-absorption mechanisms are needed to explain the data, but that at low neutron momentum the two-nucleon processes dominate the cross section. Due to the choice of the kinematic domain and the transverse nature of the probe used in these experiments, the absorption of the photon by a two-proton pair observed at low neutron momentum cannot be uniquely attributed to knockout induced by one-body hadronic currents.

The $(e, e'pp)$ reaction provides a tool to investigate the role of NN correlations inside nuclei. At intermediate electron energies, the reaction amplitude is driven by several processes. Firstly, coupling of the virtual photon to one nucleon – described by a one-body hadronic current – can lead to emission of two nucleons due to initial-state correlations. Secondly, two-body hadronic currents, like coupling to mesons (meson-exchange currents or MECs) and excitation of the Δ in an intermediate state, will contribute to the cross section. Also final-state rescattering will give contributions to the cross section. The detection of two protons in the final state has the advantage that it allows measurement of those regions in phase space where the neutron, which remains undetected, has a low momentum and can thus be considered as a spectator particle. In such a 'direct' reaction on a proton-proton pair, the contribution from meson-exchange currents is suppressed since – to first relativistic order – the photon does not couple to the uncharged mesons involved. Also the contribution of Δ excitation is reduced because of angular momentum and parity conservation selection rules.

Study of the momentum transfer dependence of the cross section can be used to investigate the coupling mechanism of the virtual photon to a pair of nucleons. The energy transfer should then be chosen such that the influence of intermediate Δ excitation to the cross section is reduced, *i.e.*, well below the invariant mass of the $N\Delta$ system at 2170 MeV/c^2, but sufficiently high to emit two protons from the nucleus with enough kinetic energy to pass the detector thresholds. On the other hand, variation of the energy transfer allows investigation of meson-exchange and isobar contributions to the cross section.

Preferably, measurements should be performed over a large domain in relative and centre-of-mass momenta of the nucleons involved. Together with knowledge on the reaction mechanism this may provide insight in the bound-state wave function of the ^{3}He nucleus for specific values of relative and centre-of-mass momenta. A detailed comparison with the results of calculations, based on different models of the NN interaction, can subsequently be made.

The recent advance of high duty-cycle electron accelerators has made possible the three-fold coincidence experiments necessary to measure exclusive electron-induced two-nucleon knockout. Experiments aiming at the study of NN correlations by means of the $(e, e'pp)$ reaction were pioneered with the ^{12}C$(e, e'pp)$ experiments by Zondervan *et al.* [Zon95] and Kester *et al.* [Kes95]. Measurements performed by Onderwater *et al.* [Ond98a] at the Amsterdam Pulse Stretcher AmPS facility using large-solid-angle proton detectors revealed signatures of short-range correlations in the ^{16}O$(e, e'pp)^{14}$C reaction. Similar results were obtained with a three-spectrometer setup at the Mainz Microtron MAMI [Ros97]. Experimental evidence for short-range correlations was obtained from the study of the ^{16}O$(e, e'pp)^{14}$C$_{\mathrm{g.s.}}$ reaction at various energy transfer values by Starink *et al.* [Sta99a].

In this work measurements of exclusive electron-induced two-proton knockout on ^{3}He are discussed. Chapter 2 is devoted to a description of the kinematics of the ^{3}He$(e, e'pp)$ reaction and discusses calculations of the cross section based on the continuum Faddeev technique employed by Golak *et al.* [Gol95]. Here, also the numerical methods necessary to compare the calculations to data are discussed. The experimental setup is described in chapter 3, where also an overview of the measured kinematic settings is given. The analysis of the data is described in chapter 4. In chapter 5 the extracted cross sections are presented and compared to the results of the continuum Faddeev calculations. The work ends with a summary and an outlook.

II Theory

The kinematics of the electron-induced three-body breakup reaction of ^{3}He and the relevant physics observables are discussed. Interpretation of the measured cross sections requires comparison with predictions of a theoretical model. In this chapter, the model developed by Golak *et al.* [Gol95] is introduced and the procedure developed to compare results of this model to data is detailed.

2.1 Kinematics of electron-induced ^{3}He breakup

In the exclusive electron-induced two-nucleon knockout reaction, energy and momentum are transferred to a nucleus by a virtual photon. After the reaction the momenta of the scattered electron and the emitted nucleons are determined. The remainder of the nucleus is left intact and no secondary particles are created. This reaction mechanism is schematically shown in Fig. 2.1. The energy transfer ω and three-momentum transfer $\boldsymbol{q}$ is calculated from the momentum difference between the incoming and scattered electron. If the electron mass is neglected, as it is much smaller than its energy E, then we can define $\omega \equiv E_e - E_{e'} = c(p_e - p_{e'})$ and $\boldsymbol{q} = \boldsymbol{p}_e - \boldsymbol{p}_{e'}$.

In the present $^3\text{He}(e, e'pp)$ experiment the two protons, with momenta $\boldsymbol{p}'_1$ and $\boldsymbol{p}'_2$, resulting from the full breakup of ^{3}He are detected. As no particles are created, the final state can be reconstructed completely and the missing momentum $\boldsymbol{p}_m = \boldsymbol{q} - \boldsymbol{p}'_1 - \boldsymbol{p}'_2$ can be identified with the momentum of the undetected neutron $\boldsymbol{p}'_3$. Energy conservation requires the missing energy E_m to be equal to the binding energy E_b of the ^{3}He nucleus: $E_m = \omega - T_1 - T_2 - T_{rec} = E_b$, where T_{rec} is the kinetic energy of the recoiling neutron, which can be calculated from $\boldsymbol{p}_m$, T_1 and T_2 being the kinetic energies of the two emitted protons. The binding energy of ^{3}He is 7.718 MeV [Til87].

As the direction of the virtual-photon momentum defines a natural direction of preference, it is convenient to describe the scattering process in a coordinate

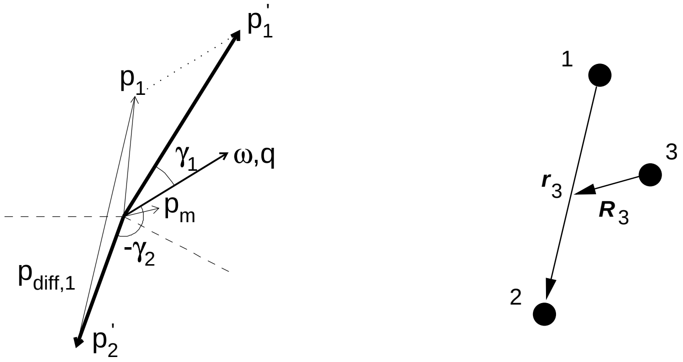

Figure 2.1: *Kinematic configuration of an* $(e, e'pp)$ *reaction. For clarity, the momentum vectors are shown all in one plane. The dashed lines represent the incoming and scattered electron; the bold vectors detected protons and the thin vectors derived quantities. Coupling of the photon to proton–1 has been assumed. The right-hand figure shows the Jacobi coordinates in the three-body system.*

system in which a vector $\boldsymbol{p}$ is expressed as $\boldsymbol{p} = (p, \gamma, \zeta)$, where γ represents the polar angle between the momentum of the particle and the momentum transfer $\boldsymbol{q}$. The angle ζ is defined as the angle between the electron scattering plane and the plane containing both $\boldsymbol{p}$ and $\boldsymbol{q}$. For clarity the prime is dropped from the angles γ and ζ; hence, γ_1 is the angle between $\boldsymbol{q}$ and $\boldsymbol{p}_1'$. For convenience, proton–1, of which the momentum vector has the smallest angle with respect to $\boldsymbol{q}$, is labelled 'forward', and the second proton 'backward'.

In the description of three-body kinematics Jacobi coordinates are introduced as $\boldsymbol{r}_k = \boldsymbol{x}_i - \boldsymbol{x}_j$ and $\boldsymbol{R}_k = \boldsymbol{x}_k - \frac{1}{2}(\boldsymbol{x}_i + \boldsymbol{x}_j)$ as shown in Fig. 2.1 [Glö83]. The indices ijk are cyclic permutations of the particle indices 1, 2, and 3. The corresponding Jacobi momenta are then defined as[*]:

$$\boldsymbol{p}_{rel,k} = \tfrac{1}{2}(\boldsymbol{p}_i - \boldsymbol{p}_j) \quad \text{and} \quad \boldsymbol{p}_{cm,k} = \tfrac{2}{3}[\boldsymbol{p}_k - \tfrac{1}{2}(\boldsymbol{p}_i + \boldsymbol{p}_j)]. \tag{2.1}$$

---

[*] The Jacobi momenta are usually called $\boldsymbol{p}$ and $\boldsymbol{q}$, as in Ref. [Glö83]. To avoid ambiguity between the individual nucleon momenta, the three-momentum transfer and the Jacobi momenta, they are here labelled $(\boldsymbol{p}_{rel}, \boldsymbol{p}_{cm})$.

2.2 Breakup of ^{3}He by an electromagnetic probe

The interaction of an electron with ^{3}He can well be described within the one-photon exchange approximation. In this case the differential cross section for full breakup of the tri-nucleon system, in absence of spin observables, is written as

$$d\sigma^{3N}\rfloor_{lab} = \frac{1}{(2\pi)^2}\frac{E'}{E}m_e^2|M_{fi}^{3N}|^2\delta(M_t+\omega-E_1'-E_2'-E_3')\delta^3(\boldsymbol{q}-\boldsymbol{p}_1'-\boldsymbol{p}_2'-\boldsymbol{p}_3')$$
$$dE'd\Omega_e d^3\boldsymbol{p}_1' d^3\boldsymbol{p}_2' d^3\boldsymbol{p}_3', \quad (2.2)$$

where $m_e^2|M_{fi}^{3N}|^2$ is the contraction of the leptonic and hadronic tensor, the delta-functions take energy and momentum conservation into account, E is the total relativistic energy and m_e is the electron mass [Golth]. Integration over the momentum vector $\boldsymbol{p}_3'$ of the third, unobserved, particle and the momentum of the second particle p_2 yields the eight-fold differential cross section

$$\frac{d^8\sigma}{dE'd\Omega_{e'}dT_1'd\Omega_1 d\Omega_2} = \frac{1}{(2\pi)^2}\frac{E'}{E}\,m_e^2|M_{fi}^{3N}|^2\,\rho_f^{3N} \quad (2.3)$$

where ρ_f^{3N} is the phase space factor

$$\rho_f^{3N} = \frac{E_1|\boldsymbol{p}_1'|\,\boldsymbol{p}_2'^{\,2}}{\left|\frac{|\boldsymbol{p}_2'|}{E_2} - \frac{\boldsymbol{p}_2'\cdot\boldsymbol{p}_3'}{|\boldsymbol{p}_2'|E_3}\right|}. \quad (2.4)$$

The transition matrix element $|M_{fi}^{3N}|^2$ can be separated in a purely leptonic part and a sum over the product of kinematic factors and hadronic structure functions W. It can be shown on general grounds [Bof96] that in the case of two-nucleon knockout only six independent structure functions contribute to the unpolarized cross section:

$$m_e^2|M_{fi}|^2 = (2\pi)^2\frac{E}{E'}\sigma_{Mott}\sum_i v_i W_i, \quad (2.5)$$

with (α being the finestructure constant)

$$\sigma_{Mott} = \frac{\alpha^2\cos^2\frac{\theta_{e'}}{2}}{4E^2\sin^4\frac{\theta_{e'}}{2}}. \quad (2.6)$$

Four of the structure functions used in this framework are also present in single-nucleon knockout: W_{C}, W_{T}, W_{I}, and W_{S} as defined by De Forest [For83]. The

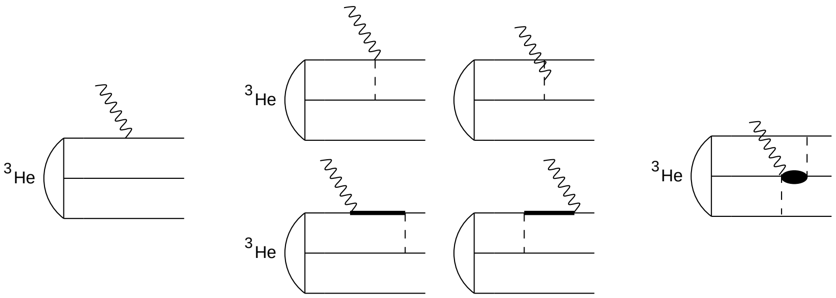

Figure 2.2: *Schematic representation of virtual-photon absorption by the* ^{3}He *nucleus. The left-hand graph shows interaction via a one-body hadronic current, the four graphs in the middle represent various two-body mechanisms: coupling to mesons and intermediate* Δ *excitation and de-excitation. An example of a three-body mechanism is shown on the right; the shaded oval represents anything except a nucleon.*

two additional structure functions contributing in $(e, e'pp)$ are arbitrarily labelled X and Y by Golak [Golth].

The structure functions W are combinations of the nuclear matrix element N^μ [Gol95],

$$N^\mu \equiv \langle \Psi^{(-)}_{scatt}(\boldsymbol{q}) | \hat{j}^\mu | \Psi_{bound}(\boldsymbol{P}) \rangle, \tag{2.7}$$

where $\Psi^{(-)}_{scatt}$ and Ψ_{bound} are fully antisymmetric solutions of the $3N$ scattering state and the initial ^{3}He bound state, respectively. The nuclear current operator $\hat{j}^\mu$ describes the coupling of the virtual photon to this bound state, making the transition to the scattering state $\Psi^{(-)}_{scatt}(\boldsymbol{q})$. In the initial state the total momentum $\boldsymbol{P}$ is zero while the total momentum of the final state equals $\boldsymbol{q}$.

Photoabsorption mechanisms

There are various ways the virtual photon can couple to the ^{3}He nucleus, some of which are depicted in Fig. 2.2.

The one-body hadronic current takes into account the absorption of a virtual photon on one nucleon only, which subsequently leads to the full breakup of the tri-nucleon system. In a non-relativistic reduction, the one-body hadronic current consists of three parts: a charge-density operator, a convection current operator – which determines the orbital magnetic moment of the nucleons – and a spin current operator, which is associated with their spin magnetic moment [Golth].

Breakup of the ^{3}He nucleus can also occur via two-body hadronic currents, thus sharing both the energy and the momentum between the two nucleons. In the energy and momentum transfer domain under study, the relevant two-body currents are coupling of the virtual photon to mesons (meson-exchange currents or MECs) and excitation of the Δ resonance in an intermediate state (isobar currents or ICs). Their importance strongly depends on the isospin of the NN pair. In the case of a pp pair the contribution of MECs to the cross section will be strongly suppressed, as the virtual photon to first relativistic order does not couple to such a pair [Giu91]. Also the contribution due to isobar currents is reduced in case the two protons are in a relative $^1S_0$ state, as the transition via the resonant M1 multipole is forbidden by angular momentum and parity conservation rules. Therefore Δ excitation is only possible via the much weaker non-resonant E1 and E2 multipoles [Wilh96]. These restrictions on MECs and ICs are not applicable to pn pairs. It may therefore be expected that in a direct $(e, e'pp)$ reaction the influence of these two-body currents is reduced compared to the $(e, e'pn)$ case.

In addition, the photon can couple to all three particles by a three-body mechanism, *e.g.*, by coupling to the simultaneous exchange of two mesons. Sensitivity to these processes will exist at photon energies around 500–600 MeV and in specific regions of phase space, where the struck meson initially propagates on-shell and is subsequently reabsorbed by the remaining nucleon pair [Bof96].

Final-state rescattering

The interaction among the three nucleons in the final state (FSI), *i.e.*, after the interaction of the virtual photon with the tri-nucleon system, can strongly influence the cross section for specific kinematic configurations. It has been convincingly shown [Meij86, Ish94] that multiple rescattering among the outgoing nucleons leads to cross sections that are significantly different compared to those calculated in a plane-wave approach. Truncation to single-rescattering

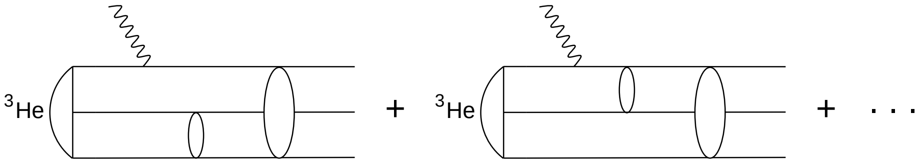

Figure 2.3: *Schematic representation of multiple-rescattering among the nucleons in the final state, following an interaction via a one-body hadronic current. The 'blobs' represent the 2N scattering operator (t-matrix).*

processes only is insufficient. A schematic representation of the rescattering process is given in Fig. 2.3.

2.3 Calculation of the breakup cross section

The differential cross section of the exclusive three-body breakup of the trinucleon system can be calculated by solving Faddeev-type equations for both the bound state and the final, 'scattering' state [Glö96, Meij86]. Alternatively, one can apply a diagrammatic approach, in which the presumably most important processes are added coherently [Lag87]. Whereas the diagrammatic approach allows inclusion of realistic two-body mechanisms, especially isobar currents, it is not suited to account for rescattering effects up to infinite order. As it has been shown in both theoretical [Meij86, Ish94] and experimental [Poo99] studies, that higher-order rescattering can have a significant effect, and calculations are available that include these processes [Gol95], the measured cross sections are compared to the results of these 'continuum Faddeev' calculations only. They are based on realistic models of the NN interaction that fit the NN scattering data with a χ^2 per datum of approximate one. In this section, the formalism employed to calculate the ^{3}He$(e, e'pp)$ cross section within this framework is reviewed.

Solving the three-body problem

The Faddeev decomposition of the Schrödinger equation provides a powerful tool to solve the three-body problem. In the presence of two-body interactions only, the Schrödinger equation for the complete three-body wave function with merely pair interactions can be written as the sum of three similar equations that each involve only one pair interaction [Car98]. This method has been successfully applied to the ^{3}He bound-state for different types of NN interaction models, but is also suited for solving the scattering state of the three nucleons.

In the procedures used by Golak *et al.* [Gol95], the Faddeev equations are solved in momentum space. The initial ^{3}He bound state is solved and projected onto a basis $|p_{rel}p_{cm}\alpha\rangle$. The index α labels a partial wave or *channel*, *i.e.*, a unique combination of orbital angular momentum, spin and isospin quantum numbers of the nucleon pair and the spectator. In the calculation of the bound-state wave function, thirty-four channels are considered. The nuclear matrix element from Eq. (2.7) can subsequently be formally separated in two parts: *i)* N^{μ}_{PWIAS}, which is the transition matrix element between the initial bound state, the current operator and a fully symmetrized plane wave of three nucleons without any mutual interaction and *ii)* $N^{\mu}_{\mathrm{rescatt}}$, which includes all rescattering processes. To retain consistency with the calculated wave functions, the current operator $\hat{j}^{\mu}$ is used in a non-relativistic approximation [Ish94].

It should be noted that the final state obtained from N^{μ}_{PWIAS} consists of a symmetrized plane wave, which is no eigenstate of the $3N$ Hamiltonian and is non-orthogonal to the ^{3}He bound state. It can therefore not be compared to data and can only serve to illustrate the effect of ingredients in the calculation by comparing different PWIAS results.

The equation defining the rescattering matrix element $N^{\mu}_{\mathrm{rescatt}}$ leads to a multiple-scattering series, involving the repeated application of the NN t-operator. It is derived from the solution of a Faddeev-like integral equation which sums up this multiple-scattering series [Gol95]. The solution of the integral equation depends only on the characteristics of the virtual photon involved, *i.e.*, (ω, q). A projection of this solution onto the basis $\langle p_{rel}p_{cm}\alpha|$ subsequently allows straightforward calculation of $N^{\mu}_{\mathrm{rescatt}}$ for specific final states. In this way, the computationally most involved part – solving the integral equations – has to be performed only once for any given (ω, q) value [Gol95].

The sum of PWIAS and the rescattering contribution yields the complete solution of the nuclear matrix element N^{μ}.

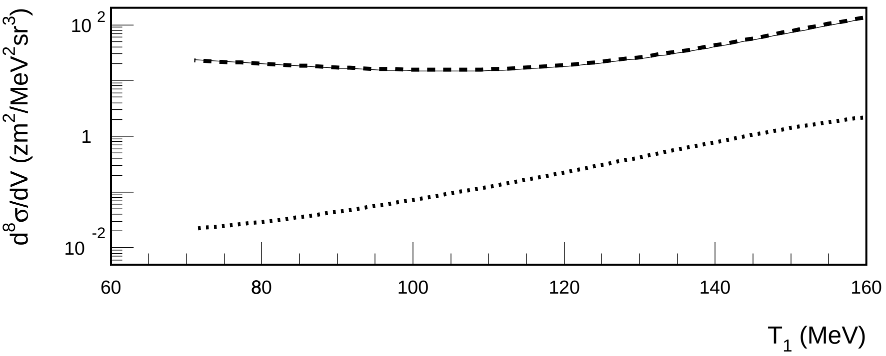

Figure 2.4: *Differential plane-wave cross section for various coupling mechanisms: coupling to the proton emitted in forward direction (dashed), coupling to the backward proton (dotted) and the coherent sum of coupling to particle 1, 2, and 3 (solid). Kinematic setting LQ, θ_1=54°, θ_2=−120°.*

One-body currents and the bound-state wave-function

Information on the initial ^{3}He bound state can in principle be obtained from reactions induced by a one-body hadronic current; in this case, the momentum of the virtual photon is transferred to a single nucleon only. In absence of final-state rescattering, this implies for the non-struck particles that the momenta observed in the final state equal their initial-state values and that the exact initial-state configuration can be reconstructed. However, the information on which nucleon was hit cannot be reconstructed from the data as the measured cross section (even in the plane-wave impulse approximation, PWIAS) is the coherent sum of coupling to any of the three nucleons.

Insight in the coupling mechanism can been deduced from the PWIAS calculations of Golak *et al.*. Although their absolute magnitude cannot be compared to the experimental data they are nevertheless valuable to determine the relative importance of the coupling to the various particles leading to the same final state. Figure 2.4 shows the cross section for the ^{3}He$(e, e'pp)$ reaction for the central kinematic configuration of LQ (see section 3.6): over the entire energy

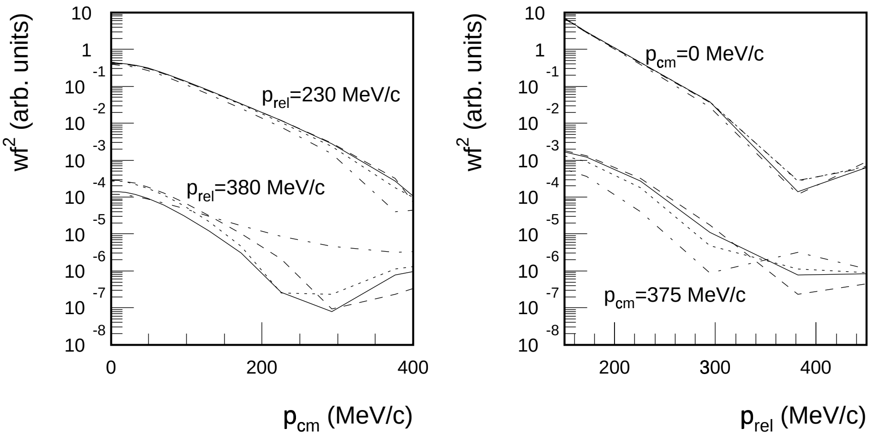

Figure 2.5: *Probability of the* ^{3}He *bound-state wave function for a two-nucleon system in a relative* $^1S_0$ *state. On the left-hand side as a function of the centre-of-mass momentum, on the right-hand side as a function of the relative momentum in the nucleon pair. The curves show calculations with the Bonn-B (solid), CD-Bonn (dashed), Nijmegen-93 (dotted) and Argonne* v_{18} *(dot-dashed) potential models.*

acceptance, the cross section is predicted to be dominated by coupling to the forward proton.

Once the coupling mechanism is known, the relative momentum inside the pp pair in the initial state can be determined. In absence of final state rescattering, the $(e, e'pp)$ reaction directly probes the initial ^{3}He wave function as shown in Fig. 2.5 for a nucleon pair in the $^1S_0$ state. The bound-state wave functions shown are based on Faddeev calculations performed with various models of the NN interaction: Bonn-B, charge-dependent Bonn (CD-Bonn), Nijmegen-93 and Argonne v_{18}. The left panel shows the neutron momentum density distribution for two values of the NN-relative momentum. In kinematic setting LQ of the present experiment this relative momentum p_{rel} ranges from 210 to 350 MeV/c, if coupling of the photon to the forward proton is assumed. The right-hand panel shows a relative NN momentum density distribution for two values of the neutron momentum. At low values of the centre-of-mass and relative momentum the results obtained using the various potential models are similar. Only at high

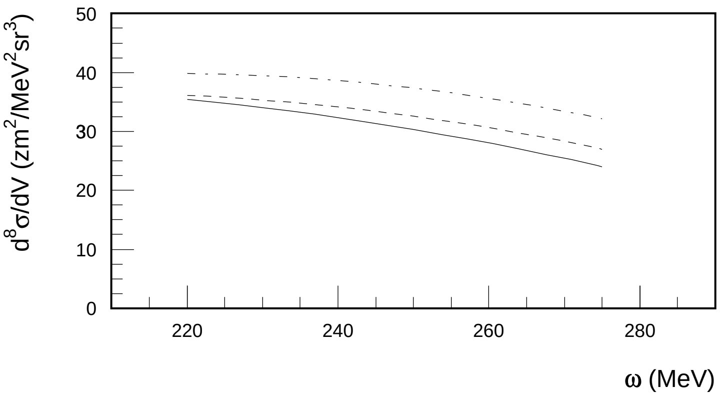

Figure 2.6: *Cross sections for the* ^{3}He$(e,e'pp)$ *reaction for varying energy transfer. The cross section was averaged over the acceptance of this experiment and corresponds to situations where the neutron can be considered as a spectator* (p_m = *30 MeV/c). The solid, dashed and dash-dotted curves correspond to calculations with only one-body, with MEC and with MEC+*Δ *currents, respectively.*

centre-of-mass or relative momentum differences can be observed that are due to the potential model used.

Two-body currents

Two-body hadronic currents involve coupling of the virtual photon to exchanged mesons, and excitation or de-excitation of Δ isobars. Meson-exchange currents have been incorporated in the solution of the continuum Faddeev equations using a formalism due to Schiavilla *et al.* [Sch89], which includes coupling to one-pion and one-rho exchange. To incorporate these currents in a way compatible with the potential model used, the exchange interactions are modified by multiplication with an additional form factor [Golpc].

A preliminary expression for the isobar currents [Sch89] was included in the calculations in a similar way. The simplified expression for the $\pi\Delta$ current reads

$$\boldsymbol{j}_{\pi\Delta}(\boldsymbol{k}_1,\boldsymbol{k}_2) \propto \frac{1}{(m_\Delta - m_N)}\; G_M^V(q)\cdots, \tag{2.8}$$

where $G_M^V(q)$ is the isovector magnetic form factor and m_Δ the mass of the Δ_{33} resonance (the $\rho\Delta$ current is similar). The current includes terms for the excitation of a nucleon to a Δ isobar as well as terms that describe the de-excitation of a 'pre-existing' Δ to a nucleon by an electromagnetic interaction. The expression quoted, also known as the *static* Δ, does not depend on the energy transfer to the system and thus will not produce the required resonant behaviour, as is shown in Fig. 2.6. This formalism should therefore been seen as a first step towards incorporation of the Δ current. A more accurate treatment of isobar currents in the Faddeev calculations will be necessary before firm statements about the role of the Δ can be made.

2.4 Choice of observables

The cross section of the ^{3}He$(e,e'pp)$ reaction depends on seven independent kinematic variables. However, the statistical accuracy of the data does not allow representation of the measured cross section for small intervals in all seven quantities simultaneously. The properties of the current operator and of the ^{3}He bound-state wave function suggest that a limited set of observables carries most of the information of the ^{3}He$(e,e'pp)$ process.

The electron kinematics naturally defines two relevant observables: the energy transfer ω and the momentum transfer q. Alternatively, the energy transfer ω can be exchanged for the invariant energy $W_{N'N'}$ of two nucleons in the final state. The ^{3}He momentum distributions shown in Fig. 2.5 suggest an important role for the relative and pair momenta. Therefore, the missing momentum p_m, which in a direct $(e,e'pp)$ reaction mechanism reflects the neutron momentum in the initial state, is selected as an observable.

Investigation of the coupling mechanisms by one-body currents shows a dominant role for coupling of the virtual photon to the forward proton. In this case, the Jacobi momentum $\boldsymbol{p}_{rel,3}$ in the initial state can be related to the momentum

$$\boldsymbol{p}_{diff,1} = (\boldsymbol{p}_1' - \boldsymbol{q}) - \boldsymbol{p}_2' \triangleq \boldsymbol{p}_1 - \boldsymbol{p}_2 \equiv 2\boldsymbol{p}_{rel,3}\,. \tag{2.9}$$

Another significant process that influences the cross section is the rescattering among the outgoing nucleons. Especially when two nucleons are emitted with (vectorially) comparable momenta the cross section will be notably enhanced.

Within the experimental detection volume, such 'FSI configurations' occur between the forward proton and the unobserved neutron. Hence, the momentum difference of these two nucleons was selected as an observable:

$$\boldsymbol{p}_{ij} = \boldsymbol{p}'_i - \boldsymbol{p}'_j. \tag{2.10}$$

The 'FSI configuration' corresponds to $p_{ij} \rightarrow 0$ MeV/c.

2.5 Numerical results

Comparison of the theoretical model by Golak *et al.* to the data requires calculation of the cross section for specific kinematic configurations, as well as the evaluation and averaging of the cross section over the experimental detection volume. In this section the methods employed and their associated uncertainties are discussed.

Uncertainties within the theoretical model

For computational reasons not all components of the NN interaction are taken into account in the calculations. The number of relevant components depends on the kinematic conditions of the reaction. In general, a higher energy and momentum transfer implies that more force components should be taken into account.

In view of the uncertainties associated with the measured cross section, a 'theoretical' accuracy of approximately 10% should be aimed at. To determine the uncertainty associated with the choice for $j \leq 3$, calculations were also performed for $j \leq 2$. Figure 2.7 shows a comparison of both calculations for the kinematic configuration corresponding to the central values of the LQ kinematic setting in this experiment. The average difference is around 6% and never exceeds 12%. It is expected that the inclusion of higher angular momentum components will change the cross section by less than this amount. Therefore, in this experiment only those NN force components were used for which the angular momentum j of the NN system was not larger than three.

Also the final state is expanded in partial waves with total three-body angular momentum J. The calculations performed for this experiment include contribu-

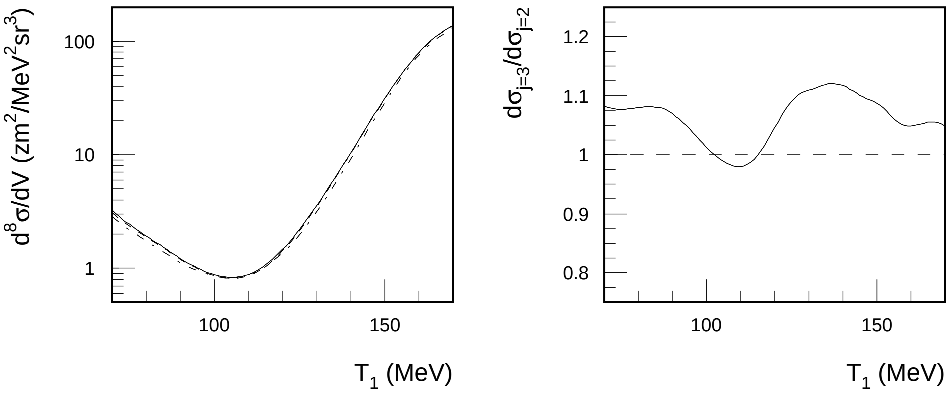

Figure 2.7: *Comparison of cross sections calculated by Golak et al. taking into account a different number of NN force components. In the left panel, the dot-dashed and solid curves correspond to calculations including force components with $j \leq 2$ and $j \leq 3$, respectively. The kinematic conditions correspond to the central values of LQ: $(\omega, q) = (220\ MeV, 305\ MeV/c)$, θ_1=55° and θ_2=−105°.*

tions up to $J = \frac{19}{2}$, which – within the kinematic domain of this experiment – ensures convergence to better than 2% on average .

Uniqueness of kinematic configurations

The kinematic configuration is not necessarily uniquely defined for a given electron kinematic setting (ω, q) and a set of values $(\theta_1, \phi_1, \theta_2, \phi_2, T_1)$ for the two outgoing protons. Figure 2.8 shows the kinematically determined curve for a selected angular combination. Here, for T_2 two possible solutions exist for $T_1 > 170$ MeV. Not only does this lead to ambiguities in the calculated cross section, it also introduces a mathematical singularity in the phase space factor (defined in Eq. 2.4) at the point corresponding to the maximal T_1 value. In this experiment, this kind of ambiguities is not relevant as the lowest detectable proton energy for the backward proton T_2 is 48 MeV.

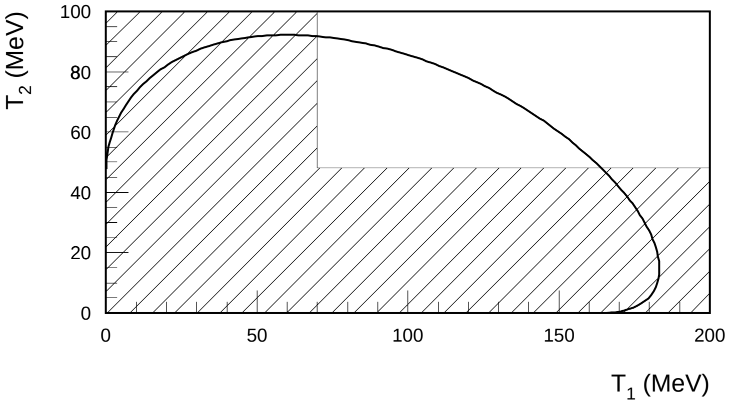

Figure 2.8: *Kinematically determined curve in the* (T_1, T_2) *plane for a fixed electron kinematic setting and fixed angles for the two outgoing protons. The curve shown corresponds to the central configuration of LQ,* i.e., θ_1*=55°,* θ_2*=−105°. The hatched area is not covered by the experimental detection volume.*

Averaging over the experimental detection volume

As mentioned, the theoretical cross section depends on seven kinematic variables that uniquely define the configuration. In general, the data are presented as a function of two or three quantities, derived from the basic kinematic variables. In this way an implicit averaging over the other quantities within the experimental detection volume is performed.

For a fair comparison between theory and data, the same averaging should be applied to the calculated cross sections. This averaging cannot be performed analytically because of the complexity of the integration limits, *i.e.*, the shape of the experimental detection volume. Performing the necessary integration by a Monte-Carlo method (*c.f.* section 4.4) requires too many computational resources to be performed with sufficient accuracy within a reasonable amount of time. Therefore, the integrals were approximated by a sum over an orthogonal grid.

The averaging of the cross section over the experimental detection volume was performed for the central value of (ω, q) only, because of constraints on

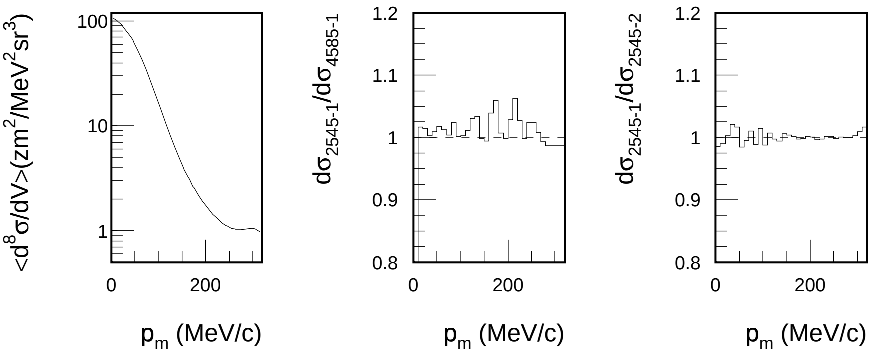

Figure 2.9: *Theoretical cross section for the LQ kinematic setting as a function of the neutron momentum, averaged over the experimental detection volume. The left panel shows the calculated cross section, the middle and right-hand panels show the ratio of the cross section calculated with the finest grid to two coarser grids. The numeric labels in these two panels specify the grid spacing.* $d\sigma_{ijkl-m}$ *indicates* $\Delta\theta_1 = i^\circ$, $\Delta\phi_1 = j^\circ$, $\Delta\theta_2 = k^\circ$, $\Delta\phi_2 = l^\circ$, *and* $\Delta T_1 = m$ *MeV.*

the available computational resources[†]. The dependence of the cross section on the electron variables was investigated by comparing the calculated results for the various kinematic configurations measured. The dependence on ω is close to linear, which implies that no change in cross section is induced by taking the central value for (ω, q). The q-dependence of the cross section shows an exponential decay (see section 5.4), which implies that the weighted average of the data corresponds to a smaller q value than the one used to calculate the cross section. This effect introduces a systematic underestimation of the cross section by at most 6%, as determined from the q dependence at low p_m.

For a given interval in the variables in which the cross section is presented, *e.g.*, an interval Δp_m, the average cross section is defined as

$$\left\langle \frac{d^8\sigma}{dV} \right\rangle (\Delta p_m) = \frac{\int \frac{d^8\sigma}{dV}(\boldsymbol{v}) D(p_m(\boldsymbol{v}); \Delta p_m) D(\boldsymbol{v}; \boldsymbol{A}) d\boldsymbol{v}}{\int D(p_m(\boldsymbol{v}); \Delta p_m) D(\boldsymbol{v}; \boldsymbol{A}) d\boldsymbol{v}}, \tag{2.11}$$

[†] Calculation of the half-shell amplitudes $|p_{rel} p_{cm} \alpha\rangle$ with NN force components upto $j = 3$ and a current operator that includes MECs takes approximately 15000 CPU seconds on a Cray C916/121024 supercomputer.

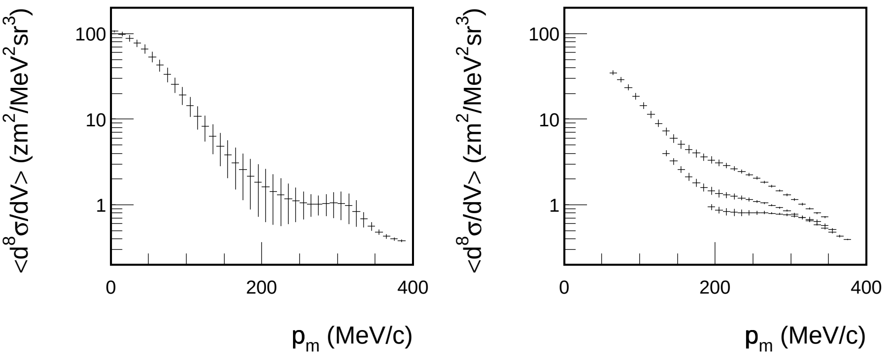

Figure 2.10: *Average cross section as a function of the missing momentum for the LQ kinematic setting. The left-hand panel is averaged over the entire detection volume without additional constraints, whereas in the right-hand panel the momentum difference p_{13} was limited to slices of 50 MeV/c wide, centred around 475, 375, and 275 MeV/c (in top-to-bottom order). Error bars indicate the width of the contributing cross section distribution.*

where $\boldsymbol{v}$ is the vector of laboratory quantities $(\theta_1, \phi_1, \theta_2, \phi_2, T_1)$, $\boldsymbol{A}$ is the acceptance region of the experimental detection setup and $D(\boldsymbol{x}; \boldsymbol{R})$ is a two-valued function that is only different from zero if $\boldsymbol{x}$ is inside the region $\boldsymbol{R}$.

The two integrals are approximated by their sums, determined with equidistant, orthogonal grids in the laboratory quantities $\boldsymbol{v}$. The distance between the gridpoints was chosen in such a way that the approximation errors introduced in the final result are below 6%, *i.e.*, comparable to the intrinsic uncertainty of the calculations due to the partial wave truncation. To verify the accuracy obtained, the cross section was calculated with a varying amount of grid points; the results of these calculations are displayed in Fig. 2.9. From these and similar tests it was concluded that a grid point density of $(\Delta\theta_1, \Delta\phi_1, \Delta\theta_2, \Delta\phi_2, \Delta T_1) = (2°, 5°, 4°, 5°, 1\ \text{MeV})$ is sufficiently accurate[‡].

[‡] This requirement on the grid density leads to about 2.5×10^6 points per kinematic setting. Calculation of one grid point typically takes about 0.6 seconds on a 270 MHz UltraSPARC–IIi processor, which implies that it takes about 17.5 CPU days to calculate the grid for one kinematic setting and one current operator.

The averaging of the cross section over the experimental detection volume may obscure dependencies of the cross section on non-explicit variables. Such dependencies lead to a large spread in the values for the individual cross sections contributing to a certain grid point. To investigate such dependencies, the standard deviation of the cross section distribution from which the average is derived was determined for every bin.

Figure 2.10 shows the missing-momentum distribution for the LQ kinematic setting. In the left-hand panel, no limitations were imposed on the contributing part of the detection volume. From the observed spread, which is as large as 60% around 200 MeV/c, it can be concluded that the cross section depends strongly on a non-explicit variable. In the case shown, the dependence on the momentum difference p_{13} is relatively strong, as the experimental acceptance contains an 'FSI configuration' around p_m=300 MeV/c. Moreover, the detection volume in the (p_m, p_{13}) plane is triangular in shape in such a way that for higher p_m values, increasingly lower values of p_{13} are covered. A projection on p_m for slices in p_{13} of 50 MeV/c wide shows that the spread of the theoretical distribution is reduced to less than 10%, as shown in the right-hand panel.

Considerations regarding relativity

At present, no framework exists to solve the three-body problem in a Lorentz-covariant manner. Although certain parts of the calculations – especially the kinematics and the calculation of the phase-space factor – can be performed with 'relativistic' kinematics, this would introduce internal inconsistencies in the calculation, as the wavefunctions and operators are entirely non-relativistic. By performing the theoretical calculations in a completely non-relativistic fashion, these inconsistencies can be avoided, although at the cost of introducing kinematic ambiguities.

In comparing calculations to data, the momenta that are explicitly shown along the axes are kept identical, *e.g.*, in presenting a missing-momentum distribution, the theoretical cross section shown for a particular value of p_m corresponds to the same momentum being used for p_3 in the calculation. This implies at the same time that the coverage of the non-explicit momenta (in this case p_1 and p_2) contributing to the average cross section is slightly different from the one spanned in the experiment.

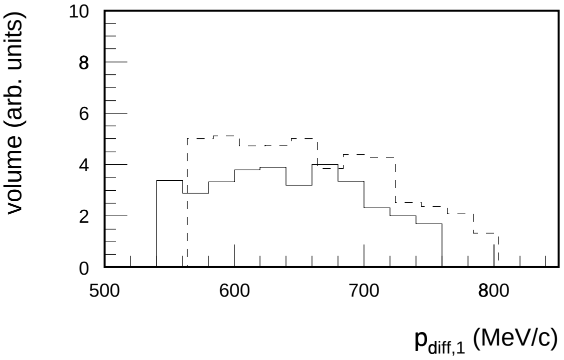

Figure 2.11: *Range in $p_{diff,1}$ contributing to the region $p_m < 100$ MeV/c. The solid (dashed) curve shows the distribution according to a non-relativistic (relativistic) calculation of the kinematics. The effective $p_{diff,1}$ value in the non-relativistic case is approximately 20 MeV/c too low. (kinematic configuration: LQ)*

The effect of this momentum mismatch was investigated for various kinematic conditions. The largest discrepancies were observed in the low p_m region, as this domain is covered primarily by p_1 values around 540 MeV/c. As the cross section shows a sizeable dependence on $p_{diff,1}$, the mismatch introduced in $p_{diff,1}$ is expected to be the most significant factor.

For the kinematics LQ at $p_m < 100$ MeV/c, the domain of $p_{diff,1}$ contributing to the cross section is shown in Fig. 2.11. The momentum mismatch of $p_{diff,1}$ amounts to 20 MeV/c. From the dependence of the cross section on $p_{diff,1}$, the expected change in the theoretical cross section due to this mismatch is estimated to be around 8%.

III Experimental Setup

In this chapter the electron accelerator facility, the target and the detectors are discussed. The choice of the kinematic configurations is motivated.

3.1 The electron beam

For the measurements described in this thesis, the electron beam provided by the Amsterdam Pulse Stretcher facility (AmPS) was used. This facility consists of a linear electron accelerator with a low duty-factor and a storage-stretcher ring. When operated in storage mode, experiments with gaseous targets internal to the ring are performed in the IT hall. In stretcher mode – the mode used for the present experiment – the injected bursts of electrons are extracted as an almost continuous current for experiments in the EMIN hall. A view plan of the facility is shown in Fig. 3.1.

The Medium Energy Accelerator (MEA) [Vri84] provides a beam of electrons in short bursts up to 2.1 μs with a repetition rate of at maximum 150 Hz. The energy can be varied continuously up to 700 MeV at zero current. An energy spectrum compression system brings the energy spread down to less than 0.1%. The electrons are subsequently injected into a stretcher ring (the AmPS proper) with a circumference of 212 m [Wit93]. This length corresponds to a revolution time of 708 ns. A closed orbit for the recirculating electrons is defined by a lattice of 32 dipoles, 68 quadrupoles, and 32 sextupoles.

As the electrons are bent in the arcs of the ring, they loose energy due to synchrotron radiation, which is compensated by an additional RF cavity inside the ring. To obtain extraction from the ring, the RF voltage inside this cavity is gradually reduced. This causes shrinking of the phase space area for stable circulation [Wu91]. In the unstable phase space region, electrons suffer large excursions from the beam centre. At a distance of about 25 mm from the beam centre line, an electrostatic septum intercepts the particles and enlarges their separation with respect to the stable recirculating beam using an electric

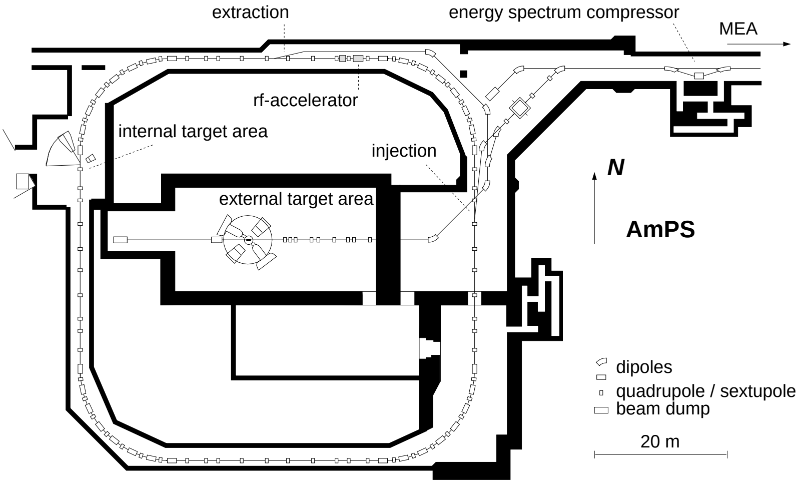

Figure 3.1: *Floor plan of the AmPS facility. Of the MEA linear accelerator only the energy spectrum compressing system is shown. The experiment was performed in the external target area EMIN.*

field [Lin92]. The extracted beam is then guided to the target area by magnetic elements.

The extraction time can be varied to a maximum of 20 ms, limiting the MEA repetition rate to values above 50 Hz for a continuous beam. The optical configuration of the ring allows for at most three-turn injection.

Experimental conditions

For all kinematic settings of this experiment MEA was operated at a repetition rate of 50 Hz and a burst length of 2.1 μs. The electrons injected into the AmPS ring were extracted over a period of 20 ms with a *macroscopic* duty factor of more than 80%. This duty factor varied by no more than 10% during the experiment. In order to obtain the highest macroscopic duty factor, the lowest possible repetition rate compatible with the required luminosity was selected.

Inhomogeneities in the beam structure at the sub-microsecond time scale give rise to a time-difference distribution of the accidental coincidences which is not flat [Ond98b]. It is therefore advantageous to optimize this *microscopic* duty factor, which is mainly sensitive to details of the injection process.

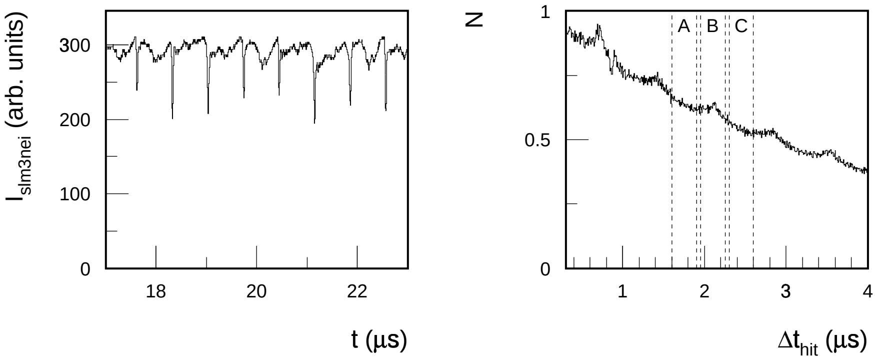

Figure 3.2: *The beam structure at time scales close to the revolution time influences the instantaneous luminosity at the target and the effective real-to-accidental ratio. The left panel shows the instantaneous current in the AmPS ring as a function of time. The right panel shows the time difference distribution between two successive hits in a hodoscope strip of the HADRON3 detector.*

The severity of these inhomogeneities can be estimated by investigating the time difference distribution of successive events in a fast-counting detector. Changes in the instantaneous current that are due to the revolution time in the ring will give rise to a peaked structure with a periodicity of 708 ns (see Fig. 3.2, right panel). Following [Sta99b], an intensity asymmetry

$$A = \frac{N_B - \frac{1}{2}(N_A + N_C)}{N_B + \frac{1}{2}(N_A + N_C)} \tag{3.1}$$

can be defined, where N_i is the number of events in the time interval i as shown in the right panel of Fig. 3.2. All intervals are 300 ns wide. This intensity asymmetry is a measure for the relative surplus of counts in region B, which is centred around Δt=2100 ns, with respect to the expected yield in this area as derived from the average in A and C. For the distribution shown in Fig. 3.2, the intensity asymmetry is 2.2%.

To ensure a continuous current at the 708 ns time scale, three-turn injection was used during the entire experiment. In this mode, injection of electrons from MEA continues while electrons already circulating in the ring pass the injection point undisturbed. The optical properties of the ring and the pulse length of 2.1 μs allow for three-turn injection. A mismatch between burst length and revolution time will now cause a reduction to only 2/3 of the maximum circulating current. The effect on the time-structure of the beam will then be only minor. The intensity asymmetry A was monitored continuously during the experiment. It was always less than 5%.

For this experiment, the incident electrons had an energy of 563.7±0.3 MeV as determined with elastic scattering measurements from ^{12}C and ^{3}He, performed several times in between the coincidence measurements (see section 4.5).

3.2 Target setup

The target setup consisted of a cryogenic, high-pressure 'barrel' cell containing gaseous ^{3}He, a graphite target with a thickness of 93.5 mg/cm^{2} and an aluminium-oxide target for beam calibration purposes.

The barrel cell is a cylindrically shaped container with a diameter of 50 mm and an aluminium wall with a thickness of 250 μm [Una91]. At the top-side of the container a heat-exchanger is mounted consisting of 34 copper ribs. This heat exchanger is connected to a cold head. A cryogenic refrigerator with a capacity of 30 W at 18.5 K is used. Between the ^{3}He gas and the heat exchanger, heat is transported by natural convection.

Temperature sensors are mounted directly on top of the heat exchanger. The cell can hold a pressure of 4 MPa at temperatures around 20 K. A 5 MPa pressure sensor is mounted outside the scattering chamber in the filling line of the target. The cell can be moved vertically by a pneumatic system connected to the cold head in such a way that the solid targets can be positioned at beam height by means of a stepping motor. Both target selection systems are controlled remotely.

The cell is connected to a closed-circuit gas-handling system containing a supply of ^{3}He at 3 MPa, a compressor and a 5 l emergency recuperation vessel. A PLC system monitors the pressure sensor and will open a valve to the recuperation vessel if the cell pressure exceeds specified safety limits. The setup is designed such that cooling failures will not result in loss of ^{3}He gas. The system avails of a cold-trap which can be used to remove contamination from the recuperated ^{3}He which might freeze in the filling lines to the target.

The recuperation vessel can also be used to temporarily store the ^{3}He gas whilst performing measurements with a different gas (*e.g.*, Hydrogen) or background measurements with an empty cell.

During the experiment the recuperation system was used several times and no loss of ^{3}He gas was observed. All measurements with the ^{3}He gas-target were performed at a temperature of 15 K and a pressure of 2.9 MPa, as determined by the sensors attached. The effective target thickness was determined by elastic scattering measurements as described in section 4.5.

The carbon target

In order to perform measurements of the absolute detection efficiency of the electron detector system, a graphite target of 93.5 mg/cm^2 was used. This fixed target can replace the barrel cell at beam height and be rotated remotely. Angles from 50 to 120 degrees with respect to the incident beam can be reached. The homogeneity of the target is better than 1%.

3.3 Detection of the scattered electron

The scattered electrons were detected in the QDQ magnetic spectrometer. This focussing spectrometer can detect electrons within a range of ±4.5% with respect to the selected central momentum value. The momentum resolution is better than 2×10^{-4} [Vri90]. The solid angle is defined by an octangular slit with an acceptance of ±70 mrad in both the in-plane and out-of-plane direction. The detector package consists of two pairs of multi-wire drift chambers (MWDCs) [Dis84], a thin (3 mm) 'bottom'-scintillator covering the same area as the wire chambers, twelve 'timing'-scintillator paddles (8 mm) segmented in the dispersive direction, an aerogel Čerenkov detector and a 'top'-scintillator (4 mm). The index of refraction of the aerogel material is n=1.05. The bottom- and top-scintillators are read out on both sides by a photomultiplier tube. A cross section of the detection package is shown in Fig. 3.3.

The trigger for electrons is defined as a coincidence between a hit in the bottom-scintillator and any of the twelve timing-scintillators. The phase of the trigger is determined by the timing-scintillators. Information from the aerogel Čerenkov detector is only used in the off-line analysis.

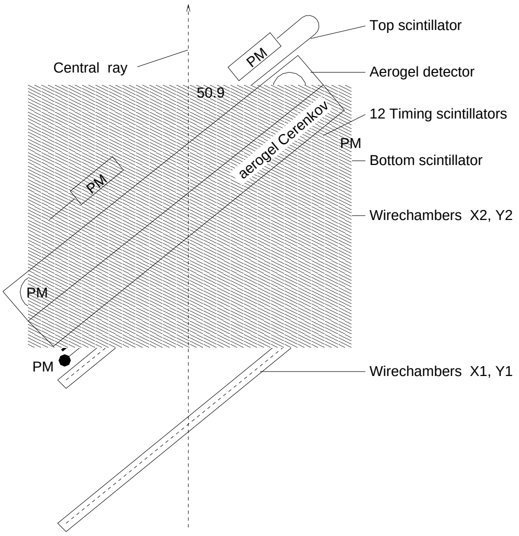

Figure 3.3: *The focal plane detection package of the QDQ magnetic spectrometer.*

The position information in the successive wire chambers is used to reconstruct the momentum vector at the target [Vri90]. Information is also obtained on the vertex position (y_{tg}) perpendicular to the optical axis of the spectrometer with a resolution of 1 mm. The solid angle covered by the spectrometer has been found to be dependent on the vertex position for $y_{tg} < -6.0$ mm or $y_{tg} > 3.0$ mm [Spa97].

3.4 Proton detectors

To detect the protons emitted from the target two scintillator detectors were used: HADRON3 and HADRON4. These detectors both cover a large solid angle and span a sizeable range in detected proton energies [Mul95, Pel96, Pel99]. The design of both HADRON detectors is similar and the differences will be noted only where relevant.

As these detectors are non-magnetic, the scintillation material is directly exposed to all particles emitted from the target. At the anticipated luminosity (above 10^{35} atoms/cm^2 s) this requires a setup with a large granularity to be

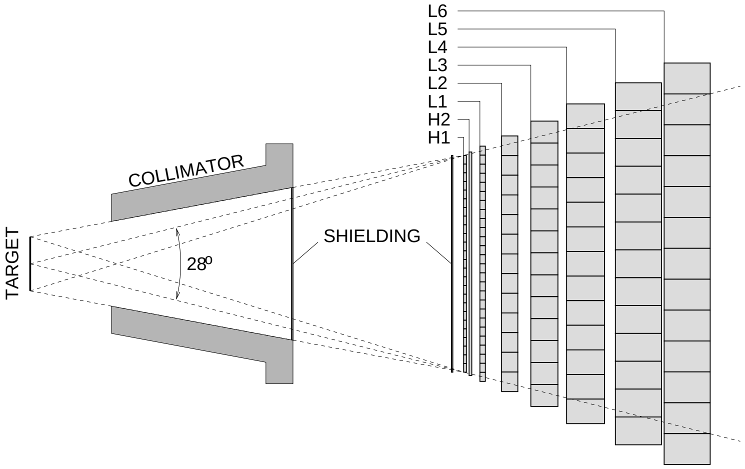

Figure 3.4: *A top view of the HADRON3 detector. The detector housing is not shown. The distance between the target and the front of the first hodoscope layer H1 is 800 mm.*

able to cope with the count rate in each individual element. A top view of the HADRON3 detector is shown in Fig. 3.4. Its design is guided by the results of extensive beam tests with scintillators and absorbers of various dimensions [Zon94].

The detection system proper consists of a pair of thin, perpendicularly segmented 'hodoscope' strips to determine the impact position, and a series of larger 'stopping' layers to measure the proton energy and perform particle identification. In front of the hodoscope shielding material may be mounted to reduce the flux of low-energy particles. At the same time this shielding will raise the detection thresholds for protons. The active detection elements consist of BC408 plastic scintillator material and are mounted inside a light-tight lead housing with a thickness of 50 mm on the front side and 30 mm at the sides and at the back. In this experiment HADRON3 was operated with 5.2 mm lead shielding, giving an effective lower detection threshold for protons of 72 MeV. HADRON4 was operated with stainless steel shielding of 2.0 mm (lower threshold 48 MeV) or 1.0 mm (36 MeV).

In between the housing and the scattering chamber a lead collimator with a wall thickness of 50 mm is installed to prevent the influx of particles not originating from the target. An extended target of ±100 mm is allowed for. The distance between the target and the first hodoscope plane (H1) is 800 mm.

For each scintillator element the generated light is collected in a photomultiplier tube (PM). For the thin (2 mm) hodoscope elements of HADRON4 PMs are attached to both ends of the scintillator to counter losses due to the strong attenuation in these 640 mm long strips. The high-voltage applied to each PM can be individually adjusted to match the input sensitivity of the charge digitizers.

The hodoscopes and the first stopping layer (L1) require a high degree of segmentation to cope with the high flux of low-energy electrons coming from the target. Besides, this segmentation is needed to obtain an accurate determination of the impact position of the impinging particles. The effective width of the in-plane-segmented hodoscope H1 and of L1 is identical, but offset by half the width of one element to increase the in-plane angular resolution. In the subsequent stopping layers, the segmentation is reduced. The increasing width of the elements in the back layers takes the additional angular spread due to multiple scattering and hadronic interactions into account.

Characteristic parameters for both HADRON detectors are given in Table 3.1.

Data acquisition

Given the high count rate per element (up to 1 MHz) and the need for complex trigger decisions, the analogue signals from the PMs are digitized per element immediately on arrival. In this way the dead time of the DACQ is minimized to the combined effect of channel and detector-trigger dead time. In this way, time needed for global trigger decisions and for readout of the data from the channels does not introduce additional dead time.

The digitizers (‘frontends’) are constructed as triple-height VME modules, with the standard VME bus supplemented with trigger and DACQ control lines. Each VME board contains two independent frontends. As the digitizers are autonomous units, they use an internal logic condition as the start-of-measurement: integration of the analogue signal starts when both the slope (‘low’ threshold) and the height (‘high’ threshold) exceed the specified discriminator levels. At the same time the time-to-amplitude converter (TAC) is started, the phase of which is determined by the differential, ‘low’ discriminator to minimize rise-time effects in the time integration process. Both charge and arrival time (relative to

Table 3.1: *Characteristic parameters of both HADRON detectors. Nominal values are shown; the actual values during the experiment or used in the analysis of the measurements may depend on the shielding installed and the cuts applied to the data during the analysis.*

	HADRON3	HADRON4
number of scintillators	141	94
number of photomultipliers	141	134
hodoscope segmentation	25	20
hodoscope width per element (mm)	16	32
L1 elements (subtriggers)	26	21
opening angle, in-plane and out-of-plane (deg)	28	44
in-plane angular resolution (deg)	0.5	1
out-of-plane angular resolution (deg)	1	2
subtended solid angle (msr)	230	540
number of stopping layers	6	4
T_p^{min} (MeV)	36	25
T_p^{max} (MeV)	239	165

the detector trigger) are determined. Besides, every frontend avails of a direct ('hit') logic output which may be used as input to the detector trigger modules. All relevant parameters (offset and width of the charge and time integration, signal thresholds and the 'hit' delay) can be set by VME commands [Zon94].

If a valid detector trigger is generated, a time-stop signal is provided to the frontends using the special-purpose part of the crate backplane. This signal stops the TACs and starts the digitization of the charge integrator and TAC voltages. The converted values are subsequently stored in a 64-word deep cyclic buffer in dual-port memory (DPM). The frontend electronics is reset if no time-stop signal arrives within a certain time after the TAC has reached its maximum value.

Because at most 19 digitizer modules can be mounted in one crate, the frontend electronics spans four VME-crates per detector. Every crate contains a data-acquisition and readout transputer (DART) [Kwa91] which manages the special-purpose bus-lines and controls the VME bus for data readout. Amongst other functions, the DART determines the address of the digitized information in the DPM cyclic buffer of each frontend, using the special-purpose part of the crate back plane. When requested, the information is retrieved by the DART and stored as sub-event in its local event fragment memory (EFM). These sub-event fragments are combined by the acquisition transputer chain into complete HADRON events to be provided to the event builder (EB).

Trigger

To limit the trigger rate to an acceptable level of at most 800 kHz, signals from various elements are combined. Taking advantage of the segmented design, coincidences of hits in elements in subsequent layers are taken as trigger condition. To keep the detection threshold for protons as low as possible, the first two layers with identical orientation are used, *i.e.*, H1 and L1. As the elements in these layers are offset with respect to each other, a coincidence between the L1 'hit' signal and the logic OR of both corresponding H1 strips is used to generate the subtrigger (T1A). The OR of these subtriggers is then made (T1B) and used as detector arm trigger (ATR). For HADRON4 the OR of the 'hit' signals from both sides of an H1 element is used in T1A.

The phase of the final subtrigger is determined by the arrival of the 'hit' signal from the L1 elements. The width of the acceptance window – started by any of the corresponding H1 hits – is computer controllable. Care is taken to ensure that the signals from real tracks are well within the acceptance of the gate.

Tools for efficiency determination

The HADRON detector has two sources of dead time: the process of digitization in each frontend and the dead time associated with the processing of the trigger.

The frontend dead time is due to the local digitization process and its duration is around 110 ns, depending on the adjustable parameters of the TAC. To monitor the induced inefficiency, an electronic test pulse is sent at regular intervals to all digitizer modules. A dedicated digitizer module is employed to determine the total number of test pulses generated. The live time per frontend is determined using the acceptance ratio deduced from these test pulses.

The same quantity is also measured by flashing a preset amount of light either into the scintillation material or directly into the PM. A photo diode is employed to detect these laser-generated flashes and its signal is digitized in the same way as the regular events. The live time determined with the laser flasher has been found to be identical to the one determined with the test pulse [Pel96].

In this experiment the determination of the frontend live time is based solely on test pulse data. It is lowest in the two hodoscope layers, as they suffer from a high flux of low-energy particles, but was always higher than 80%. The L1 live time was above 99% because of the high threshold set for these triggering elements. The live time of the other stopping layers was better than 93% and 90% for HADRON3 and HADRON4, respectively.

The dead time due to the trigger is set at a fixed value of 250 ns. To determine the trigger live time, a prompt output with negligible dead time is provided by the trigger module. The ratio of generated arm triggers (who are subject to the 250 ns dead time) over the number of prompt triggers determines the trigger live time and is applied as a correction factor to the data.

The trigger live time during this experiment was always better than 77%.

3.5 Coincidence detection

In an $(e, e'pp)$ reaction, the two protons will be emitted from the vertex at the moment the nucleus is struck by the electron. In this case, all three detectors (QDQ, HADRON3 and HADRON4) will give an arm trigger (ATR) within an interval of several hundred nanoseconds. However, such a coincidence can also be due to particles that originate from different nuclear reactions, that occur accidentally at roughly the same time. To estimate the fraction of the accidental events that contribute to the three-fold coincidence time region, a coincidence detector (CD) is employed, that measures the arrival times of the three ATR signals with a resolution of 48.8 ps [Ver96]. Each ATR starts a 'window' with a set length of 125 ns. These window signals are used by the gating and prescaling module to classify events based on their coincidence type (single, double or triple). The readout of each type of coincidence event can be individually enabled and prescaled using a special module in the CD. The readout of the various types of events is completely independent as long as the total event rate does not exceed 5 kHz or 1.4 MByte/s. In this experiment all three-fold coincident events (triples) were stored as well as a subset of the doubles and singles for monitoring purposes.

So as not to load unnecessarily the data links with the transport of unneeded event fragments (from arm events which did not take part in one of the selected coincidences) an event fragment labelling system is used. Together with the ATR signal from the detector arm, an ATR label is sent to the CD. If the event-fragment is deemed 'interesting', this label, together with an event trigger (ETR), is sent back to the detector arm. The event-fragment data is then collected from the sub-event builders in the various crates and transported, together with the arrival time information from the CD, to the event builder (EB). Using this labelling system events can be retrieved asynchronously. Counters internal to the event data are used to check the consistency of the combined events. Besides, triple events due to test pulses delivered simultaneously to both HADRON detectors and the QDQ are used to perform off-line consistency checks.

3.6 Kinematic conditions

In order to enhance the contribution due to knockout of correlated proton pairs to the cross section, measurements are preferably performed in the so-called 'dip' region. Here, sufficient energy is transferred to the nucleus to emit two high-energy nucleons (above the detection threshold of the HADRON detectors), while at higher energy transfers the contribution from Δ excitation is expected to increase.

Several constraints determine the accessible kinematic configurations:

- the beam energy is restricted to less than 600 MeV. Higher energies limit the available beam current and make the accelerator more sensitive to failure.

- the central detection angle of the scattered electron should be larger than 27° due to geometrical limitations which prevent the QDQ spectrometer to move closer towards the beam pipe.

- the transferred energy should be sufficient for both protons to deposit a reasonable amount of energy in both HADRON detectors, taking into account the detection thresholds of HADRON3 and HADRON4, namely 72 MeV and 48 MeV, respectively. (with reduced shielding the threshold for HADRON4 becomes 36 MeV)

- preferably, all measurements should be performed at the same incident energy to reduce the overhead due to accelerator and ring tuning.

Kinematic configurations were selected in accordance with the aforementioned limitations. To investigate the coupling mechanism of the virtual photon to the ^{3}He system, measurements were performed at various values of the three-momentum transfer q. A series of measurements at various energy transfer values allowed study of the reaction mechanism as a function of the invariant energy of the photon and two-proton final state. In this way, the relative importance of one-body and two-body hadronic currents can be investigated.

At beam energies below 600 MeV and small electron scattering angles (27°), the dip region corresponds to energy transfer values around 200 MeV. The wish to measure at missing-momentum values around 0 MeV/c requires that ω be at least around 220 MeV.

At $\omega = 220$ MeV the requirement that $\theta_{e'} > 27^\circ$ gives a minimum momentum transfer q of 305 MeV/c at an incident energy $E_0 = 564$ MeV. Higher incident energies raise this q-value, lower E_0 reduces the flux of virtual photons. The setting is symbolically labelled LQ in the remainder of this thesis.

Besides, extensive investigations have been made to find kinematic configurations where the influence of final-state interactions might be minimized. This search was guided by the continuum Faddeev calculations [Gol95] as described in section 2.3. Within the accessible kinematic domain, LQ is the only kinematic setting that contains two-proton angular combinations where the calculated full cross section, calculated with a one-body hadronic current, is identical to the plane-wave prediction. These have been measured in the kinematic setting labelled PEF.

The ω value of 220 MeV was chosen to perform measurements at various momentum transfer values. Three values of transferred momentum were selected: 305 (LQ), 375 (CQW) and 445 (HQ) MeV/c, where the choice of q=445 MeV/c was dictated by the strongly reduced count rate at higher values of q. The esti-

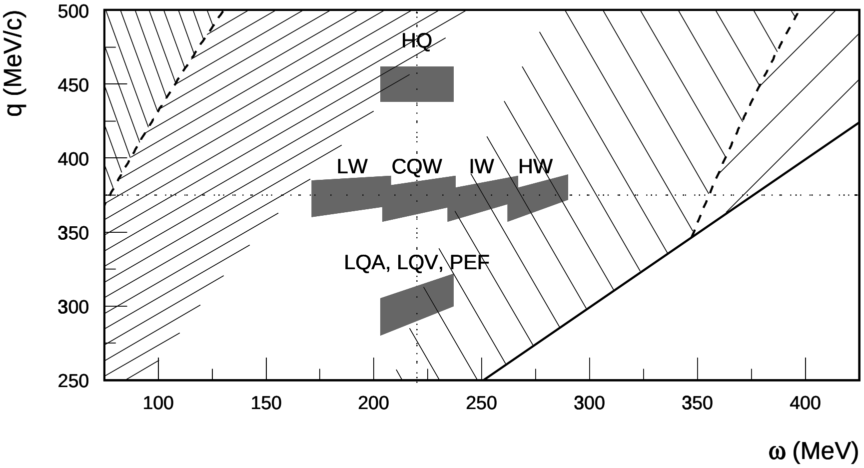

Figure 3.5: *Shaded areas indicate the coverage in (ω, q) due to the acceptance of the QDQ spectrometer. The dashed lines indicate kinematic conditions corresponding to quasi-elastic knockout (left-hand side) or excitation of the Δ resonance (right-hand side). Hatched regions indicate the width (FWHM) as calculated by the code QFS, due to [LiO88]. Symbolic names of the kinematic settings are indicated.*

mated count rate for HQ is 20 times smaller compared to estimates for the LQ setting.

At q=375 MeV/c, measurements at several energy transfer values were performed in such a way that a continuous range from 170 MeV to 290 MeV was covered with small overlaps between the different settings. Within this range, the invariant mass of the two-proton system in the final state, $W_{p_1' p_2'}$, ranges from 2005 to 2120 MeV/c^2. At the low-ω point (LW) the shielding of the backward proton detector HADRON4 was reduced to gain detection volume in the region of low missing momenta. This required a 50% reduced luminosity with respect to other kinematic settings at the same proton detection angle.

The coverage of transferred momentum and energy – determined by the acceptance of the QDQ spectrometer – is indicated in Fig. 3.5.

The positioning of the two proton detectors was guided by the emission of the protons at conjugate angles. The angle of the forward proton detector, HADRON3, was determined by geometrical constraints of detector housing and beam pipe. The angle between $\boldsymbol{q}$ and the forward proton was kept as small as possible. The backward proton detector was located around the conjugate angle, corresponding to the kinematic configuration where the neutron is left at rest in the final state.

The LQ kinematic setting, which features the largest flux of virtual photons, was used to perform additional measurements at other proton angles to investigate the angular correlation and the behaviour of the cross section as a function of the angle γ_1 between $\boldsymbol{q}$ and the forward proton.

An overview of all measured kinematic settings is given in Table 3.2.

Table 3.2: *Overview of the kinematic configurations of the* ^{3}He$(e,e'pp)$ *experiment. The incident energy was 563.7 MeV. The transferred four-momentum* $Q^2 = q^2 - \omega^2$ *is indicated.*

ID	ω (MeV)	q (MeV/c)	$\theta_{e'}$ (deg)	θ_q (deg)	Q^2 (GeV/c)^2	θ_{H3} (deg)	θ_{H4} (deg)
LQA	220	305	−27.72	31.6	0.045	53.8	−120.4
LQV						53.8	−92.9
PEF						79.9	−100.1
CQW	220	375	−40.26	36.4	0.092	53.8	−105.3
HQ	220	445	−52.01	37.6	0.150	53.8	−119.7
LW	190	375	−41.14	41.0	0.110	53.8	−119.7
IW	250	375	−38.72	31.6	0.078	53.8	−105.3
HW	275	375	−36.76	27.5	0.065	53.8	−105.3

IV Data Analysis

The process of converting the measured data into a differential $(e, e'pp)$ cross section can be divided in several parts. First, particles are identified and their momentum and relative timing are determined, using the raw data obtained from each detector. Subsequently, the number of real events is determined as a function of one or more kinematic quantities. After normalization and correction for detection volume, cross sections are obtained. This chapter is devoted to the methods used in this analysis. At the end, an estimate of the systematic uncertainty associated with the determined cross sections is presented.

4.1 Analysis of QDQ data

The event information obtained from the QDQ magnetic spectrometer contains hit-pattern information from the four MWDCs and 12 timing scintillators, and ADC information from the aerogel Čerenkov detector. The matrix-formalism described by de Vries *et al.* [Vri90] is used to reconstruct the vertex position (y_{tg}) and the momentum vector of the scattered electron at the target. A suitable set of matrix elements for use with an extended target was determined earlier by Spaltro [Spapc]. Additional data collected in this experiment were used to verify and improve this set of matrix elements. Several matrix elements were adjusted to reflect the alignment conditions of this experiment.

The y_{tg} reconstruction was verified using the known dimensions of the barrel cell. At an angle of 27°, the entire length of the cell is within the y-acceptance of the QDQ. The diameter of the cell, as determined from the top-to-top distance in Fig. 4.1, was found to be 47±0.8 mm, which is reasonably close to the actual value of 50 mm.

Using sieve-slit measurements performed with the ^{3}He target cell, the correlation between y_{tg} and the in-plane scattering angle ϕ was verified. Using the known calibration for y, the first-order (y, ϕ) and the zeroth-order ϕ matrix element were adjusted. The resulting set of matrix elements was checked

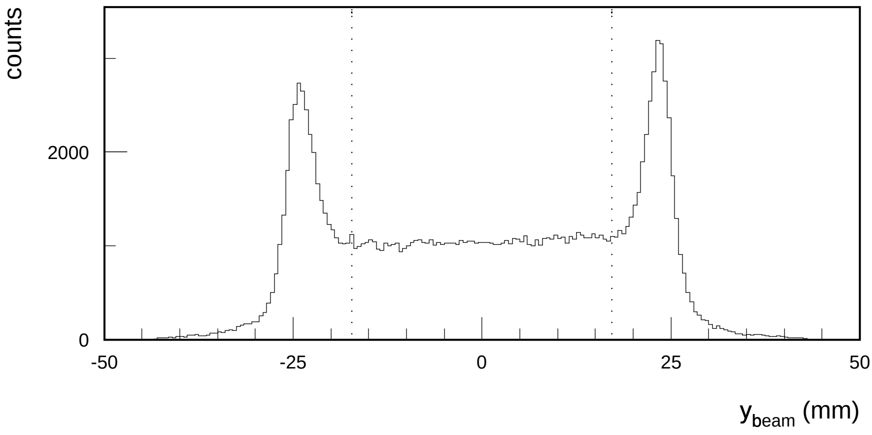

Figure 4.1: *The y_{tg} reconstruction, corrected for the angle of the QDQ. The dashed lines indicate the projection of the cut, used in the analysis, to reject events from the cell walls. They correspond to a y_{tg} position of ±8 mm. (data: LQA)*

with several sieve-slit measurements taken on ^{12}C and ^{3}He, at various moments during the experiment.

The time-of-flight reconstruction of the electrons, obtained from the matrix elements determined by Spaltro [Spapc], was verified using the time-difference distribution of two-fold coincident events from this experiment. As the phase of the QDQ detector trigger is defined by combining the logic signals from twelve different regions in the detection plane, off-line corrections have to be applied to synchronize events originating from these different regions. They are determined employing the time differences of two-fold coincident events and the hit-pattern information contained in the QDQ event fragments. The timing corrections applied are all less than 3 ns.

Besides electrons, also negatively charged pions and muons will reach the detection system of the QDQ. Therefore, information from the aerogel Čerenkov detector is used to suppress the contribution from these particles. With the index of refraction n=1.05, pions and muons with momenta below 440 MeV/c and 330 MeV/c respectively will not generate Čerenkov light in the aerogel.

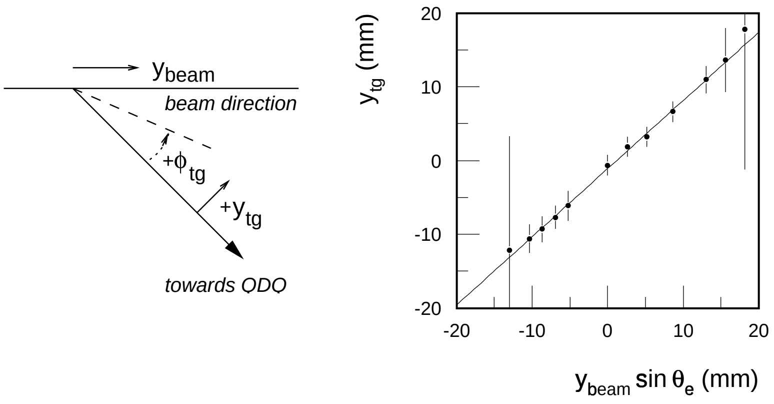

Figure 4.2: *Calibration of the y_{tg} reconstruction based on the data collected with a slanted target. The QDQ angle, $\theta_{e'}$, was 60°. Error bars indicate the width (FWHM) of the reconstructed y distribution. The coordinate system used for the QDQ matrix element formalism is shown on the left-hand side.*

The probability that an electron will not generate a signal in the Čerenkov detector is estimated to be below 1.7×10^{-4} [Sch97]. Due to the finite resolution with which the signals from the Čerenkov PMs are digitized, an additional inefficiency is introduced in the analysis by requiring that the measured ADC value is different from zero. The additional loss is estimated to be less than 0.5%.

The Y-dependence of the (θ, ϕ) acceptance

The angular acceptance of the QDQ as a function of y – the distance between the vertex position and the optical axis, as seen on a line perpendicular to this optical axis, shown in Fig. 4.2 [Vri90] – is only flat between -3 and $+6$ mm [Spa97]. To verify this range and to investigate the (θ, ϕ) acceptance for y positions outside this region, measurements were performed with a slanted copper strip target. With such a setup, the target height is correlated with the vertex position along the beam line (y_{beam}). Measurements were performed for twelve different vertex positions between $-21 < y_{beam} < 15$ mm. The QDQ spectrometer was positioned at $-60°$ and the '70x70' slit was used. This slit has an octangular shape and an

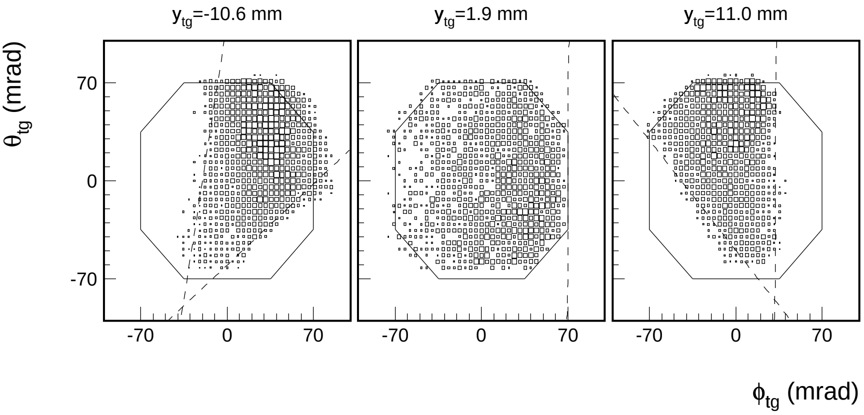

Figure 4.3: *Filling of the QDQ solid angle for three values of* y_{tg}. *The octagonal shape indicates the nominal acceptance of the '70x70' slit. The dashed lines represent the parametrization of the acceptance as used in the analysis (see text). The data shown were obtained with the slanted target.*

angular acceptance of ±70 mrad for both the in-plane and out-of-plane angle. It is located at 481.5 mm from the target.

The various data sets are used to verify the y_{tg} reconstruction, as this is a prerequisite for using y_{tg} in the analysis of extended-target data. Figure 4.2 shows the reconstructed y_{tg} as a function of the nominal y-position as determined from the measurement of the slanted-target height. The contraction of y as determined from the slope is 1.06 ± 0.04, which is identical to the value obtained from the cell wall measurement.

To determine the acceptance of the QDQ as a function of y_{tg}, two-dimensional plots of the (θ, ϕ) distribution are parametrized using cutoff lines in the (θ, ϕ)-plane which depend on y_{tg}. The parameters are determined on basis of both the slanted-target data and data obtained with the barrel cell during this experiment. To adequately describe the acceptance, two sets of straight lines in the (θ, ϕ)-plane are needed, one for each side of the acceptance ($y_{tg} < 0$ and $y_{tg} > 0$ mm, respectively). The effect of y_{tg} on the acceptance, as well as the parametrization are indicated in Fig. 4.3. The effective acceptance described by this method is used to calculate the contribution of the QDQ to the detection volume as described in section 4.4.

Limitation imposed on the spectrometer data

All coincidence measurements on ^{3}He were performed with the '70x70' slit. The out-of-plane acceptance, θ_{tg}, is reduced further by geometric limitations inside the QDQ to $\theta_{tg} > -60$ mrad. Software limitations on θ_{tg} or ϕ_{tg} were imposed during the analysis at ±150 mrad to eliminate events not originating from the target.

In the analysis of the coincidence data, the acceptance in y_{tg} has been limited to $-8 < y_{tg} < 8$ mm. This is well inside the region were the reconstruction of y_{tg} can be assumed to be reliable (based on the information in Fig. 4.2). The cut is also sufficient to reduce to contribution of cell-wall events to the coincidence data below the 1.4% level for all kinematic settings (see section 4.3).

Due to geometrical limitations, part of the focal plane cannot be reached by particles without obstruction. Therefore, the useful range of X1 has been limited in the analysis to $528 < \text{X1} < 4200$ fine-channels – a momentum acceptance of 9.5% – as determined from a quasi-white spectrum measured at the LQ kinematic setting.

Detection efficiency

The efficiency of the QDQ spectrometer is determined by various ingredients: the electron detection efficiency of the wire chambers, scintillators, the frontend electronics, the detector trigger and the reconstruction efficiency in the off-line analysis.

The MWDC and scintillator efficiencies were optimized at the beginning of the experiment. A fixed dead time of 500 ns has been introduced to ensure proper event readout; a prompt trigger output with negligible dead time is provided to determine the fraction of events lost. The trigger live time during the experiment was better than 99.5%.

The variation of the detection efficiency as a function of focal-plane position was investigated by performing (e, e') scattering experiments on ^{12}C, such that the peak corresponding to elastically scattered electrons was located at different positions along the focal plane. For each measurement, the cross section was determined. Relative variations between the various measurements were found to be less than 1%.

The absolute detection efficiency was determined using elastic scattering from ^{12}C at different spectrometer angles. The collected charge was determined, taking into account the duty-factor dependence of the beam current measurement. The measured cross sections were compared to calculations based on a 15-parameter Fourier-Bessel parametrization of the charge distribution [Vri87]. The efficiency was found to be 96% [Lappc, Sta99b]; the statistical and systematic uncertainties amount to 2% and 3%, respectively.

4.2 Analysis of HADRON data

The procedure to convert raw event fragments, originating from the HADRON readout electronics, to proton momentum vectors is similar for both detectors used.

Determination of proton momenta

The methods employed to convert the measured ADC information to the light produced in the scintillator at the impact point, as well as the way to treat particles impinging on the detector under different impact angles are already extensively described elsewhere [Lee96, Ond98b, Sta99b]. In summary, the effective gain of the photomultiplier (PM) is determined by comparing ADC distributions measured in subsequent layers with light-production calculations based on the Bethe-Bloch energy-loss formula and the energy-to-light parametrization due to Wright [Wri53]. The attenuation along the scintillators is accounted for by determining the response at various values of the distance from impact point to PM. For the horizontally segmented layers the impact position relative to the PM is obtained from the perpendicularly segmented hodoscope H2. For the calibration of H2 itself, selections are made based on L1. The light yield estimate is phenomenologically corrected for impact-angle effects. Using this procedure, an effective quantity L_{norm}, labelled 'normalized light', is obtained.

Particle identification

The identification of proton events in the detector is performed in two steps. Firstly, tracks are identified using the procedures described in, *e.g.*, [Lee96], where it should be noted that no self-timing restrictions on L1 are imposed in the analysis to avoid ambiguity in determining the correction for 'cross-over' events in this layer [Kas97]. Secondly, based on the amount of normalized light in the stopping layer, the estimated amount of light a proton should have produced in the preceeding layer is calculated. The difference, ΔL, between this calculated amount of light and the measured yield results in a distribution which peaks around zero for protons. A window on ΔL is used to suppress non-proton events in the analysis. This gate is set in such a way that more than 99% of the protons will be identified correctly, which however implies that a fraction of the non-proton events will incorrectly be flagged as proton. These events are eliminated after subtraction of the accidental coincidences (see section 4.3).

Timing corrections

In the analysis, the arrival time of the HADRON detector trigger, as measured by the CD, is corrected for time-of-flight of the proton and for various time-differences occurring in the proton detection system. In this way, the departure time of the proton at the vertex is determined,

$$t_{dep} = t_{\mathrm{ATR}} - t_{tof}(T_p, \alpha) - t_{walk}(\mathrm{ADC}) - t_{prop}(i_{\mathrm{H2}}) - t_{\mathit{off}}(i_{\mathrm{L1}}), \tag{4.1}$$

using a phenomenological method to account for effects on the time-of-flight that depend on the impact angle α. The determination and use of the various correction factors are described in, *e.g.*, [Sta99b]. The total effect of the timing correction varies between 4 and 18 ns, primarily determined by the time-of-flight correction (4 to 11 ns).

The correction factors partially depend on the calibration parameters used in the energy determination. As these parameters were optimized for each kinematic setting separately, also the timing corrections were determined on a per-kinematics basis. The optimal resolution obtained is 0.72 ns (FWHM) for data taken at the one-hour time scale. A typical coincidence time distribution is shown in Fig. 4.4.

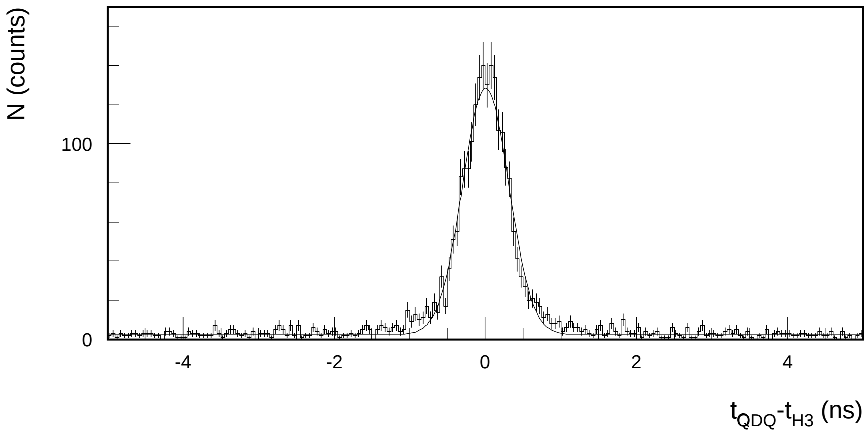

Figure 4.4: *Time-difference distribution for two-fold coincidental events QDQ–HADRON3. The resolution amounts to 0.72 ns FWHM. (data: LQV, taken over a period of one hour)*

Long-term variations of the peak position in the coincidence time distribution were observed for data taken in a single kinematic setting. This effect, which occurs at a time scale of several days, deteriorates the resolution and thereby reduces the real-to-accidental ratio. Only the time-difference distribution for QDQ–HADRON3 coincidences is subject to this problem, which suggests it is due to the readout electronics of HADRON3 being located far away (60 m) from the detector proper, whereas the readout systems for QDQ and HADRON4 are located within several metres from their respective detection systems. As the real-to-accidental ratio for QDQ–HADRON3 coincidences is extremely good and variations are not more than 0.7 ns, this effect was taken into account by choosing wider time-difference windows in the coincidence analysis; the real-to-accidental ratio for $(e, e'pp)$ events is primarily determined by the ratio for QDQ–HADRON4 coincidences, which was not affected.

Detection efficiency

The efficiency of the HADRON detector is determined by various effects: electronics live time, deficiencies in the reconstruction procedure, and by multiple-

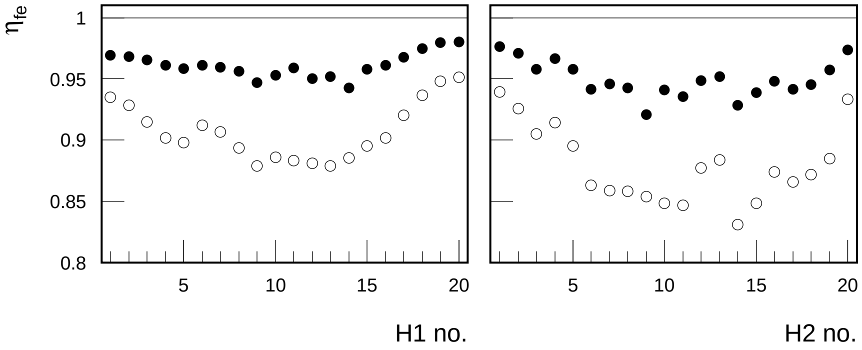

Figure 4.5: *Live time of the frontend electronics of HADRON4 for both hodoscope layers, when a hit from both sides of any element is required. Data were taken at two different values of the luminosity. The solid dots correspond to an average current of 0.5 μA, the open dots to 1.5 μA. (Data: LQA)*

scattering and hadronic interactions of the protons in the detector. The efficiencies are monitored during the experiment or estimated using a model-description of the detector. Independent checks are performed using the kinematically overdetermined ^{1}H$(e, e'p)$ reaction and by performing measurements at the same kinematic setting, but at different luminosities.

As described in section 3.4, the live time of the frontend electronics is determined using test pulses as a monitor This live time depends on the instantaneous luminosity and is therefore determined on a per-file basis. The influence of luminosity variations is illustrated in Fig. 4.5. The live time is lowest in the two hodoscope layers. The fluctuations among elements within the same layer are due to variations in the solid angle subtended by the elements (which decreases as the elements are located further away from the detector heart line), to the frontend thresholds set and to the angular dependence of the singles count rate.

Since multiple frontends are involved in the detection of a particle track, the *track live time* is determined as the product of the live times of the frontends that are part of the track. In using this method, a small overcorrection will result from correlated frontend live times. As the main contribution to the track live time is due to the hodoscopes (which are oriented perpendicular to each other and are therefore hardly correlated), and the frontend live time of the stopping layers is close to 100%, the effect of correlated dead time to the track live time is estimated to be less than 1%.

Also with the detector trigger a live time is associated, which like that of the frontends, depends on the luminosity. This inefficiency is determined by measuring the number of prompt triggers (which have a negligible dead time) and the number of generated detector triggers (ATRs). The trigger live time – the ratio ATR over prompt triggers – amounts to about 85%. It is recorded on a file-by-file basis and used as such in the analysis.

To avoid ambiguities in the reconstruction of particle tracks and in the timing corrections to be applied to the arrival time of the detector trigger, those events in which more than one element of L1 fired (multiple-hit, MH) are disregarded in the analysis. Also tracks in which more than one of the H1 candidate elements was hit, are ignored. A count of the number of MHs in L1 is kept. As in almost all cases (97%) MHs are due to particles crossing the edge between two neighbouring L1 elements (cross-overs), the efficiency is determined to be

$$\eta_{\mathrm{MH}}(i_{\mathrm{L1}}) = 1 - \frac{1}{2}\frac{n_{\mathrm{MH}}(i_{\mathrm{L1}})}{n_{event}}. \tag{4.2}$$

Here $n_{\mathrm{MH}}(i_{\mathrm{L1}})$ is the number of MHs in the i-th element of L1, and n_{event} the total number of events detected. The correction is determined and applied to the data on a per-file basis.

An additional inefficiency and source for possible misreconstruction of detected protons are interaction processes occurring in the flight-path of the particles, especially in the shielding material.

Firstly, hadronic interactions among the impinging protons and nuclei in the shielding and scintillator material will occur. The energy loss suffered due to both elastic and inelastic scattering may be so large, that the protons subsequently fail to reach L1 and thus will not generate a trigger, a process which will primarily affect protons with energies near the detection threshold. Energy losses can also result in loss of a proton – when it fails the particle identification procedure – and lead to misreconstruction of its incident energy.

Secondly, multiple-scattering may lead to extremely large angular variations in such a way that the proton either escapes from the detector at the sides or is stopped outside the candidate array used in the analysis. These proton tracks will not be reconstructed by the analysis procedure.

To account for the aforementioned inefficiencies, a model description of both HADRON detectors is made using the detector description and simulation tool GEANT [Gea94]. In this model, the geometries of the target system and scattering chamber, and the description of the detector housing and scintillator package are implemented. Using the simulation capability of GEANT, protons with a uniform energy and angular distribution are generated within a solid angle slightly larger than the one spanned by the detector collimator. The vertices are also uniformly distributed over a line of 50 mm along the beam path to account for the extension of the target. The light output of all elements is simulated and subsequently converted to ADC values. For this conversion, gain parameters as determined from the real data are used. The digitized values are stored in a pseudo-event format compatible with the one produced by the event builder.

The generated pseudo-data are treated like regular data in the analysis procedure. The efficiency due to interaction processes is defined as the number of protons accepted by the analysis procedure over the number of generated particles. This efficiency is dependent on the proton energy and on the impact angle of the particles on the detector (and thus the effective thickness of material seen). The correction factors are therefore determined for intervals in T_p and impact angle α of 5 MeV and 1°, respectively.

Care should be taken not to implicitly apply the MH correction twice, as most MHs are cross-over events due to real protons. The efficiency is therefore separated in two parts. The hit-efficiency η_{hit} is defined as the probability that a proton, originating form the target, will reach H1. The reconstruction efficiency η_{rec} measures the probability that a proton, which hits only one L1 element and one of the corresponding H1 elements, is properly identified as such by the analysis procedure. The product of these two efficiencies is applied as a correction factor to the data.

The amount of light produced by protons in the stopping layer may remain below the detection threshold. In this case, the analysis procedure will incorrectly identify the previous layer as the stopping layer and an attempt will be

Table 4.1: *Overview of ^{1}H$(e, e'p)$ measurements performed with HADRON3. The variable η_{total} is the ratio of the number of measured protons over the expected yield, after all corrections have been applied to the HADRON data. The uncertainties shown are statistical only.*

file ID	$\theta_e(^\circ)$	$\theta_p(^\circ)$	T_p (MeV)	$\eta_{hit \cdot rec}$	η_{trig}	η_{MH}	η_{total}
464	47	54	90	0.91	0.92	0.91	95.6±2.9%
465	47	54	90	0.91	0.92	0.91	95.4±2.7%
466	47	60	90	0.91	0.94	0.92	97.3±2.9%
468	47	60	90	0.91	0.94	0.92	101.3±3.1%
469	57	54	120	0.86	0.92	0.92	99.0±3.7%
470	57	54	120	0.86	0.92	0.92	97.8±3.6%

made to determine the identity of the proton under this false assumption. The windows used for the particle identification are sufficiently wide to accept these events and no protons will be lost. However, the reconstructed energy will be slightly too small. This redistribution will deteriorate the resolution, but will not cause loss of yield for the $(e, e'pp)$ events under study.

Verification of the efficiency correction

Verification using the reaction ^{1}H$(e, e'p)$

To verify the efficiency corrections applied to the HADRON singles data, measurements were performed with a hydrogen target. As the ^{1}H$(e, e'p)$ reaction is kinematically overdetermined and the acceptance of the HADRON detector is much larger than the proton cone corresponding to the acceptance of the QDQ electron spectrometer, every elastically scattered electron inside the QDQ acceptance should lead to a proton being detected in HADRON. During this experiment, ^{1}H$(e, e'p)$ measurements were performed with the QDQ and HADRON3 under three different kinematic conditions, listed in Table 4.1. The target cell used for the ^{1}H$(e, e'p)$ measurements is identical to the one used during the ^{3}He$(e, e'pp)$ measurements. The density of the hydrogen gas was 0.34 mg/cm^3.

As the energy of the emitted protons is strongly dependent on the scattering angle of the electron, the QDQ acceptance was limited to ±20 mrad in-plane,

±30 mrad out-of-plane and a y_{tg} acceptance of ±4 mm. The energy distribution of the scattered electrons was corrected for energy variations due to the finite angular acceptance (*kinematic correction*). A cut of ±4 MeV was used around the peak in the electron energy distribution to eliminate events which suffered a large energy loss due to radiative effects.

The corrections applied to the HADRON data are determined in a way identical to that for $(e, e'pp)$ data. Trigger, frontend and MH correction factors are determined on a per-file basis. The model-dependent efficiencies (η_{hit} and η_{rec}) are taken from a simulation with a ^{3}He gas target. Although the density of the hydrogen gas is much lower, this change has only minor influence on the correction factors calculated.

No accidental coincidences are observed in the time difference distribution for QDQ–HADRON3 events. The total reconstruction efficiency η_{total} is thus determined directly from the corrected number of reconstructed protons. Besides the statistical error quoted in Table 4.1, a systematic error of 4% has to be associated with these measurements due to uncertainty in the detector simulation and correlated *track* live time (see section 4.6). As the reconstructed efficiency is compatible with one within the statistical and systematic error, no additional correction factor was applied to the ^{3}He$(e, e'pp)$ measurements.

Verification by luminosity variations

As some sources of inefficiency depend on the instantaneous luminosity (track live time and trigger live time), the validity of their corrections can be investigated by repeating the measurements at different values of the luminosity. The test was performed during the measurement of LQA, as this setting features the highest count rate. In Fig. 4.6, the number of fully corrected, true three-fold coincident $(e, e'pp)$ events per unit charge is displayed for all datafiles measured at LQA. All conditions, except the incident beam current, are kept constant. Data files up to and including no. 334 were measured with an incident current of 1.5 μA; the current was changed to 0.5 μA from file 335 onwards. The correction factor applied to the data varies from 1.95 at the high current to 1.25 at the low current measurements. The reconstructed numbers of true $(e, e'pp)$ events per unit charge are consistent: 174±2.8 and 178±3.9 at an incident beam current of 1.5 and 0.5 μA, respectively.

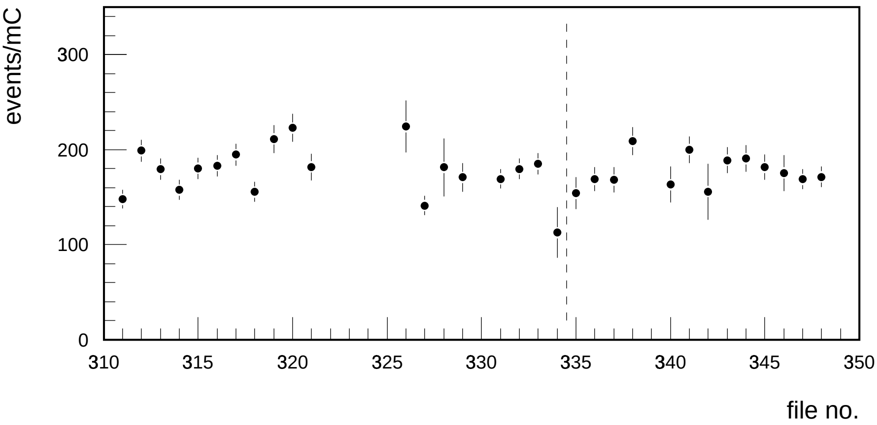

Figure 4.6: *Number of true* $(e, e'pp)$ *events per unit charge, as determined on a file-by-file basis for the LQA kinematic setting. All correction factors described have been applied to the data. The dashed line indicates the change in luminosity from 1.5* μA *up to file no. 334 to 0.5* μA *from file no. 335 onwards.*

Recuperation of lost H2 information in the LW kinematics

During the measurement of the LW kinematic setting, the combination process of sub-event fragments in the HADRON4 data acquisition chain occasionally selected the wrong sub-event in one specific crate out of the four. This crate contained all but three digitizer modules for H2, the hodoscope layer sensitive to the out-of-plane direction. No digitizers from other layers were contained in this crate.

In 20% of the cases the sub-event supplied by this crate did not belong to the requested event, but to an uncorrelated other event. The problem became apparent during the frontend efficiency determination, which showed a 20% reduced efficiency for a number of elements, all located in the same crate. This is illustrated in Fig. 4.7. Such an effect is only visible for test pulses and laser events as these show a characteristic hit pattern throughout the complete detector. It can safely be assumed that this miscollection of sub-events also affected the regular data. As it cannot be determined which events are affected, all in-

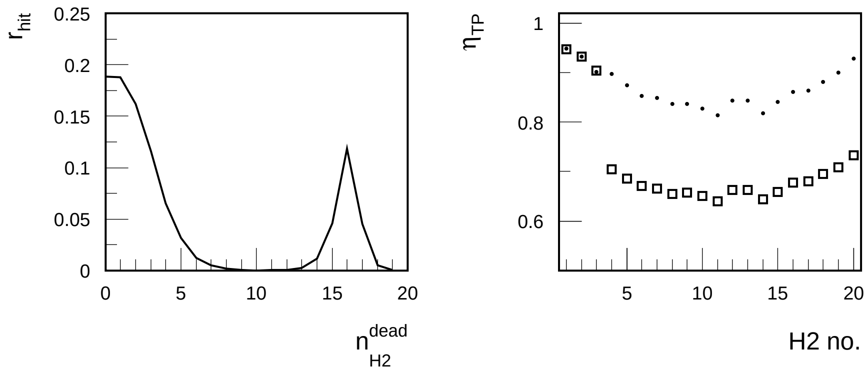

Figure 4.7: *The effect of event miscollection on the frontend live time. The left panel shows the frequency distribution of the number of non-responding H2 elements per test pulse event. The right panel shows the apparent frontend live time. Open squares represent the estimated live time determined using all test pulse events, the solid dots using only those test pulse events in which at least 10 elements are alive,* i.e., *those in the peak on the left-hand side in the left panel. (Data: LW, file 715)*

formation originating from this crate had to be discarded in the analysis. To retain consistency among all analysed events, also the information originating from the three unaffected H2 elements was discarded.

The H2 impact information is used in the analysis for several purposes: *i)* in the gain determination for the elements of all other, vertically mounted, layers via the attenuation, *ii)* in the timing corrections by the propagation-time parametrization, *iii)* in the determination of the out-of-plane angle of the proton momentum vector, *iv)* for identification of protons stopping in L1; here, the exact ADC values of the H2 elements are needed.

As the miscollection problem was present in more than 90% of the measurements performed at the LW settings, it was considered worthwhile to try to recover the lost H2 information. A partial reconstruction of the out-of-plane information is possible because of the double-sided readout of the perpendicularly mounted hodoscope plane H1. Propagation time differences within the elements of H1 are used to reconstruct the impact position with an accuracy of about 50 mm.

The ADC information of H2 is permanently lost and therefore no particle identification can be performed for protons stopping in L1. In the analysis for LW, these protons are therefore not used. This raises the effective proton-detection threshold to protons stopping in L2. Taking into account the 1.0 mm steel shielding used during LW, the threshold becomes 53 MeV (compared to 36 MeV for L1 stoppers). The remainder of this section will be concerned with the method developed to recover the H2 hit-information.

The method to reconstruct the out-of-plane information proceeds in several steps:

- Parametrize the propagation-time difference for each H1 element, such that the time difference can be used to calculate the corresponding H2 element number. Use the reconstructed H2 number to perform light-attenuation corrections, timing correction and determination of the out-of-plane angle.
- Determine the additional frontend live time of every H1 element. In the regular analysis, only one of the two H1s needs to fire in order to obtain a valid event. As both are needed now to do the H2 reconstruction, an additional live time has to be corrected for.
- Determine the efficiency of this procedure using data files with valid H2 information.

The data produced by the frontend electronics contain the difference between hit arrival time and the arrival of the time-stop signal from the global detector trigger. This time-stop signal has a fixed time relation to the hit arrival time in the L1 element. If we consider valid events, only one L1 and one H1 strip are involved in the event. In this case, the difference in arrival time between the two sides of H1 is correlated with the impact position due to the propagation time of the light inside the scintillator.

The correspondence between H1 time difference and the H2 impact position was determined for each H1 strip separately. A plot of the relation between Δt_{H1} and the H2 number is shown in Fig. 4.8. This relation was parametrized with a straight line and used in the analysis of the affected files. The difference between

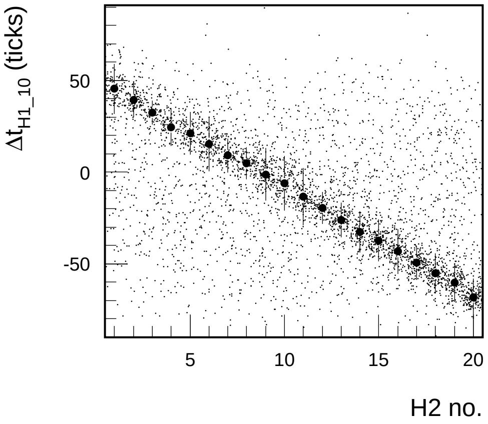

Figure 4.8: *Time difference between hits arriving on the top-side and bottom-side PM of an H1 element as a function of the element number as determined in the regular-type analysis. The error bars indicate the width (FWHM) of the time difference distribution. (Data: IW, file 685)*

the H2 number determined with this procedure as compared to the regular one is displayed in Fig. 4.9.

The detector trigger for HADRON4 is a coincidence between a hit in an L1 element and a hit in any of the four corresponding H1 PMs. In the regular analysis, the only additional requirement is that just one H1 strip was hit. It is therefore not necessary that both sides of this H1 element have a valid signal.

However, to perform the H2 reconstruction, a signal from both sides of the H1 strip is required. This induces an additional inefficiency, corresponding to the ratio of the live time for the H1 element, when requiring a signal from both frontends, compared to the live time for this H1 element when only one frontend is required. This additional live time effect is determined per H1 strip and amounts to 92.7% on average.

For several files from IW, the effectiveness of this alternative procedure is determined using HADRON4 single events. Only true protons stopping in L2 and beyond are taken into account in the comparison. The amount of true

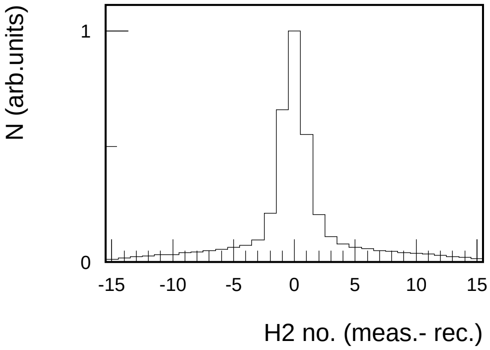

Figure 4.9: *Difference between the tracking H2 element as determined by the regular analysis and by using H1 time difference information. (Data: file 685)*

protons recovered is 99.4±0.8%. It is therefore assumed that this reconstruction procedure is sufficiently accurate to be used in the analysis of the $(e, e'pp)$ events.

4.3 From counts to yield

As described earlier in section 3.5, the differences in the arrival times of the various detector triggers are used to discriminate the different types of events: single events, two-fold coincidences among the various detector combinations, and three-fold coincident events. Within the coincidence detector these different event types are selected by time difference. A time difference of ±125 ns between every pair is allowed for by the coincidence detector (CD).

The arrival times measured by the CD are corrected for detector-dependent timing corrections to yield the departure times of the particles from the vertex. For the events flagged as three-fold coincident by the CD, the difference in the departure time between the electron trigger and the proton in either forward (H3) or backward (H4) direction is shown in Fig. 4.10.

In this figure, several kinds of events can be discriminated. The peak, located at a time difference of 0 ns for both combinations, corresponds to real three-fold coincidences. The two ridges at Δt_{QH4}=0 ns and Δt_{QH3}=0 ns are due to real $(e, e'p)$ coincidences between the scattered electron and either the

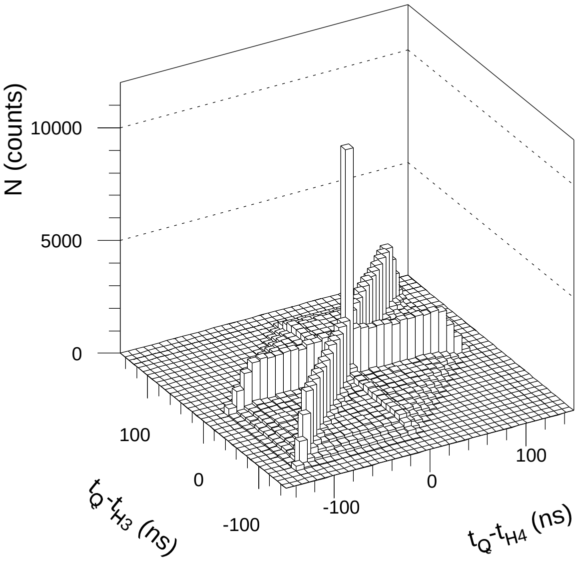

Figure 4.10: *Time difference distribution for three-fold coincident events. The binning has been chosen to enhance visibility and does not reflect the resolution with which the distribution was measured. The resolution amounted to 1.5 ns (FWHM). (Data: LQA)*

backward or forward proton detector together with an accidental third. The ridge at $\Delta t_{\mathrm{QH4}} = \Delta t_{\mathrm{QH3}}$ contains real two-proton coincidences together with an accidental electron trigger. The structures are located on a flat background of events that are three-fold uncorrelated.

To extract the true $(e, e'pp)$ events, the contributions of the flat background and the ridges to the region of the real coincidences has to be estimated. This is best performed by symmetrizing the coincidence time spectrum by a linear transformation

$$\tau_x = \frac{1}{\sqrt{3}} \left(2t_{\mathrm{H4}} - t_{\mathrm{Q}} - t_{\mathrm{H3}}\right) \tag{4.3}$$

$$\tau_y = \left(t_{\mathrm{Q}} - t_{\mathrm{H3}}\right). \tag{4.4}$$

After this transformation, the time difference distribution will exhibit a symmetric hexagonal shape as displayed in Fig. 4.11. The width b is chosen in such a

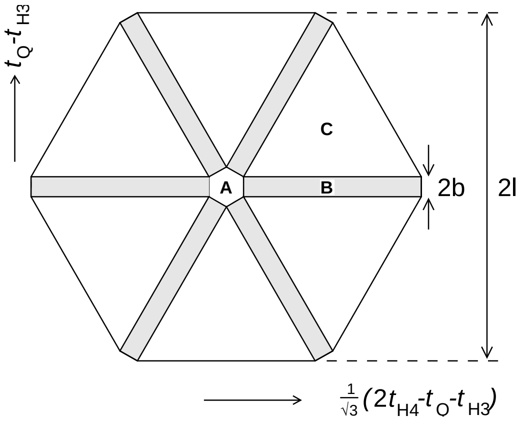

Figure 4.11: *A hexagonal shape is obtained after the coincidence time distributions are symmetrized.*

way that the full width of the two-fold coincidence band is well within the regions B. As the coincidence time resolution is always better than 1.5 ns (FWHM), b was chosen to be 3 ns, *i.e.*, at least 4.5σ from the peak. The value of l determines the accuracy with which the accidental level inside the real region A can be estimated. The accuracy is largely determined by the statistical uncertainty on the two-fold coincident events in the B regions, as these will contribute most to area A. The length l was chosen to be 60 ns. This is still well within the acceptance of the CD.

The number of true $(e, e'pp)$ events is determined by the number of events in region A, reduced with the estimated contribution from B and C,

$$N_T = N_A - f_B N_B - f_C N_C, \tag{4.5}$$

where the fractions f_B and f_C are derived from the lengths and areas of the regions A, B, and C [Ond98b, Sta99b]. The fractions f_B and f_C are subsequently used as weights in the summation of the events. Events outside the regions A, B and C are discarded.

Contributions from cell walls

The ^{3}He target, described in section 3.2, is a cylindrically shaped container made of aluminium with a diameter of 50 mm. Hence, the cell walls will be

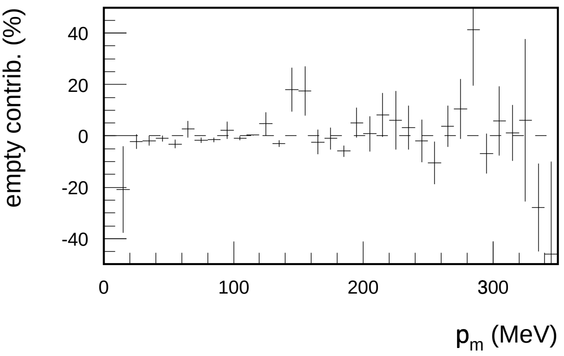

Figure 4.12: *Relative contribution of the cell wall to the total* $(e, e'pp)$ *yield for kinematics LQA as a function of the missing momentum. The empty-target data was analysed in the same manner as the* ^{3}He$(e, e'pp)$ *data.*

within the acceptance of the QDQ spectrometer for electron detection angles below approximately 30°. Under these circumstances, true ^{27}Al$(e, e'pp)$ events originating from these cell walls will contribute to the measured yield of $(e, e'pp)$ events. The contribution from these cell wall events has been reduced by limiting the y_{tg} acceptance of the spectrometer to ±8 mm, as explained in section 4.1.

The contribution of cell wall events will be most prominent for kinematics LQ, where the spectrometer angle was set at 27.7°. To determine this contribution, dedicated measurements were performed with an empty target cell. The kinematic conditions were kept identical to those of the coincidence measurement. For the empty-cell measurements in the LQA kinematics, a charge of 15.6 mC was collected, which corresponds to more than 15% of the total charge collected on the ^{3}He gas in this kinematic setting. The contribution to the total yield (after applying the usual correction factors) originating from the cell walls was 1.4±0.7% for the excitation energy region from -11 to 14 MeV, independent of the missing momentum p_m. The relative contribution from the cell walls to the corrected yield is shown in Fig. 4.12.

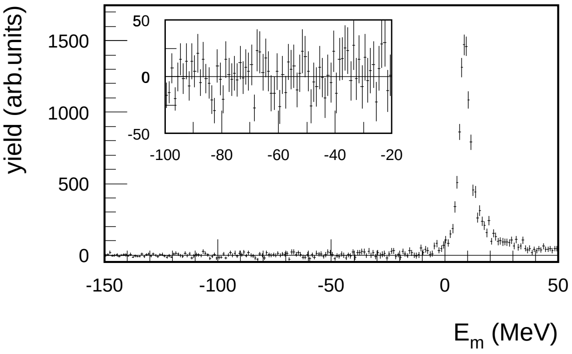

Figure 4.13: *Missing-energy distribution for kinematics LQA. The resolution amounts to 5.5 MeV (FWHM). The inset shows an enlargement of a subset of the same distribution. The yield in the E_m region between -100 and -20 MeV is -1.1±1.7.*

Verification of the subtraction procedure

The proper subtraction of accidental coincidences is verified using the missing-energy distribution of the true $(e, e'pp)$ coincidences. Below the value corresponding to the two-proton separation energy, in this case the binding energy of ^{3}He, no true $(e, e'pp)$ events can occur. The strength in the region below this energy should be compatible with zero. For kinematics LQA, the missing-energy distribution for true $(e, e'pp)$ events is shown in Fig. 4.13. The peak corresponding to the three-body breakup of ^{3}He is located at E_m=7.7 MeV. The tail extending to higher E_m values is caused by energy loss suffered by the incident or scattered electron due to radiative processes. The inset shows an enlargement of the E_m distribution for the range $-100 < E_m < -20$ MeV. The yield in this region, -1.1±1.7, is compatible with zero.

4.4 From yield to cross section

The cross section for the reaction ^{3}He$(e,e'pp)$ is determined as a function of the kinematic quantities described in section 2.1, *e.g.*, ω, p_m, $p_{\mathit{diff},1}$, or p_{ij}. The eight-fold differential cross section is defined as

$$\frac{d^8\sigma}{dV^8}(\Delta\boldsymbol{X}) = \int_{E_x} \frac{N(\Delta\boldsymbol{X})}{\int\mathcal{L}\,dt\,\mathcal{V}(\Delta\boldsymbol{X})} \left|\frac{\partial T_2}{\partial E_x}\right| dE_x. \tag{4.6}$$

In this equation, $\Delta\boldsymbol{X}$ refers to a range of values of (a set of) kinematic quantities in which the cross section will be represented, *e.g.*, $\Delta\boldsymbol{X} = (\Delta p_m, \Delta p_{\mathit{diff},1})$. $\int\mathcal{L}dt$ represents the integrated luminosity, $N(\Delta\boldsymbol{X})$ the number of true $(e,e'pp)$ events, and $\mathcal{V}(\Delta\boldsymbol{X})$ the experimental detection volume in phase space. The factor $|\partial T_2/\partial E_x|$ is a Jacobian.

The integrated luminosity, $\int\mathcal{L}\,dt$, is the product of target thickness and collected charge. This collected charge was measured for each data file and summed. The density of the ^{3}He gas was determined by elastic scattering from ^{3}He (see section 4.5). The reduction of the target thickness due to the varying acceptance of the QDQ spectrometer along y (see section 4.1) is taken into account in the calculation of the experimental detection volume $\mathcal{V}$ and therefore the nominal thickness (*i.e.*, the density times the diameter of the cell) is used in determining the integrated luminosity.

The total ^{3}He$(e,e'pp)$ yield that contributes to the selected domain $\Delta\boldsymbol{X}$ is represented by $N(\Delta\boldsymbol{X})$. It takes into account the correction factors due to inefficiencies and incorporates the random subtraction:

$$N(\Delta\boldsymbol{X}) = \sum_i \frac{w_i(\tau_x,\tau_y)}{\epsilon_i} D(\boldsymbol{X}_i;\Delta\boldsymbol{X}), \tag{4.7}$$

where w_i accounts for the random subtraction, ϵ_i for the detector efficiencies and $D(\boldsymbol{x};\boldsymbol{R})$ is a two-valued function, that has the value 1 if $\boldsymbol{x}$ is inside the region $\boldsymbol{R}$, and zero everywhere else. The sum $\sum_i$ loops over all three-fold coincident events inside the regions A, B, and C.

With the experimental setup used, not every interval $\Delta\boldsymbol{X}$ is equally likely to be hit. This detection volume $\mathcal{V}(\Delta\boldsymbol{X})$ in phase space is defined as

$$\mathcal{V}(\Delta\boldsymbol{X}) = \int D(\boldsymbol{X}'(\boldsymbol{v});\Delta\boldsymbol{X})D(\boldsymbol{v};\boldsymbol{A})\,d\boldsymbol{v}. \tag{4.8}$$

In this equation, $\boldsymbol{X}'(\boldsymbol{v})$ is the vector of observables determined from the integration variable $\boldsymbol{v}$, $\boldsymbol{A}$ is the acceptance region of the combined three-detector setup, and the integration variable $\boldsymbol{v}$ represents $(\boldsymbol{p}'_e, \boldsymbol{p}'_1, \boldsymbol{p}'_2, y_{beam})$. The integration is carried out over the complete phase space. The dependence of $\boldsymbol{X}'$ on $\boldsymbol{v}$ is such, that the integration is best performed numerically.

Integration over the excitation-energy range

The quantity $N/\mathcal{V}$ of Eq. 4.6 is a nine-fold differential, $dT'_e\, d\Omega'_e\, dT'_1\, d\Omega'_1\, dT'_2\, d\Omega'_2$. To obtain the eight-fold differential cross section, it is integrated over the excitation energy E_x. This introduces a Jacobian, which in the $(e, e'pp)$ case can be expressed as:

$$\frac{\partial T_2}{\partial E_x} = \left[1 - \frac{E_2}{E_{rec}} \left(\frac{(\boldsymbol{q} - \boldsymbol{p}'_1) \cdot \boldsymbol{p}'_2}{|\boldsymbol{p}'_2|^2} - 1 \right) \right]^{-1}, \tag{4.9}$$

where E_2 and E_{rec} are the total energy of proton 2 and the recoiling neutron, respectively. As this Jacobian depends on the individual proton momenta, it is applied as a weight factor to the data on an event-by-event basis.

Not the entire region in E_x is integrated to determine the cross section as – except for resolution effects – the region below E_x=0 MeV does not contribute to the cross section for ^{3}He$(e, e'pp)$. To reduce the total statistical error due to the contribution of these events, the region $E_x < -11$ MeV is disregarded in the integration. This corresponds to more than 4σ from the position of the peak.

The events in the region at $E_x > 0$ MeV are due to true ^{3}He$(e, e'pp)$ events and include events of which either the incident or the scattered electron suffered energy loss due to the emission of photons, which results in a reconstructed E_x that is systematically larger. The shape of this radiative tail as a function of the excitation energy is readily calculated using the formalism of [MoT69].

The upper integration limit was set at E_x=14 MeV. For each kinematic setting, the fraction of events beyond this cutoff was calculated and applied as a correction factor to the data; they vary from 1.14 to 1.16.

In selecting this region in excitation energy, the uncertainty due to radiative effects on the other kinematic quantities is limited. The missing momentum p_m will be most strongly affected, but the variation is still limited to ±4 MeV/c on average, which is smaller than the bin-width used in the presentation of the cross section. The effect on the determination of γ_1 is estimated to be smaller than the angular resolution of the HADRON detectors.

Because of limitations imposed by the analysis software, the integration over the E_x interval is performed on the measured yield and the detection volume separately. As the variation of the detection volume $\mathcal{V}$ with E_x is small within the relevant range, its value is approximated by a constant $\tilde{\mathcal{V}}$ and taken out of the integration:

$$\frac{d^8\sigma}{dV^8}(\Delta\boldsymbol{X}) = \frac{1}{\int\mathcal{L}\,dt\,\tilde{\mathcal{V}}(\Delta\boldsymbol{X})\rfloor_{E_{equiv}}} \int_{E_x} N(\Delta\boldsymbol{X}) \left|\frac{\partial T_2}{\partial E_x}\right| dE_x. \tag{4.10}$$

The eight-dimensional volume $\tilde{\mathcal{V}}$ is evaluated at a specific value of E_x=E_{equiv}, such that the differential cross section, evaluated using equation 4.6 is identical to the cross section evaluated using Eq. 4.10. Due to the radiative tail of the distribution, this value does not correspond to E_x=0, but to a slightly higher value. This value was determined to be E_{equiv}=2 MeV and is identical for all kinematic settings, as the shape of the radiative tails is similar.

Determination of the experimental detection volume

To evaluate the detection volume $\tilde{\mathcal{V}}$, a numerical integration of equation 4.8 is performed. The generic code Q2HPHASPA is used, which evaluates the nine-dimensional integral for the volume spanned by the QDQ and both HADRON detectors using a Monte-Carlo method. The code determines $\mathcal{V}$ by

$$\mathcal{V}(\Delta\boldsymbol{X}) = \frac{N^{MC}(\Delta\boldsymbol{X})\,\mathcal{V}^{MC}}{N^{MC}_{total}}, \tag{4.11}$$

where $\mathcal{V}^{MC}$ is the volume of the hypercube, which can be calculated analytically. N^{MC}_{total} is the total number of samples drawn from the volume $\mathcal{V}^{MC}$, and $N^{MC}(\Delta\boldsymbol{X})$ the number of samples for which $\boldsymbol{X}'$ is within the volume $\Delta\boldsymbol{X}$.

For each detector, a momentum vector is generated randomly inside its acceptance from which relevant physical quantities $\boldsymbol{X}'$ are constructed. These Monte-Carlo events are sorted in intervals identical to the ones used in the projection of the measured data. The generated events originate from different positions along the beam line to account for the extended target. The volume $\tilde{\mathcal{V}}(\Delta\boldsymbol{X})$ is subsequently obtained by selecting a region ΔE_x having a width of

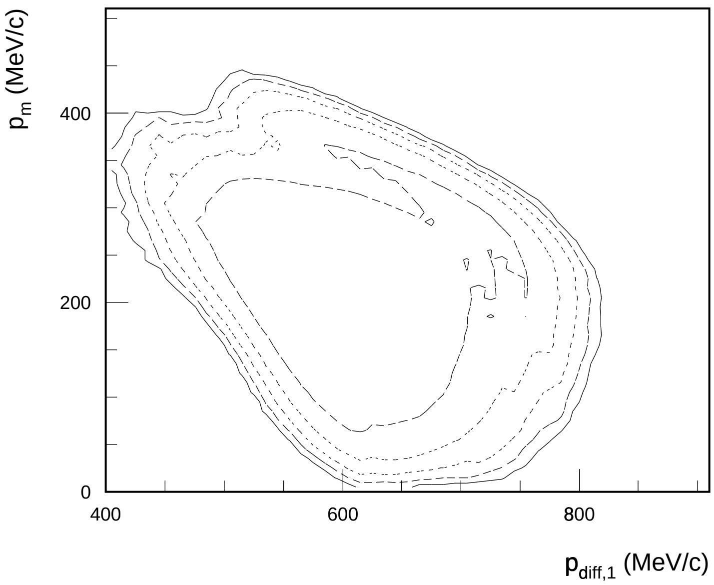

Figure 4.14: *Contour plot of the detection volume* $\tilde{\mathcal{V}}$ *as a function of* $(p_m, p_{diff,1})$ *for the combination of the kinematic settings LQA, LQV, and PEF. Contours are drawn at 30%, 10%, 3%, 1%, and 0.3% of the maximum value.*

10 MeV and centred around the equivalent energy E_{equiv}=2 MeV. This width is such that further reduction does not change the value of $\tilde{\mathcal{V}}$ by more than 1%. In Fig. 4.14, the volume $\tilde{\mathcal{V}}$ is shown for $\boldsymbol{X} = (p_m, p_{diff,1})$ for the combined kinematic settings at LQ.

In total 10^8 events were generated inside the nine-dimensional volume $\mathcal{V}^{MC}$ for every kinematic setting. This ensures that the contribution of the Monte-Carlo sampling error to the statistical uncertainty in the cross section is less than 0.4%.

QDQ volume

The angular acceptance of the QDQ is limited by an octangular slit with a central acceptance of ±70 mrad in both directions. However, the QDQ is not capable of viewing the entire length of the target with complete coverage of this angular domain. As the QDQ is the only detector with such a limited y acceptance, the effective y acceptance of the $(e, e'pp)$ detection volume is accounted for by an effective solid angle of the QDQ.

Sample events are drawn uniformly inside a cone with an angular span of 85 mrad, originating from vertex positions $-25 < y_{beam} < 25$ mm. Using the parametrization of the QDQ acceptance, as described in section 4.1, the effective solid angle of the spectrometer is determined.

The energy acceptance along the focal plane is independent of the angles of the electron within the relevant domain and can therefore be generated uniformly over the X1 acceptance.

HADRON volume

The HADRON detector may be thought of as being composed of a large number of rectangular detectors. Every combination of H1 and L1, and H2 in itself represents an active detection element with a solid angle and an energy acceptance. This solid angle, which depends on the H1–H2 combination, can be calculated analytically. The energy acceptance, however, is more complicated, as it depends on the impact angle of the particle. Therefore, this acceptance is evaluated using uniformly distributed samples between the lowest possible energy (at an impact angle of zero degrees) and the largest possible one (at the maximal impact angle). The actual energy limits are thus predetermined for each active element. The extension of the target is taken into account in the calculation of the momentum vector by segmenting the extension of the target in eight regions of equal length. For each of these regions the aforementioned segmentation of the HADRON acceptance is performed. The angular acceptance of HADRON is such that no cutoff by the collimator is introduced in y_{tg}.

The treatment of HADRON in this way reduces the number of trigonometric computations and significantly increases the sample generation rate.

Normalization of the cross section

The integrated luminosity $\int \mathcal{L}\, dt$ is determined by both target thickness and collected charge. As stated earlier, the target thickness is derived from the gas density, by multiplication with the nominal length of the target in the beam direction. This has two advantages: the density can be compared between different settings of the QDQ, and it allows a comparison of the density, as measured using elastic scattering from ^{3}He (section 4.5) with the one derived from the measured values for temperature and pressure (section 3.2).

The collected charge is measured using the beam-dump tank as a Faraday cup and integrating the current over time. As described elsewhere [Sta99b], this integration is affected by an offset current (I_0) and a multiplication factor (K_χ) that is duty-factor dependent. This duty-factor dependence was parametrized as

$$Q_{true} = Q\left(\frac{1}{1+p\chi}\right), \tag{4.12}$$

where the factor $p \approx 0.09$ is determined by a fit to dedicated calibration data taken with a beam of varying duty factor χ. In the present experiment, the duty factor was 80±10%. Hence, the correction factor K_χ amounts to 7.0±0.8%.

The offset I_0 was recorded during the experiment by measuring the instantaneous current in absence of an incident beam. The value of I_0 varied slightly during the experiment, from 15 nA at the start of the experiment to 40 nA at the end. However, the uncertainty on this value is rather large (±10 nA). The measured I_0 was verified using the amount of (e, e') events per measured unit charge for two different incident beam currents during the measurement of LQA. The value obtained in this way is 15±1 nA, which has been used to calibrate the I_0 measurements for the remaining kinematic settings. The slope of the current measurement was verified using a known current source; the measured deviation is less than 0.7%.

The systematic error to be associated with the current offset depends slightly on the average incident beam current, and typically amounts to 1.1%.

4.5 Determination of the target density

The thickness of the ^{3}He gas in the cell was determined by elastic scattering experiments performed in between the $(e, e'pp)$ data taking. Elastic ^{3}He(e, e') data were taken at each kinematic setting and the measured cross sections were compared to theoretical predictions. As the procedures, employed to determine the target density are the exact inverse of the methods used to determine the cross section for the $(e, e'pp)$ data, the systematic error associated with the parametrization of the QDQ solid angle, will cancel out, as the effective solid angle of the QDQ was determined using the code Q2HPHASPA. Also the contribution of K_χ will cancel out, as the duty factor during the elastic and $(e,e'pp)$ measurements was similar. The uncertainty associated with the unfolding of radiative effects in the elastic-scattering measurements is estimated to be 1%.

The cross section for elastic scattering from ^{3}He can be expressed in the plane wave Born approximation as

$$\frac{d\sigma}{d\Omega} = \left(\frac{d\sigma}{d\Omega}\right)_{Mott} \frac{1}{1+q^2/4M^2} \left[\frac{q^2}{\boldsymbol{q}^2} F_C^2(q) + \frac{\mu^2 q^2}{2m^2 Z^2}\left(\frac{1}{2}\frac{q^2}{\boldsymbol{q}^2} + \tan^2\frac{\theta}{2}\right) F_M^2(q)\right], \tag{4.13}$$

where the Mott cross section contains the usual Z^2 and recoil factors, q^2 is $-Q^2$, $\boldsymbol{q}^2$ the three-momentum squared, μ is the magnetic moment of ^{3}He, M is the ^{3}He mass and m the nucleon mass.

The charge and magnetic form factors of ^{3}He, F_C and F_M, are taken from a SOG parametrization by Amroun *et al.* [Amr94] and converted to a 15-parameter Fourier-Bessel expansion (with a cutoff radius of 6.5 fm), which is a usable parametrization for the code MEFCAL. This code was subsequently used to calculate the cross section for charge scattering. To obtain the cross section due to magnetic scattering, the code was used with the parametrization of the magnetic form factor and its result was scaled with a global factor corresponding to the central kinematic setting. The ratio of the magnetic over the charge contribution varied between 2.3 and 13.7%.

The theoretical cross section was averaged over the acceptance of the spectrometer using the code CTXS. This code segments the angular acceptance of the spectrometer in 16 small squares and calculates the cross section for each square separately. The calculated cross section was also averaged over the contributing part of y_{tg}.

Figure 4.15 shows the reconstructed target density as derived from the elastic ^{3}He(e,e') measurements. As the variations are well within the statistical uncertainty, a constant target density of 53.7±0.5 mg/cm^3 has been assumed in the analysis of the $(e,e'pp)$ data. This density is independent of the vertex position along y, as verified by analysing the same data with varying limitations on y_{tg}. A constant nominal target thickness of 268±2.4 mg/cm^2 is therefore assumed.

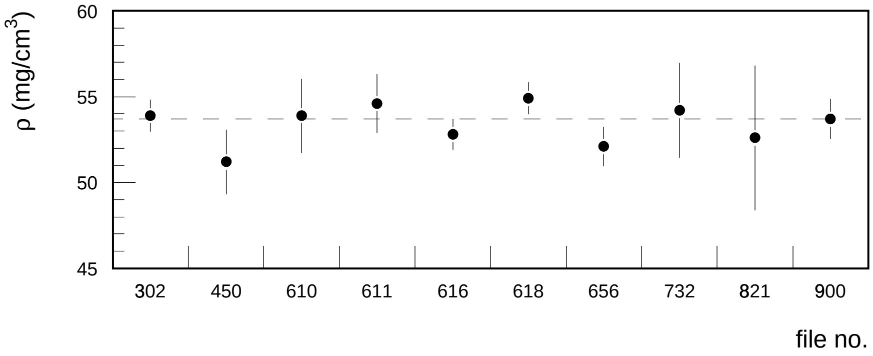

Figure 4.15: *Target gas density as determined by elastic scattering at various moments during the experiment. The dashed line indicates the average density (53.7±0.5 mg/cm^3) used in the determination of the $(e, e'pp)$ cross sections.*

The value of 53.7 mg/cm^3 is not consistent with the density as derived from the macroscopically measured temperature and pressure. These values, 15.1 K and 2.97 MPa, predict a density of 71 mg/cm^3. However, it should be noted that the temperature sensors were mounted close to the cold head and therefore do not reflect the temperature of the gas at the beam line. Assuming the pressure is correct (as it was calibrated before the start of the experiment), the reconstructed gas temperature at the interaction point is 20 K.

The effective target thickness is continuously monitored during $(e, e'pp)$ data taking by simultaneously measuring the number of (e, e') events per unit charge. This (e, e') yield is then related to measurement of the elastic scattering cross section by monitoring the prompt trigger yield in, *e.g.*, a HADRON detector. In this way, the target thickness during the measurement of an $(e, e'pp)$ kinematic configuration is linked to a neighbouring elastic (e, e') measurement. Fluctuations of the target thickness are less than 3%, as shown in Fig. 4.16.

The elastic (e, e') measurements are also used to determine the incident electron energy with high accuracy, as for elastic scattering the combined measurement of energy and angle of the scattered electron defines the kinematic configuration. The incident energy was reconstructed to be 563.7±0.3 MeV, where the

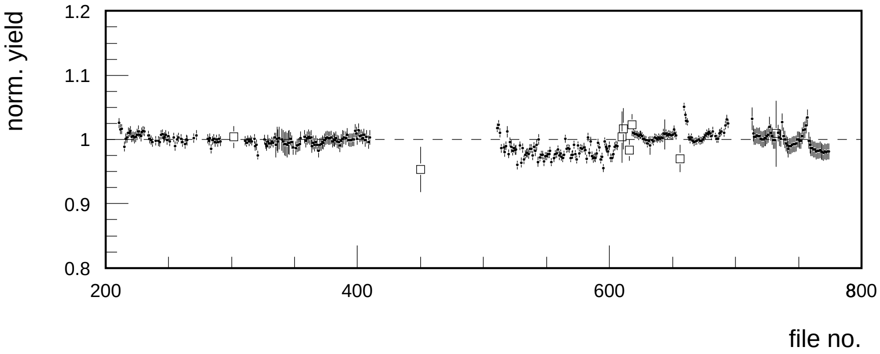

Figure 4.16: *Normalized yield of* (e, e') *events measured by the QDQ during* $(e, e'pp)$ *data taking. The* (e, e') *yield for each kinematic setting has been linked to a nearby elastic cross section measurement (the open squares) using the prompt trigger yield of the HADRON3 detector. The average of the elastic cross section measurements has been normalized to one. Deviations are less than 3%.*

uncertainty is mainly due to the momentum resolution and absolute calibration of the QDQ spectrometer.

4.6 Estimate of uncertainties

The statistical error on the cross section is determined by the uncertainty in the number of measured real events, in the estimated contribution of accidental events to the real-coincidence area A, and the uncertainty in the detection volume integration. The main contribution stems from the uncertainty on the number of real coincident events, as the number of measured accidental events is large and the corresponding weight factors f_B and f_C small. The increase of statistical uncertainty in the true yield, induced by the accidental contribution, varies from 1.15 (LQA) to 2.0 (HQ), as illustrated by Fig. 4.17. As argued in section 4.4, the contribution due to the uncertainty in the evaluation of the detection volume is less than 0.4%.

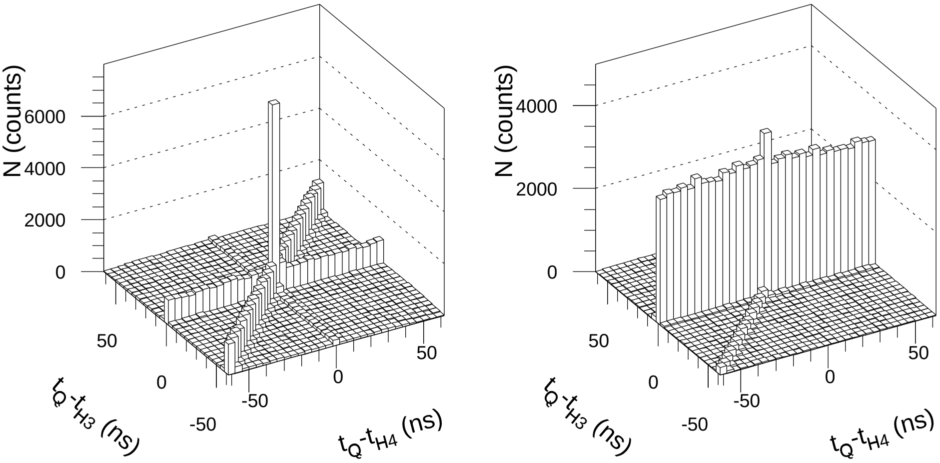

Figure 4.17: *Time difference distribution for three-fold coincident events. The left-hand panel shows the distribution for kinematics LQA, the right-hand panel for HQ.*

Besides the statistical uncertainty, a systematic uncertainty has to be associated with the measured cross section. The largest contribution stems from the estimate of the loss of protons due to interaction processes, which is estimated using a model description of the detector. The accuracy to which these are known is limited, as they are partially based on extrapolations from the GeV domain. Its contribution is estimated to be 3% per detector. Because the same code is used to estimate the interaction processes for both HADRON detectors, the uncertainties are added linearly.

The accuracy with which the target thickness is known, is determined by the error in the elastic (e, e') measurements, as most of the uncertainty associated with the duty-factor dependent current offset and the parametrization of the QDQ solid angle will cancel out. The remaining uncertainty is estimated to be 3%.

The integration of the incident electron current is hampered by a slowly varying offset and an unstable reading of this offset current. These effects induce an uncertainty of 1%.

Table 4.2: *Sources contributing to the systematic uncertainty to be associated with the measured* $^3\text{He}(e,e'pp)$ *cross sections.*

source		uncertainty
target thickness determination		3%
offset current determination		1%
HADRON detector simulation	(3%+3%)	6%
correlated track live time	(1%+1%)	2%
aerogel detection threshold		0.5%
radiative tail cutoff		1%
cell wall contributions		1.5%
integration of the detection volume		1%
total systematic uncertainty		*7.4%*

Remaining contributions are due to the correlated track live time of the HADRON detectors (two times 1%, added linearly), the requirements imposed on the aerogel signal in the analysis (0.5%), the cutoff of the radiative tail (1%), the cell wall contribution (1.5%) and the determination of the detection volume $\tilde{\mathcal{V}}$ (1%). All contributions are listed in Table 4.2; they sum up quadratically to 7.4% in total.

V Results and Discussion

Cross sections obtained in this experiment are presented and consistency among the data measured in overlapping regions of phase space is investigated. The results are compared to predictions of continuum Faddeev calculations and the implications thereof are discussed.

Differential cross sections were determined at an energy transfer ω=220 MeV for varying three-momentum transfer values q (hereafter labelled q-scan data) and at q=375 MeV/c measurements were performed over a continuous range of energy-transfer values (labelled ω-scan data). At the (ω, q) = (220 MeV, 305 MeV/c) kinematic setting measurements were performed over a large range of proton emission angles. Here, an extensive set of data with high statistical accuracy was collected to allow a detailed investigation of the dependence of the cross section on several observables.

5.1 Angular correlation in two-proton knockout

In the case of direct two-proton emission from ^{3}He, *i.e.*, a reaction that takes place on the proton pair and leaves the neutron as a spectator, the emission angles of the two protons are correlated by momentum conservation (as $\boldsymbol{p}_1' + \boldsymbol{p}_2' = \boldsymbol{q}$ at p_m=0 MeV/c). This leads to 'back-to-back' emission in the centre-of-mass frame of the virtual photon and the two protons. A larger angle of the forward proton with respect to $\boldsymbol{q}$ implies that the emission angle of the backward protons should be more forward. Therefore, such back-to-back emission is a clear signature of a direct knockout process.

This angular correlation was investigated at LQ (ω=220 MeV, q=305 MeV/c) in three different, partially overlapping, proton detector settings: LQA, LQV, and PEF (*c.f.* Table 3.2). Figure 5.1 shows a density plot of the cross section measured at LQ. The detection volume coverage extends throughout the grayed

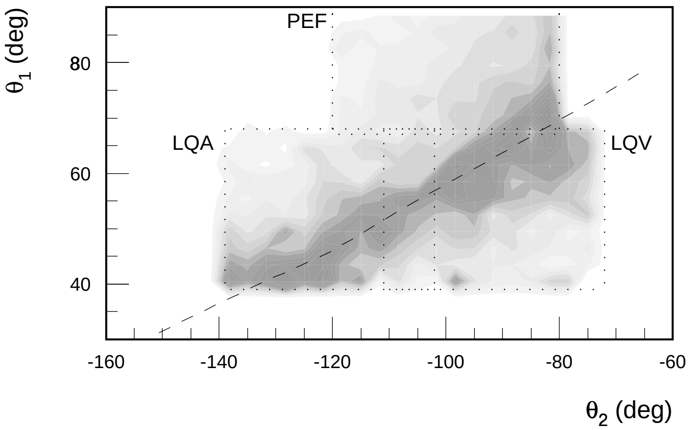

Figure 5.1: *Average experimental cross section at LQ as a function of the laboratory proton emission angles θ_1 and θ_2. The shading indicates the magnitude of the cross section, where darker shading indicates more strength (levels are not equidistant). The dashed curve indicates the angular correlation due to the back-to-back emission of the proton pair. The dotted lines indicate boundaries of the various kinematic configurations.*

area. Clearly, the larger cross sections are concentrated around the dashed curve, that corresponds to back-to-back emission of the two protons. The width of the distribution is due to the centre-of-mass motion of the neutron.

Figure 5.2 shows the differential cross section as a function of the backward proton angle for three slices in the emission angle of the forward proton. The positions of the conjugate angles, corresponding to p_m=0 MeV/c, are indicated by the arrows. The differential dV is $d\Omega_{e'} dE' d\Omega_1 d\Omega_2 dT_1$; the error bars indicate statistical uncertainties only. The overall systematic error is not indicated in the graphs and amounts to 7.4%.

Consistency checks

The data taken at q=305 MeV/c are composed of three angular settings of the HADRON detectors. This opens the possibility to verify the methods used to

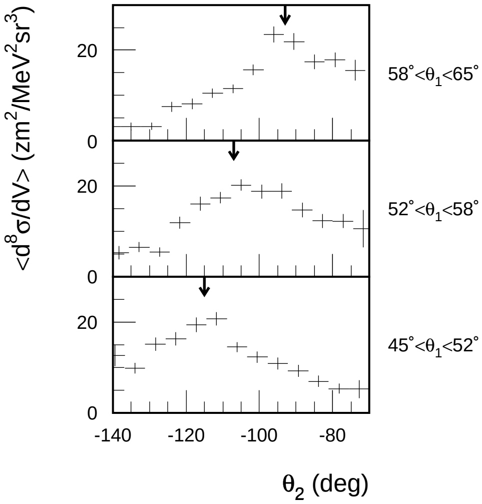

Figure 5.2: *Angular distribution of the average cross section at LQ as function of the angle of the backward proton, for three slices in the forward proton angle. The positions of the conjugate angles (see text) are indicated with arrows.*

extract cross sections from the data, by comparing the cross sections derived from different detector settings for the same region of phase space. These overlapping regions in the detection volume coverage can be identified from Fig. 5.1. The domain $40 < \theta_1 < 68°$ was covered both in LQA and LQV. The cross sections for these two settings are displayed individually in Fig. 5.3 as a function of θ_2; in the overlap region from $-111 < \theta_2 < -102°$ the ratio of the cross sections is 0.98 ± 0.05. For the adjacent settings LQV and PEF the θ_1 distribution is shown in Fig. 5.3 for the domain $-110 < \theta_2 < -95$ °; the cross section distribution around the separation at $\theta_1 = 70°$ is continuous.

5.2 Neutron momentum distribution

For the data measured at LQ, the differential cross section is shown as a function of p_m in Fig. 5.4, averaged over the detection volume corresponding to the settings LQA and LQV, *i.e.*, $40 < \theta_1 < 68°$. The cross section decreases

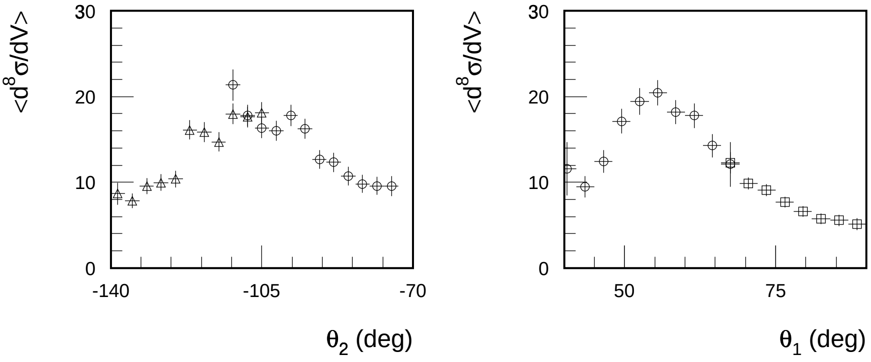

Figure 5.3: *Average cross section as a function of proton emission angles. In the left-hand panel, cross sections derived from LQA (triangles) and LQV (circles) are compared. In the right-hand panel the adjacent data sets LQV (circles) and PEF (squares) are shown. The range in the non-explicit proton angle was limited to the overlapping domain.*

roughly exponentially as a function of the neutron momentum between zero and 300 MeV/c. This reflects the neutron momentum distribution inside ^{3}He for relative momenta in the pp pair around 300 MeV/c, the region probed in this kinematic configuration (*c.f.* Fig. 2.5 and Fig. 4.14).

Signatures of two-proton knockout by one-body hadronic currents will most likely be found at low p_m – where the neutron is left approximately at rest and can be considered a spectator – since in direct pp knockout contributions from two-body currents are suppressed. Contributions from MECs are to first relativistic order prohibited as the photon will not couple to the neutral mesons exchanged in the pp pair. Additionally, the knockout via $pp \rightarrow \Delta^+ p \rightarrow pp$ is suppressed since the otherwise dominant M1 transition is forbidden by angular momentum and parity conservation rules for protons initially in a $^1S_0$ state [Wilh96].

A comparison of the data at $p_m \lesssim 100$ MeV/c with the results of continuum Faddeev calculations including only one-body currents shows a fair agreement; it accounts for approximately 50 to 80% of the measured strength in this domain, while the contribution of MECs is small (5%).

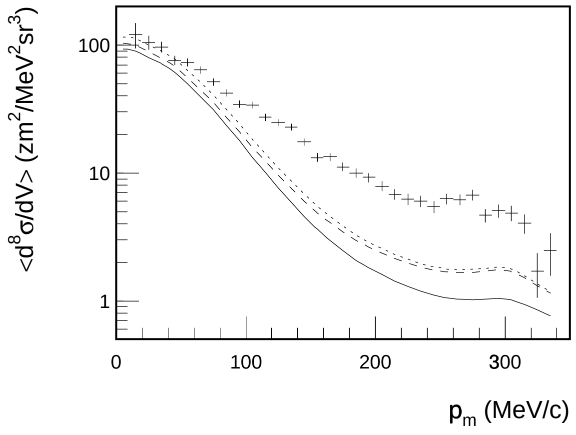

Figure 5.4: *Average cross section as a function of p_m for the combined kinematic settings LQA and LQV. The curves represent the results of continuum Faddeev calculations (solid: one-body currents only, dashed: including MECs, dotted: including MECs and static Δ currents).*

Processes at high neutron momentum

At higher missing-momentum values, one-body calculations underestimate the data by a factor of five. The high missing-momentum region is likely dominated by two-body hadronic currents (MECs and ICs), which involve coupling of the virtual photon to a proton-neutron pair. Such processes will predominantly contribute to the high p_m region in the $^3\text{He}(e, e'pp)$ reaction as the momentum of the photon is shared by both nucleons involved. This expectation is supported by the results of calculations with MEC contributions, that show an increased importance of MECs of up to 40% of the calculated strength at $p_m \approx 300$ MeV/c, as compared to the low p_m region.

In the high p_m domain, also a sizeable contribution from Δ excitation can be expected. Excitation of a Δ within a pn pair, a process that is not suppressed by selection rules like in the pp case, will contribute primarily to this domain.

Moreover, excitation of the Δ resonance strongly depends on the invariant mass of the photon plus two-nucleon system. If one considers a direct reaction on

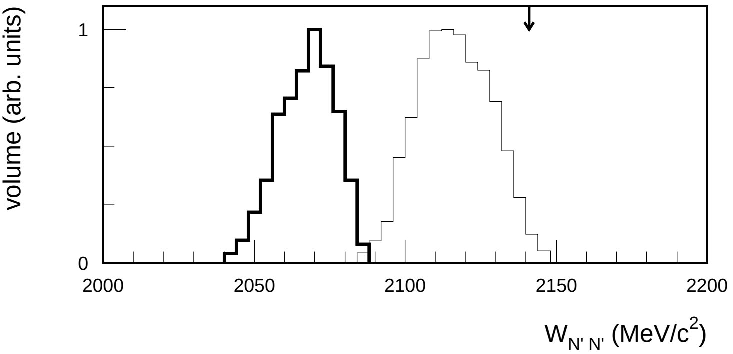

Figure 5.5: *Invariant mass of the two nucleons in the final state for the* $p_1'p_2'$ *pair (thick line) and the* $p_1'n$ *pair (thin line) in kinematics LQ. The arrow indicates the position of the resonant peak in real-photon induced deuteron breakup [Wilh96].*

a two-proton pair, *i.e.*, at small p_m values, the invariant mass $W_{\gamma pp}$ in the initial state can be identified with the final-state observable $W_{p_1'p_2'}$. At LQ this invariant mass ranges from 2050 to 2080 MeV/c^2, which is well below the mass of the (free) ΔN system. If one assumes excitation of a pn pair, the relevant invariant energy is that of the photon plus proton-neutron system. This is reflected in the final-state quantity $W_{p_1'n'}$, which ranges from $2100 \lesssim W_{p_1'n'} \lesssim 2140$ MeV/c^2 for p_m values around 300 MeV/c (see Fig. 5.5). The invariant mass of the other pn pair, *i.e.*, $W_{p_2'n'}$, is similar to that of the pp pair for this p_m region. Therefore the cross section for intermediate Δ excitation of the p_1n pair will be dominant, since its invariant mass is closest to that of the $N\Delta$ system.

Calculations of the ^{16}O(γ, pn) cross section indicate a strong dependence of the contribution of isobar currents on the photon energy, as is shown in Fig. 5.6 [Mac93]. These calculations, as well as calculations of photon-induced deuteron breakup, which use a different Δ propagator [Wilb96], indicate a maximum in the cross section due to Δ excitation around $E_\gamma \sim 250$ MeV. The equivalent invariant mass $W_{p_1'n'}$ will therefore be around 2125 MeV/c^2.

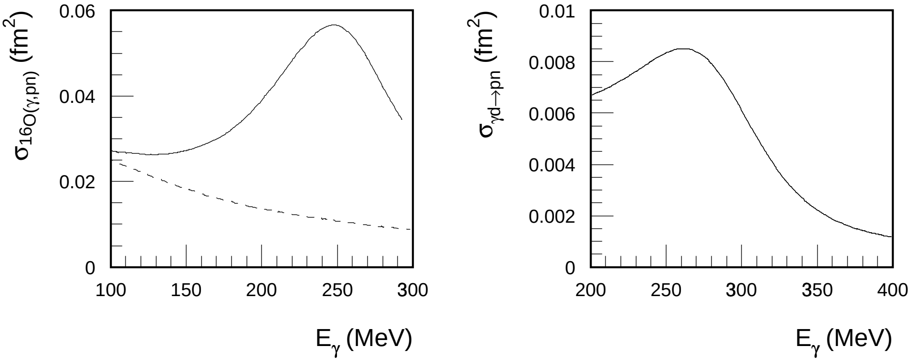

Figure 5.6: *Cross section for* ^{16}O(γ, pn) *(left panel) due to MECs (dashed line) and MECs plus ICs currents (solid line) as a function of photon energy [Mac93]. The right-hand panel shows the total cross section for deuteron photodisintegration as a function of the photon energy, as calculated by Wilbois et al. [Wilb96].*

Faddeev calculations including isobar currents

Within the continuum Faddeev framework described in section 2.3, excitation of the Δ in an intermediate state was implemented within the so-called ‘static’ approximation. The cross sections calculated within this approximation are shown as the dotted line in Fig. 5.4: it leads to a limited (at most 5%) enhancement of the cross section, largely independent of p_m. This behaviour is not unexpected, as it has been shown that in the ^{16}O(γ, pn) reaction above $E_\gamma \approx 100$ MeV [Mac93] as well as in the exclusive deuteron electro-disintegration at high momentum [Blo98], the static approach results in significantly lower cross sections compared to calculations that include a realistic (resonant) Δ propagator (see Fig. 5.7).

As of yet, no continuum Faddeev calculation is feasible that includes a realistic isobar current. The present calculations are performed in a basis built on the Jacobi momenta only in which the excitation of a Δ, requiring knowledge of the individual momenta of the nucleons, cannot be readily incorporated. This hampers a quantitative interpretation of the high p_m data obtained in this experiment.

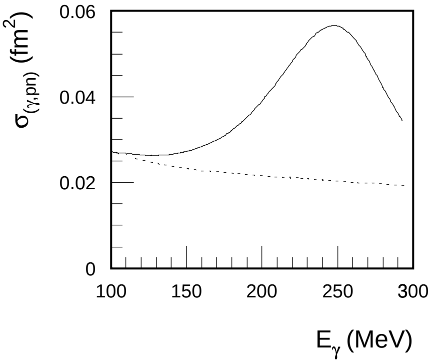

Figure 5.7: *The ^{16}O(γ, pn) cross section for a calculation performed with a 'static' Δ (dotted line) and a calculation with a realistic Δ propagator (solid line) [Mac93].*

FSI configurations at LQ

In Fig. 5.8, the missing-momentum distributions obtained at the LQ kinematic setting are displayed for three slices in γ_1. For a fixed value of p_m the angle γ_1 implicitly fixes the kinematics of the final state, provided the direction of $\boldsymbol{p}_2'$ is kept within a limited range. For $\gamma_1 \lesssim 25°$ and $\gamma_1 \gtrsim 35°$, the three nucleons are always emitted with a sizeable momentum difference, which reduces their mutual interaction. Within the interval $25 < \gamma_1 < 35°$, a so-called 'FSI configuration' occurs. Such a configuration is characterized by two nucleons being emitted with (vectorially) similar momenta. Enhanced probability for rescattering exists between such nucleons, which may significantly influence the cross section in such domains.

In the case of LQ around 300 MeV/c, such a configuration occurs for the forward proton and the undetected neutron. Within the interval $25 < \gamma_1 < 35°$ momentum difference values p_{13} as low as 90 MeV/c are covered. This may be the origin of the 'bump' observed in the cross section around $220 \lesssim p_m \lesssim 300$ MeV/c. A similar structure is seen in the theoretical predictions, which show an enhancement of the calculated cross section with respect to the extrapolation of the exponential decay for $p_m < 200$ MeV/c.

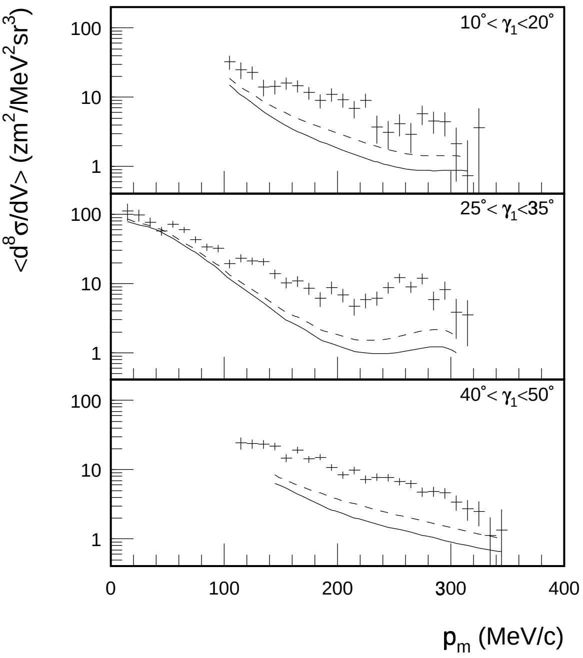

Figure 5.8: *Average cross section as a function of p_m for three slices in the forward proton angle γ_1. The solid and dashed curves represent the results of calculations with a one-body current operator and including MECs, respectively. The data were averaged over a γ_2 range from −114° to −142°.*

5.3 FSI configurations in various kinematics

For kinematic domains in which two nucleons are emitted with similar momentum vectors, rescattering effects are an important factor that influence the cross section. Presentation of the data as a function of the momentum difference p_{ij} allows an investigation focussed on these rescattering effects.

In the HQ kinematic setting the detection volume extends to $p_{13} = 0$ MeV/c. As the cross section depends strongly on both p_{13} and p_m individually and the detection volume covered is non-rectangular in these two observables, the p_m range has to be limited to $360 < p_m < 380$ MeV/c for a proper presentation.

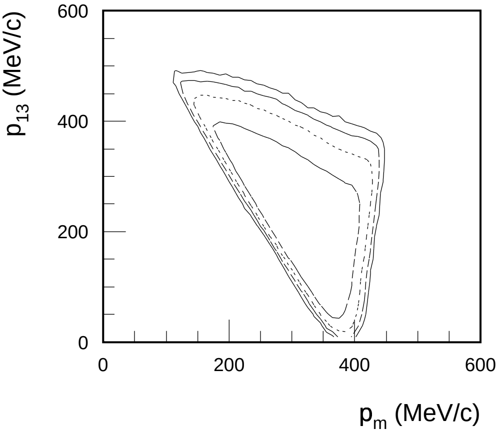

Figure 5.9: *Projection of the detection volume on the* (p_{13}, p_m) *plane for kinematics HQ. For detection volume coverage over the entire range* $0 < p_{13} < 320$ *MeV/c, the acceptance in* p_m *should be limited to* $360 < p_m < 380$ *MeV/c.*

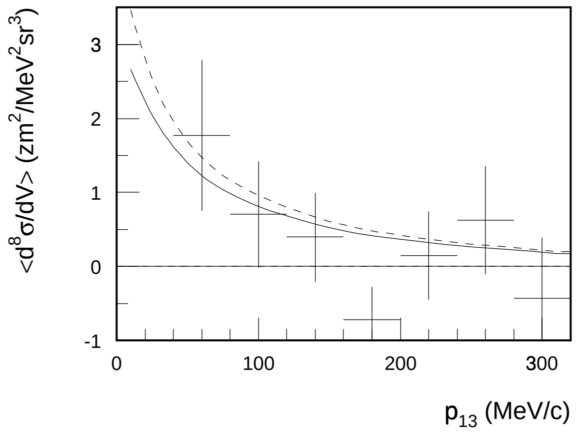

Figure 5.10: *Average cross section as a function of the momentum difference between the forward proton and the neutron for the HQ kinematic setting, for* $360 < p_m < 380$ *MeV/c. The solid curve represents a calculation performed with a one-body current operator, the dashed curve includes also MEC contributions.*

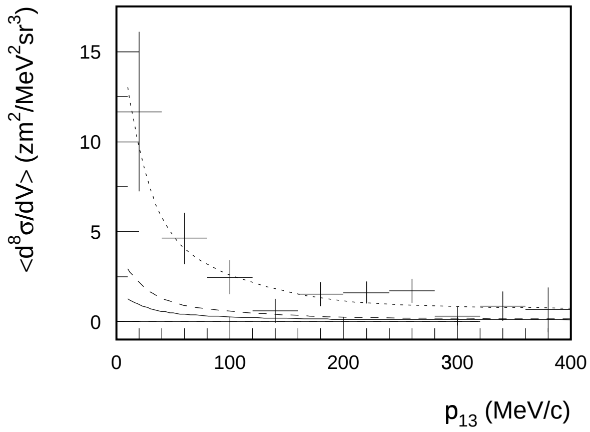

Figure 5.11: *Average cross section for the 'FSI configuration' at HW. The* p_m *acceptance has been limited to 360* $<$ p_m $<$ *410 MeV/c. The curves are results of the Faddeev calculations with a one-body current operator (solid), including MECs (dashed) and a renormalized MEC result (dotted,* $\times 4.43$*).*

The shape of the detection volume is shown in Fig. 5.9. Figure 5.10 shows the average cross section for HQ for the 'FSI configuration'.

The enhancement of the cross section for $p_{13} \to 0$ MeV/c is well reproduced by the result of continuum Faddeev calculations. The statistical accuracy of the data for this p_m domain is limited, but the compatibility between the theoretical curves and the data indicates that the process of final-state rescattering is well described.

Similar configurations occur at other kinematic settings. Especially HW contains a fairly broad region in p_m – between 360 and 410 MeV/c – for which complete detection volume coverage exists at $p_{13} = 0$ MeV/c. Unfortunately, the high value of energy transfer together with the high p_m region means that a sizeable part of the reaction occurs via intermediate Δ excitation in the pn pair. The calculated cross section, including MECs, globally underestimates the data by a factor of 4.4 at $360 < p_m < 410$ MeV/c (and by a factor of 9.1 with respect to a one-body calculation) as can be seen from Fig. 5.11.

Although the absolute magnitude is not correctly predicted, the dependence of the cross section on p_{13} is well reproduced by both the one-body calculations and those including MECs. The similarity in shape between both types of calculations suggests that the shape is mainly due to NN rescattering and the absolute magnitude to the current operators used. A scaling of the calculated results, including MECs, by a factor of 4.43 results in a good agreement between data and calculations over the entire p_{13} domain. Hence, although the calculations underestimate the 'feed' into the 'FSI configuration', rescattering is correctly described by the continuum Faddeev calculations.

5.4 Varying the virtual photon characteristics

Information on the reaction mechanism and the interaction of the virtual photon with the tri-nucleon system can be obtained by varying the characteristics of the electromagnetic probe, *i.e.*, the energy transfer ω and the momentum transfer q. The data at the various (ω, q) points all show a similar dependence of the cross section on the missing momentum. This suggests an analysis of the data as a function of ω and q for slices in this final-state neutron momentum. However, also strong rescattering effects can occur at specific values of p_m, due to $p_{13} \rightarrow 0$ MeV/c, the exact position of which depends on the experimental detection volume. Therefore, no reliable comparison can be made between data for different (ω, q) settings for the p_m domain in which an 'FSI configuration' occurs. For the q-scan data, this limits the usable domain to $p_m \lesssim 220$ MeV/c, while for the ω-scan data the domain $p_m \gtrsim 300$ MeV/c should be disregarded.

Results at varying momentum transfer

In Fig. 5.12 the cross section is shown as a function of q for two slices in p_m. The data at missing-momentum values below 100 MeV/c show a decrease by a factor of four between q=305 MeV/c and q=375 MeV/c. Both this slope and the absolute magnitude of the cross sections are reasonably well described by the calculations. For both values of the momentum transfer a calculation with only one-body hadronic currents explains 72±13% of the measured strength. As expected, the inclusion of MEC contributions has only a minor effect and

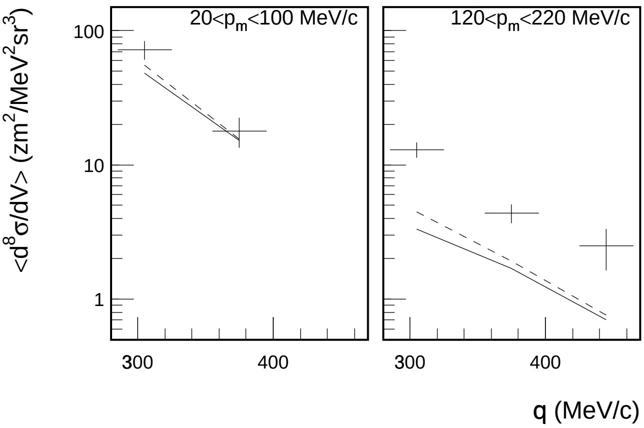

Figure 5.12: *Average cross section dependence on the momentum transfer* q*, for two slices in the final-state neutron momentum. The solid curves account for one-body contributions only, the dashed curves also include MECs. Data were averaged over the domain 10* $< \gamma_1 <$ *25°. Width of error bars indicates the range in* q *values covered due to the acceptance of the spectrometer. The domain* $p_m < 120$ *MeV/c is not covered by the detection volume of HQ.*

increases the calculated strength to 80% of the experimentally observed value. The fair agreement between data and theory for both momentum transfer values indicates that, in the p_m domain below 100 MeV/c, the cross section is predominantly driven by a one-body reaction mechanism.

In the p_m domain $120 < p_m < 220$ MeV/c, the difference between a one-body calculation and data is about a factor of five. Inclusion of MECs in the calculation increases the calculated cross section by 10 to 35%, depending on the momentum transfer, thus reducing the discrepancy to about a factor of four. The slope of data and calculations is nevertheless reasonably similar.

Results at varying energy transfer

Two-body currents, especially those involving the intermediate excitation of the Δ resonance, show a significant dependence on the invariant mass of the initial

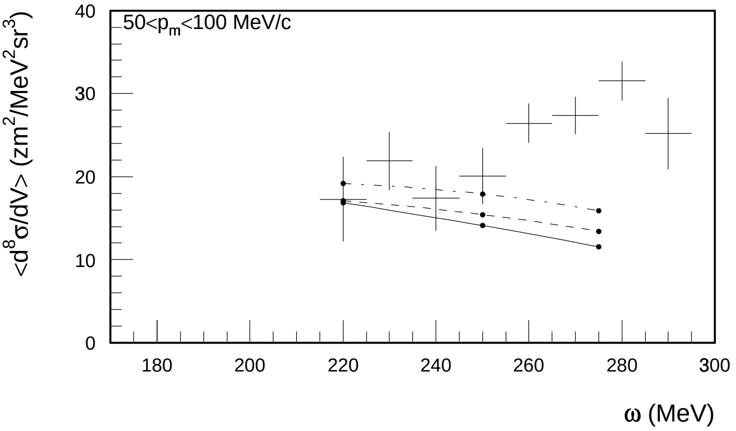

Figure 5.13: *Average cross section as a function of the energy transfer ω at q=375 MeV/c and $50 < p_m < 100$ MeV/c. The curves represent calculations with a one-body current only (solid), including MECs (dashed) and including MECs and 'static' ICs (dot-dashed).*

two-nucleon plus photon system [Mac93, Wilh96]. By varying the energy transfer of the reaction the role of isobar currents can be investigated. Therefore, measurements were performed for $170 < \omega < 290$ MeV at a momentum-transfer value of q=375 MeV/c (LW, CQW, IW, and HW).

As argued in section 5.2, the low p_m region is most likely due to direct two-proton knockout, as in this domain the neutron is left 'at rest'. In case of such a direct reaction mechanism, the invariant mass of the two emitted protons $W_{p_1'p_2'}$ can be identified with the invariant mass of the γpp system. For the ω region covered for $p_m < 100$ MeV/c, this invariant mass ranges from 2055 MeV/c^2 at $\omega = 220$ MeV (more than one full width below the peak of the Δ resonance) to 2120 MeV/c^2 at $\omega = 290$ MeV, *i.e.*, almost on top of the resonance.

In Fig. 5.13 the data for the p_m domain from 50 to 100 MeV/c at q=375 MeV/c are shown. As expected from the measurements at LQ, the agreement between data and calculations for ω=220 MeV is quite good. This already holds for a calculation with only one-body currents, which can be seen as additional evidence for the dominance of one-body currents in this p_m and ω domain.

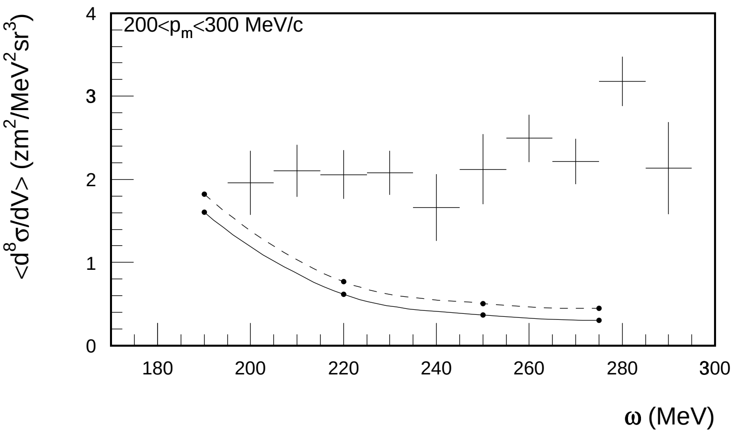

Figure 5.14: *Average cross section as a function of the energy transfer* ω *at* q*=375 MeV/c and 200* $< p_m <$ *300 MeV/c. The curves represent calculations with a one-body current only (solid), including MECs (dashed).*

The calculations with a one-body current operator show a slightly decreasing trend as a function of ω, which is due to a changing value of the relative momentum within the *pp* pair; whereas at ω=220 MeV the central value for the relative momentum is 290 MeV/c per nucleon, it has risen to 360 MeV/c per nucleon at ω=275 MeV.

The inclusion of MECs in the calculation hardly changes the cross section at ω=220 MeV and addition of a 'static' Δ contribution changes the result by about 15%. At higher energy transfer values, the data show an increase of almost 50% over the ω range from 220 to 280 MeV. The contribution due to MECs remains rather low (below 15%). Therefore, the increase of the data probably reflects an increasing importance of intermediate Δ excitation at higher invariant masses $W_{p'_1 p'_2}$. As expected, calculations including a static approximation of the Δ current fail to reproduce this enhancement and severely underestimate the data for $\omega \gtrsim 250$ MeV.

For higher values of the missing momentum, as shown in Fig. 5.14, the measured cross section does not show any structure as a function of ω. The theoretical cross section calculated with a one-body current operator decreases for increasing values of ω, due to the increasing relative momentum of the protons in the *pp* pair. In addition, at $\omega \approx 200$ MeV, the kinematic configuration is close to an 'FSI configuration' occuring within the experimental detection volume at $p_m = 320$ MeV/c. At this low ω value, the ratio of data to theory is 1.6±0.3, whereas at higher values of the energy transfer the data overshoot theory by about a factor of ten.

In the missing momentum domain probed here, a considerable part of the strength will be due to coupling of the virtual photon to a *pn* pair, of which the invariant mass in the final state is considerably larger than in the γpp system: $2110 < W_{p'_1 n'} < 2190$ MeV/c^2 for $250 < p_m < 300$ MeV/c. This domain corresponds to the region where the total cross section for photon-induced deuteron breakup reaches its maximum, *i.e.*, at $E_\gamma \approx 265$ MeV [Wilh96]. This corresponds to an invariant mass of the γpn system of approximately 2140 MeV/c^2. In this energy range, the photo-induced breakup of the deuteron is known to be dominated by intermediate Δ excitation and its subsequent decay.

5.5 Signatures of the initial state

An investigation of the data at low missing momentum, *i.e.*, $p_m \lesssim 100$ MeV/c, and at an energy transfer value of ω=220 MeV, showed a dominant contribution from direct two-proton knockout by a one-body hadronic current. As argued in section 2.3, breakup induced by coupling to a one-body current in principle allows investigation of the ^{3}He bound-state wave function. Calculations indicate that the cross section is almost exclusively determined by coupling to the forward proton, and initial-state proton momentum p_1. Investigation of the cross section as a function of $p_{\mathit{diff},1}$ in the low p_m domain at LQ may thus lead to insight in the initial-state wave function.

In Fig. 2.5, probabilities associated with the ^{3}He wave function were shown for various NN potentials. Within the experimentally accessible domain, the shape of the wave functions is similar for Bonn-B, CD-Bonn and Nijmegen-93. The result for Argonne v_{18} is different especially in the high p_{cm} and high p_{rel} region, but as in this domain the ^{3}He$(e, e'pp)$ cross section is not primarily driven by one-body currents no quantitative comparison with data can be made. Small

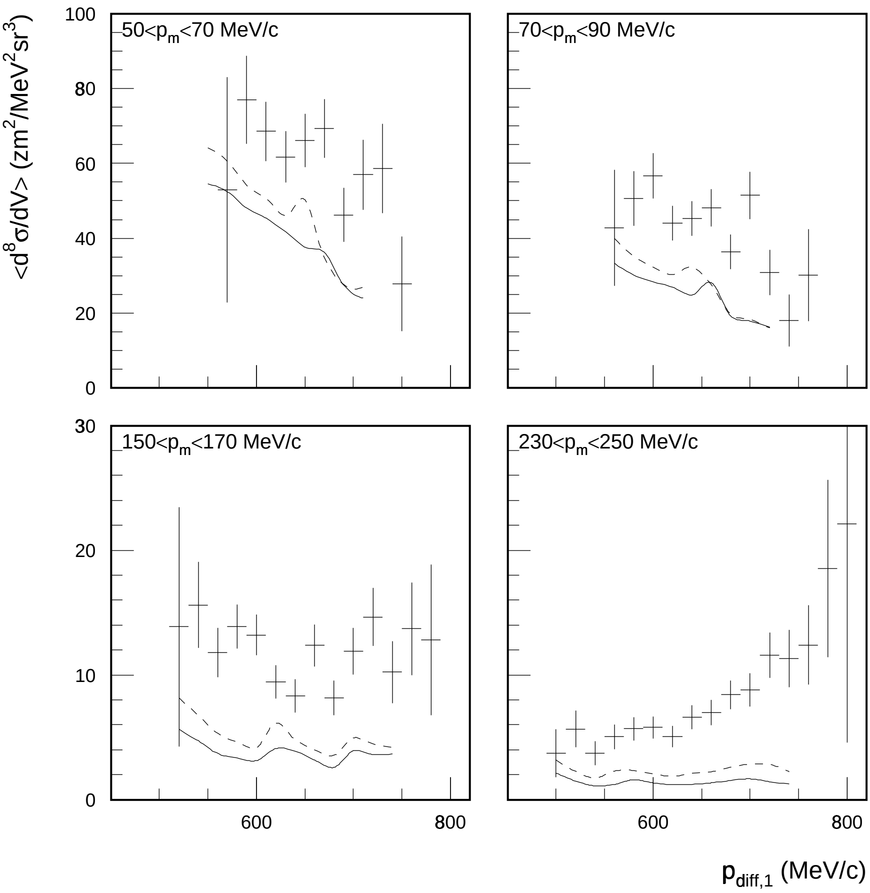

Figure 5.15: *Average cross section as a function of* $p_{diff,1}$ *for several slices in* p_m *of 20 MeV/c wide. Data are taken from the combined kinematic settings LQA, LQV and PEF. Solid curves are based on one-body currents only; dashed curves include MECs, both calculated using the Bonn-B potential. The wiggles in the calculated cross section are due to small variations in the parts of the detection volume that contribute in the different kinematic configurations.*

differences in magnitude, however, exist between the various model predictions for low p_m and here too the difference is largest for Argonne v_{18}. For all potentials one expects, based on the slope of the probability density as a function of p_{rel}, a decrease of the experimental cross section due to one-body currents as a function of $p_{\mathit{diff},1}$ at low p_m, with the slope becoming increasingly more flat at higher missing momenta.

The rapid changes in cross section as a function of p_m make it necessary to investigate the $p_{\mathit{diff},1}$ dependence for slices in the missing momentum, that are not wider than 20 MeV/c. In Fig. 5.15 the $p_{\mathit{diff},1}$ dependence in shown for various slices of the missing momentum. The two top-graphs are adjacent slices in p_m (from 50–70 and from 70–90 MeV/c) and these already show a different slope. The fine binning thus required leads to a reduced statistical accuracy for the measured cross sections.

For the domain $p_m \lesssim 100$ MeV/c the shape of the data is fairly well reproduced by calculations performed with the Bonn-B potential. The measured slope for the region $50 < p_m < 70$ MeV/c, -0.13 ± 0.07 $(\mathrm{zm}^2/\mathrm{MeV}^2\mathrm{sr}^3) / (\mathrm{MeV}/c)$, is not unlike the slope calculated including contributions due to MECs, namely -0.21 $(\mathrm{zm}^2/\mathrm{MeV}^2\mathrm{sr}^3) / (\mathrm{MeV}/c)$.

At p_m values between approximately 100 and 200 MeV/c no clear structure can be observed, neither in the data nor in the calculations. However, above $p_m \approx 200$ MeV/c the data show a significant increase as a function of $p_{\mathit{diff},1}$, which is not predicted by calculations. The p_m domain shown in the bottom-right panel of Fig. 5.15 is representative for the general trend above 200 MeV/c, *i.e.*, an increase by almost a factor of five between $p_{\mathit{diff},1}$=600 and 800 MeV/c.

Investigation of the kinematic relations between $p_{\mathit{diff},1}$ and other relevant observables for this p_m domain showed no correlation between $p_{\mathit{diff},1}$ and p_{13}. It is therefore unlikely that the effect is induced by final-state rescattering. However, there is, for a fixed value of p_m, a strong correlation between $p_{\mathit{diff},1}$ and the angle γ_1, as shown in Fig. 5.16.

The excitation of the Δ resonance in a pn intermediate state is expected to cause, due to its multipole character, a characteristic angular dependence of the cross section. Calculations of the coherent π^0 photoproduction cross section within the Δ-hole model [Koc83], which is dominated by the M1 multipole, show a peak around $\gamma_1^{cm} = 90°$ in the proton-plus-photon centre-of-mass sys-

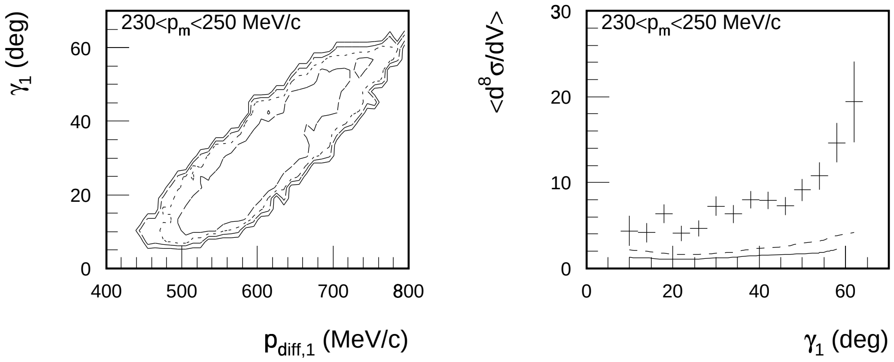

Figure 5.16: *Detection volume covered (left) by the settings LQA, LQV and PEF for the domain 230 < p_m < 250 MeV/c. In the right-hand panel the cross section is displayed as a function of γ_1 for the selected p_m interval.*

tem. Another characteristic angular dependence was found in calculations of the ^{16}O(γ, pn) cross section at $E_\gamma = 281$ MeV, a reaction that is also dominated by the Δ current [Ryc94]. The position of the resonance in this reaction varies between approximately γ_1=40° and 100°, depending on the proton energy T_1. It is therefore not unlikely that the angular dependence seen in Fig. 5.16 is induced by intermediate Δ excitation.

Comparing potential models

Figure 5.17 shows the data as a function of $p_{diff,1}$ for the same set of p_m intervals as used in Fig 5.15. Predictions based on continuum Faddeev calculations performed with different NN potential models are indicated. For the low p_m region, differences in both magnitude and slope are observed, with the Argonne v_{18} prediction being up to 15% lower than the one based on Bonn-B. In Table 5.1 the slope of the data is compared to calculations performed with a one-body current and various potential models. For the Bonn-B potential, results of calculations that include MECs are also listed.

The variations in slope between the various models are around 0.03 to 0.04. This effect is of the same order of magnitude as the effects of MECs, which was

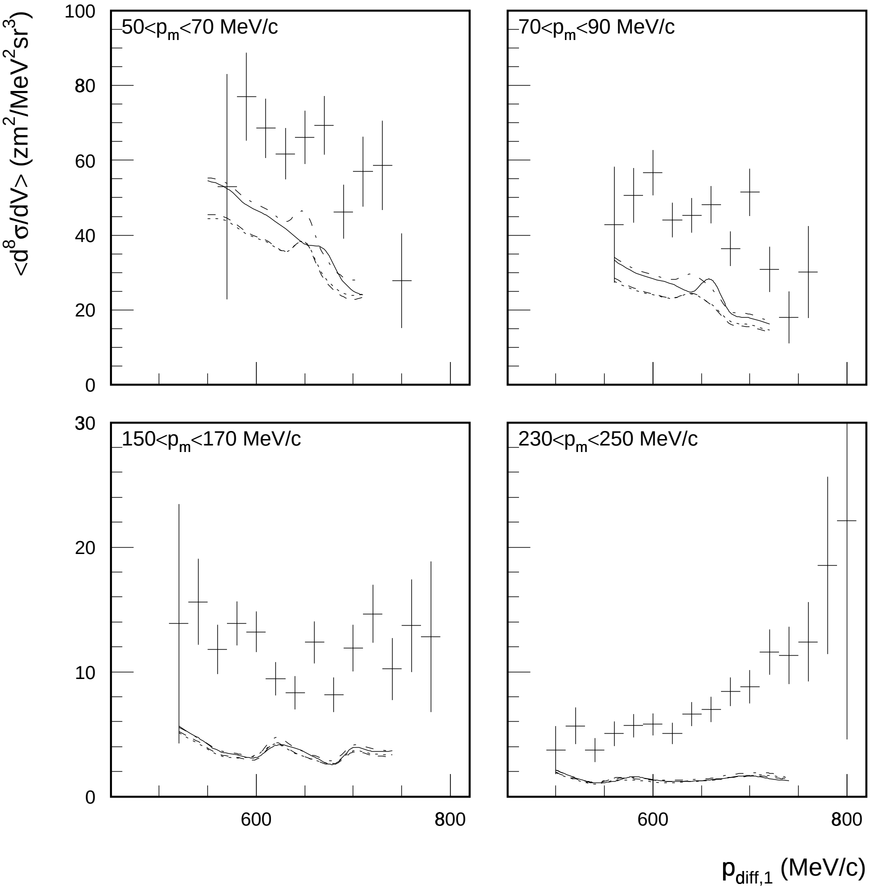

Figure 5.17: *Average cross section as a function of* $p_{diff,1}$ *as in Fig. 5.15. Data are compared to various potential models. Solid curve: Bonn-B, dotted: Argonne* v_{18}*, dashed: CD-Bonn, dot-dashed: Nijmegen-93.*

Table 5.1: *Slope of the average measured cross section as a function of* $p_{diff,1}$, *for two* p_m *intervals indicated in Fig. 5.15 and Fig. 5.17. The unit of slope is* $(zm^2/MeV^2 sr^3)\,/\,(MeV/c)$.

	$50 < p_m < 70$ MeV/c		$70 < p_m < 90$ MeV/c	
Bonn-B (one-body)	−0.21		−0.11	
Argonne v_{18} (one-body)	−0.14		−0.08	
Nijmegen-93 (one-body)	−0.18		−0.11	
CD-Bonn (one-body)	−0.15		−0.09	
Bonn-B (one-body +MECs)	−0.24		−0.15	
Data	−0.13	±0.07	−0.11	±0.05

only calculated using the Bonn-B potential. The influence of intermediate Δ excitation on the calculated slope is as of yet unknown; also the underestimation of the data by all four calculations, which amounts to approximately 30% at $50 < p_m < 70$ MeV/c, is still not explained quantitatively. In view of these uncertainties, the low p_m data do not yet allow to express a preference for any of the potential models considered.

In the high missing-momentum region, the differences due to the NN potential are almost negligible within the experimentally probed domain. The large discrepancy between data and calculations and the unknown contribution of isobar currents hampers a quantitative comparison. Either an experimental means to isolate the isobar contribution, *e.g.*, a separation of the cross section in its structure functions, or perhaps a calculation including comprehensive treatment of Δ excitation should provide the necessary information to draw conclusions from this domain in the response.

Summary

The two-nucleon part of the strong interaction, the nucleon-nucleon (NN) force, provides the dominant part of the binding among nucleons inside a nucleus. The interaction features an attractive long-range part (at distances larger than approximately 1 fm) and a strongly repulsive part at shorter inter-nucleon distances. The interaction induces correlations among the nucleons bound in nuclei. Recently, various theoretical models of the NN interaction have been proposed describing accurately the binding energy of the deuteron and the NN scattering data. However, these models give different results for both ground-state and breakup properties of three-nucleon systems.

Study of the $^3\mathrm{He}(e, e'pp)$ reaction provides a tool to investigate the reaction mechanism of the two-nucleon knockout reaction and to test predictions based on bound-state wave-functions calculated with different potential models. Exact calculations of the exclusive breakup cross section show that domains in phase space exist where the reaction is primarily driven by one-body hadronic currents. The cross section in these domains is dominated by coupling of the virtual photon to the proton emitted with a small angle with respect to the momentum transfer. This opens the possibility that measurements of the $^3\mathrm{He}(e, e'pp)$ cross section in these domains may give information on the initial-state wave function. However, breakup can also be induced by coupling of the virtual photons to mesons (meson-exchange currents or MECs) or via excitation of the Δ resonance in an intermediate state (isobar currents). Although their contribution to the reaction cross section is suppressed in the case of direct two-proton knockout, they are expected to play an important role at higher values of the neutron momentum in the final state. Variation of the virtual-photon characteristics, especially the energy transfer to the system, provides an experimental way to investigate their importance.

The $^3\mathrm{He}(e, e'pp)$ reaction can thus be used to investigate the effects of nucleon-nucleon correlations and currents in $^3\mathrm{He}$. This work describes such an exclusive

^{3}He$(e, e'pp)$ experiment and a comparison of the results with continuum Faddeev calculations performed with various models of the NN interaction.

The experiment was carried out with the high duty-cycle electron beam extracted from the Amsterdam Pulse Stretcher facility AmPS; the incident electron energy was 564 MeV and the beam current amounted to 0.5–1.5 μA. A cryogenic, high-pressure ^{3}He gas target was used with a thickness of 270 mg/cm^2. Scattered electrons were detected in the high-resolution QDQ magnetic spectrometer, the two emitted protons in the large-solid-angle scintillator arrays HADRON3 and HADRON4. Cross sections were determined for three values of the three-momentum transfer of the virtual photon (q=305, 375, and 445 MeV/c) at an energy transfer value ω of 220 MeV. At q=375 MeV/c, measurements were performed over a continuous range in energy transfer from 170 to 290 MeV.

The data are compared to results of continuum Faddeev calculations performed by Golak *et al.*, that account for the contributions of rescattering among the emitted nucleons. These calculations include both one-body hadronic currents as well as contributions due to the coupling to π and ρ mesons in an intermediate state. Since at present no framework exists to solve the three-body problem in a Lorentz-covariant manner, all parts of the calculation were performed in a non-relativistic fashion to maintain internal consistency. Various potential models were used in the calculations: Bonn-B, charge-dependent (CD) Bonn, Nijmegen-93 and Argonne v_{18}.

The angular dependence of the ^{3}He$(e, e'pp)$ cross section shows a strong back-to-back correlation, which is a signature of a direct two-proton emission mechanism that leaves the neutron with a low momentum in the final state; the width of the angular distribution reflects the momentum distribution of the neutron. Presentation of the data as a function of the missing or neutron momentum, p_m, shows that the cross section decreases exponentially as a function of p_m.

In the missing-momentum region below approximately 100 MeV/c, and at energy transfer values well below the Δ resonance, the ^{3}He$(e, e'pp)$ reaction is likely dominated by direct knockout of correlated proton pairs, as the contributions from MECs and intermediate Δ excitation are suppressed. Calculations performed with only a one-body hadronic current operator show a fair agreement with the data obtained at $p_m \lesssim 100$ MeV/c at $\omega = 220$ MeV and q=305 MeV/c. Measurements performed at q=375 MeV/c show similar results. The inclusion of

MECs in the current operator only has minor effect on the calculated strength. It can therefore be concluded that at ω=220 MeV and $p_m < 100$ MeV/c the cross section is dominated by direct knockout of two protons via a one-body hadronic current. At higher p_m values, from 120 to 320 MeV/c, a discrepancy of about a factor of five is observed between the data and calculations with a one-body current operator only. Contributions due to MECs increase the calculated strength by up to 35% only.

The influence of intermediate Δ excitation depends on the invariant mass of the nucleon pair plus the photon. To investigate these isobar currents, measurements were performed in the domain ω=170–290 MeV. This range corresponds for $p_m < 100$ MeV/c to invariant masses $W_{p'_1 p'_2}$ between 2055 and 2120 MeV/c^2. An increase of the measured cross section by almost 50% is seen over this range in energy transfer, presumably reflecting the increased importance of the Δ resonance. Theoretical predictions including MECs and isobar currents underestimate the data at the higher ω values by about a factor of two. No strong influence of the energy transfer on the contribution of MECs is seen. The contribution of the Δ isobar in the calculation was performed within the 'static' approximation, which does not incorporate the propagation and decay width of the Δ isobar. Calculations of the ^{16}O(γ, pn) cross section and of exclusive deuteron electrodisintegration at high momentum have shown that such an approximation leads to a sizeable underestimation of the strength in the Δ resonance region and lack of resonant behaviour in the calculated cross section.

At higher neutron momentum values, data and theoretical predictions differ up to a factor of five for all values of ω. Within the range of energy transfer values probed in this experiment, the high p_m domain is expected to be strongly influenced by contributions from intermediate Δ excitation in the proton-neutron pair. The magnitude of the isobar contribution to the cross section depends on the invariant mass of the system involved, which for the pn pair in this experiment amounts to approximately 2150 MeV/c^2, which corresponds to the position of the resonance in deuteron electrodisintegration. A further indication for the importance of intermediate Δ excitation as a process contributing to the ^{3}He$(e, e'pp)$ cross section in the p_m domain above 100 MeV/c was seen in the dependence of the cross section on the forward proton emission angle γ_1. The strong increase of the cross section with increasing γ_1 reflects the angular dependence of intermediate Δ excitation as seen in calculations of the ^{16}O(γ, pn) cross section and of coherent π^0 photoproduction.

Comprehensive treatment of the Δ degree-of-freedom within the continuum Faddeev framework is therefore necessary before quantitative conclusions can be drawn from the data measured at high p_m or high ω values.

The continuum Faddeev calculations account for rescattering effects among the outgoing nucleons via a multiple-scattering series based on realistic NN potentials. Within specific regions of phase space, where two nucleons are emitted with comparable momentum vectors, these rescattering processes strongly influence the cross section. Data from such specific 'FSI configurations' therefore provide a good tool to check the calculations in this respect.

For a pn 'FSI configuration' in the kinematic setting at $\omega = 220$ MeV and $q = 445$ MeV/c good agreement between data and calculations as a function of the pn momentum difference was found. Data obtained at ω=275 MeV and q=375 MeV/c confirmed this result, although the absolute magnitude of the cross section is underestimated, probably due to lack of isobar contributions in the current operator.

Information on the wave function of ^{3}He may be obtained in the domain $\omega \approx 220$ MeV and $p_m < 100$ MeV/c, if a direct knockout mechanism and coupling to one specific proton is assumed. Calculations indicate that, within the acceptance of this experiment, the cross section is dominated by coupling of the photon to the forward proton, which implies that, in absence of rescattering, the nucleon momenta in the initial state can be reconstructed. This suggests a presentation of the cross section as a function of the observable $p_{diff,1}$, which can be related to the relative momentum of the constituents of the two-proton pair in the initial state. The observed decrease of the cross section as a function of this relative momentum reflects the behaviour of the wave function and is well reproduced by calculations at low p_m. Although calculations performed with different models of the NN interaction, lead to different predictions of the slope and magnitude of the cross section in this domain. The statistical and systematic uncertainty of the data, as well as the sizeable changes induced in the predictions by the MECs and (yet unknown) isobar contributions, do not permit to express preference for any one of the potential models considered.

Larger differences between the wave functions calculated from the various NN potentials are observed at high centre-of-mass momentum values and for relative momenta above 400 MeV/c per nucleon. In order to be able to draw quantitative conclusions on the details of the NN interaction from $^3\mathrm{He}(e,e'pp)$ data, more high accuracy data should be obtained in the region of direct two-proton knockout over a larger range in pp relative momenta. Increase of the momentum transfer may further reduce the influence of isobar currents and rescattering, although it should be noted that this will lead to more severe problems with regard to the available calculations, which are performed in a non-relativistic framework. Also the investigation of the high p_m region offers possibilities, as in this region larger differences between the wave functions calculated with the various potential models exist. However, this awaits either a better theoretical treatment of the high p_m domain, or experimental means to isolate the contribution of isobar currents to the cross section. In this respect separation of the $^3\mathrm{He}(e,e'pp)$ cross section in its contributing structure functions and an investigation of the complementary reaction $^3\mathrm{He}(e,e'pn)$ will provide valuable information for better understanding the processes involved.

References

[Amr94] A. Amroun *et al.*, *Nucl. Phys.* A579 (1994) 596.

[Aud89] G. Audit *et al.*, *Phys. Lett. B* 227 (1989) 331.

[Aud91] G. Audit *et al.*, *Phys. Rev. C* 44 (1991) R575.

[Aud97] G. Audit *et al.*, *Nucl. Phys.* A614 (1997) 461.

[Bec90] D.H. Beck, *Phys. Rev. Lett.* 64 (1990) 268.

[Blo98] K.I. Blomqvist *et al.*, *Phys. Lett. B* 424 (1998) 33.

[Bof96] S. Boffi *et al.*, *Electromagnetic Response of Atomic Nuclei*, Clarendon Press, Oxford 1996.

[Car98] J. Carlson and R. Schiavilla, *Rev. Mod. Phys.* 70 (1998) 743.

[Dis84] J.H.J. Distelbrink *et al.*, *Nucl. Instr. and Meth. Phys. Res.* 220 (1984) 443.

[Duc93] J.E. Ducret *et al.*, *Nucl. Phys.* A553 (1993) 697c.

[Emu94a] T. Emura *et al.*, *Phys. Rev. Lett.* 73 (1994) 404.

[Emu94b] T. Emura *et al.*, *Phys. Rev. C* 49 (1994) R597.

[Flo99] R.E.J. Florizone *et al.*, *Phys. Rev. Lett.* 83 (1999) 2308.

[For83] T. de Forest, Jr., *Nucl. Phys.* A392 (1983) 232.

[Gea94] *GEANT Detector Description and Simulation Tool*, version 3.21/94b, CERN Program library 1993.

[Giu91] C. Giusti and F.D. Pacati, *Nucl. Phys.* A535 (1991) 573.

[Glö83] W. Glöckle, *The Quantum Mechanical Few-Body Problem*, Springer-Verlag 1983.

[Glö96] W. Glöckle *et al.*, *Phys. Rep.* 274 (1996) 107.

[Gol95] J. Golak *et al.*, *Phys. Rev. C* 51 (1995) 1638.

[Golth] J. Golak, Ph.D. thesis Jagellonian University Cracow, 1995.

[Golpc] J. Golak, private communication.

[Hos89] N. d'Hose *et al.*, *Phys. Rev. Lett.* 63 (1989) 856.

[Isb94] V. Isbert *et al.*, *Nucl. Phys.* A758 (1994) 525.

[Ish94] S. Ishikawa *et al.*, *Il Nuovo Cimento* 107A (1994) 305.

[Jan87] E. Jans *et al.*, *Nucl. Phys.* A475 (1987) 687.

[Kas97] W.-J. Kasdorp, *Deuteron electrodisintegration at large momentum values*, Ph.D. thesis Universiteit Utrecht 1997.

[Kei85] P.H.M. Keizer *et al.*, *Phys. Lett. B* 157 (1985) 255.

[Kei87] P.H.M. Keizer *et al.*, *Phys. Lett. B* 197 (1987) 29.

[Kes95] L.J.H.M. Kester *et al.*, *Phys. Rev. Lett.* 74 (1995) 1712.

[Kwa91] E. Kwakkel *et al.*, *Detector Arm Readout Transputer module (DART), Crate-readout module for the Hadron-AmPS Digitizers*, DIGEL group, NIKHEF-K 1991.

[Koc83] J.H. Koch and E.J. Moniz, *Phys. Rev. C* 27 (1983) 751.

[Kol96] N.R. Kolb *et al.*, *Phys. Rev. C* 54 (1996) 2175.

[Lag85] J.M. Laget, *Nucl. Phys.* A446 (1985) 489c.

[Lag87] J.M. Laget, *Phys. Rev. C* 35 (1987) 832.

[Lappc] L. Lapikás, private communication.

[Lee96] J.J. van Leeuwe, *Investigation of nucleon-nucleon correlations in* ^{4}He, Ph.D. thesis Universiteit Utrecht 1996.

[LeG97] J.M. Le Goff *et al.*, *Phys. Rev. C* 55 (1997) 1600.

[Lin92] A. van der Linden *et al.*, *80 kV Electrostatic Wire Septum for AmPS*, contribution to the 3rd European Particle Accelerator Conference, Berlin, March 1992.

[LiO88] J.W. Lightbody Jr. and J.S. O'Connell, Computers in Physics 57 (1988).

[Mac89] R. Machleidt, *Adv. Nucl. Phys* 19 (1989) 189.

[Mac96] R. Machleidt, F. Sammarruca, Y. Song, *Phys. Rev. C* 53 (1996) R1483.

[Mac93] L. Machenil *et al.*, *Phys. Lett. B* 316 (1993) 17.

[Mar88] C. Marchand *et al.*, *Phys. Rev. Lett.* 60 (1988) 1703.

[Meij86] E. van Meijgaard and J.A. Tjon, *Phys. Rev. Lett.* 57 (1986) 3011.

[MoT69] L.W. Mo and Y.S. Tsai, *Rev. Mod. Phys.* 41 (1969) 205.

[Mul95] F.A. Mul, *HADRON3*, Technical Report Vrije Universiteit 1994.
F.A. Mul, *HADRON4*, Technical Report Vrije Universiteit 1995.

[Nog97] A. Nogga *et al.*, *Phys. Lett. B* 409 (1997) 19.

[Ond98a] C.J.G. Onderwater *et al.*, *Phys. Rev. Lett.* 81 (1998) 2213.

[Ond98b] C.J.G. Onderwater, *Investigation of short-range correlations using the* ^{16}O$(e, e'pp)$ *reaction*, Ph.D. thesis Vrije Universiteit Amsterdam 1998.

[Pel96] A.R. Pellegrino, *Deuteron Electrodisintegration in the* Δ*-resonance Region*, Ph.D. thesis Vrije Universiteit Amsterdam 1998.

[Pel99] A.R. Pellegrino *et al.*, *Nucl. Instr. and Meth. Phys. Res., Sect. A* 437 (1999) 188.

[Poo99] H.R. Poolman, *Quasifree Spin-dependent Electron Scattering from a Polarized* ^{3}He *Internal Target*, Ph.D. thesis Vrije Universiteit Amsterdam 1999.

[Ros97] G. Rosner, in *Proc. Conf. on Perspectives in Hadronic Physics*, Trieste 1997, ICTP/World Scientific, p. 185.

[Ryc94] J. Ryckebusch *et al.*, *Phys. Rev. C* 49 (1994) 2704.

[Sar93] A.J. Sarty *et al.*, *Phys. Rev. C* 47 (1993) 459.

[Sch97] M. Schroevers, *The QDQ aerogel Čerenkov detector and its usage in a* ^{16}O$(\gamma,\pi^- p)$ *experiment*, Master Thesis, Univesiteit Utrecht 1997.

[Sch89] R. Schiavilla *et al.*, *Phys. Rev. C* 40 (1989) 2294.

[Spa97] C.M. Spaltro, *Study of Electron-Induced Deuteron Knockout from* ^{3}He *and* ^{4}He, Ph.D. thesis Vrije Universiteit Amsterdam 1997.

[Spapc] C.M. Spaltro, private communication.

[Spa98] C.M. Spaltro *et al.*, *Phys. Rev. Lett.* 81 (1998) 2870.

[Sta99a] R. Starink *et al.*, submitted for publication to *Phys. Lett. B* .

[Sta99b] R. Starink, *Short-range correlations studied with the reaction* ^{16}O$(e,e'pp)^{14}$C, Ph.D. thesis Vrije Universiteit Amsterdam 1999.

[Sto94] V.G.J. Stoks *et al.*, *Phys. Rev. C* 49 (1994) 2950.

[Til87] D.R. Tilley *et al.*, *Nucl. Phys.* A474 (1987) 1.

[Tri96] C. Tripp *et al.*, *Phys. Rev. Lett.* 76 (1996) 885.

[Una91] O. Unal *et al.*, *Design considerations for experiment 91–10*, Internal report University of Wisconsin 1991.

[Ver96] J.C. Verkooijen, *Werking van de Fast-Time-Digitizer*, NIKHEF ETR 96–05.

[Vri84] C. de Vries *et al.*, *Nucl. Instr. and Meth. Phys. Res.* 223 (1984) 1.

[Vri87] H. de Vries, C.W. de Jager, C. de Vries, *At. Data Nucl. Data Tables* 36 (1987) 495.

[Vri90] L. de Vries *et al.*, *Nucl. Instr. and Meth. Phys. Res., Sect. A* 292 (1990) 629.

[Wilb96] Th. Wilbois, P.Wilhelm, H. Arenhövel, *Phys. Rev. C* 54 (1996) 3311.

[Wilh96] P. Wilhelm, J.A. Niskanen, H. Arenhövel, *Nucl. Phys.* A597 (1996) 613, *and Phys. Rev. Lett.* 74 (1995) 1034.

[Wir95] R.B. Wiringa, V.G.J. Stoks, R. Schiavilla, *Phys. Rev. C* 51 (1995) 38.

[Wit93] P.K.A. de Witt Huberts, *Nucl. Phys.* A553 (1993) 845c.

[Wri53] G.T. Wright, *Phys. Rev.* 91 (1953) 1282.

[Wu91] Y. Wu, *The Optical Design of AmPS*, Ph.D. thesis Technische Universiteit Eindhoven 1991.

[Zon94] A. Zondervan *et al.*, *Nucl. Instr. and Meth. Phys. Res., Sect. A* 342 (1994) 436.

[Zon95] A. Zondervan *et al.*, *Nucl. Phys.* A587 (1995) 697.

Samenvatting

Het belangrijkste deel van de sterke wisselwerking, die de kerndeeltjes – ook wel *nucleonen* genoemd – in de kern bij elkaar houdt, wordt gevormd door de kracht tussen twee individuele deeltjes. Deze nucleon-nucleon-wisselwerking (NN-wisselwerking) toont een karakteristiek gedrag: wanneer de afstand tussen de twee nucleonen groter is dan ongeveer 1 femtometer, is de kracht aantrekkend, terwijl deze op korte onderlinge afstand juist sterk afstotend is. Het gebruik van een dergelijke realistische NN-interactie in de berekening van kern-eigenschappen introduceert correlaties in de golffunctie van de kern.

Het gedrag van de NN-wisselwerking kan worden beschreven door middel van theoretische modellen met zeer diverse ingrediënten. Deze modellen worden getoetst aan experimentele resultaten op het gebied van vrije nucleon-nucleon-verstrooiing en aan de gemeten eigenschappen van het deuteron. Sinds kort zijn verscheidene theoretische modellen beschikbaar die deze gegevens beschrijven met een χ^2 per punt van ongeveer één. Deze modellen blijken echter verschillende voorspellingen te doen omtrent de kenmerken van drie-deeltjes-systemen, zowel ten aanzien van de eigenschappen van de begintoestand als ook omtrent de waarschijnlijkheden voor reacties, waarbij het drie-deeltjes-systeem in de eindtoestand niet meer intact is.

De ^{3}He$(e,e'pp)$ reactie is zowel geschikt om onderzoek te doen naar het mechanisme van de twee-proton uitstootreactie als om berekeningen te toetsen, die gebaseerd zijn op helium-3 golffuncties, berekend met verschillende potentiaalmodellen. Op basis van berekeningen, uitgevoerd met een numeriek exact model van de ^{3}He$(e,e'pp)$ werkzame doorsnede, zijn gebieden in de fase-ruimte aan te wijzen, waar de werkzame doorsnede vooral bepaald wordt door uitstoot van nucleonparen middels koppeling van een virtueel foton aan één nucleon. Dit wordt wel aangeduid met de benaming 'één-deeltjes stroom'. Bovendien kan uit deze berekeningen worden afgeleid dat het foton zich vooral koppelt aan het proton dat in voorwaartse richting wordt uitgezonden. In de eindtoestand maakt dit proton dan de kleinste hoek met de overgedragen drie-impuls. Hieruit volgt dat, in die gebieden waarin aan beide criteria is voldaan, de bepaling van de werkzame doorsnede van de ^{3}He$(e,e'pp)$ reactie de mogelijkheid opent om de golffunctie van het gebonden ^{3}He-systeem te bestuderen.

Er dient wel te worden opgemerkt, dat het mechanisme zoals boven beschreven niet als enige verantwoordelijk is voor de gemeten werkzame doorsnede. Koppeling van het virtuele foton aan mesonen (aangeduid met de uit het Engels afkomstige afkorting MEC, oftewel *meson-exchange currents*) en het aanslaan van de Δ-resonantie zullen ook aan de werkzame doorsnede bijdragen, hoewel hun belang in het geval van directe twee-proton-uitstoot beperkt is. Hun bijdrage neemt echter belangrijk toe als naar die gebieden wordt gekeken waarin het neutron een hoge impuls heeft. Door de overgedragen impuls en vooral de overgedragen energie van het virtuele foton te variëren, kan in een experiment het relatieve belang van beide bijdragen worden vastgesteld.

Op grond van bovenstaande argumenten volgt dat de ^{3}He$(e,e'pp)$ reactie bij uitstek geschikt is om onderzoek te doen naar NN-correlaties en stromen. In deze studie wordt een dergelijk experiment beschreven en worden de resultaten vergeleken met een theoretisch model op basis van de Faddeev-vergelijkingen. Binnen dit model zijn berekeningen uitgevoerd met verschillende modellen van de NN-wisselwerking.

Voor de uitvoering van dit experiment is gebruik gemaakt van de bijna continue elektronenbundel die geleverd wordt door AmPS, de 'Amsterdam Pulse Stretcher'. De energie van de inkomende elektronen was 564 MeV en de gemiddelde stroom lag tussen de 0,5 en 1,5 μA. Het gasvormige ^{3}He had een dikte van 270 mg/cm^2 en bevond zich in een cryogene hogedruk-cel. De verstrooide elektronen werden waargenomen in de QDQ magnetische spectrometer, terwijl de twee uitgestoten protonen gedetecteerd werden in HADRON detectoren. Laatstgenoemde detectoren zijn in hoge mate gesegmenteerd en dekken een grote ruimtehoek af. De werkzame doorsnede is gemeten voor drie waarden van de impuls-overdracht q, namelijk 305, 375 en 445 MeV/c. De energie overdracht ω door het virtuele foton was bij al deze metingen 220 MeV. Daarnaast werd bij q=375 MeV/c een reeks metingen uitgevoerd binnen een ω-bereik van 170 tot 290 MeV.

De gegevens zijn vergeleken met voorspellingen van het 'continuum-Faddeev'-model van Golak *et al.* In dit model wordt het effect van herverstrooiing van de uitgaande nucleonen volledig meegenomen. Als stroom-operator kan voor een één-deeltjes stroom worden gekozen, maar daarnaast kan ook de bijdrage ten gevolge van de uitwisseling van π- en ρ-mesonen worden meegenomen. Aangezien nog geen Lorentz-covariante-beschrijving mogelijk is voor de werkzame doorsnede, zijn de berekeningen, om hun interne consistentie niet te verstoren, geheel niet-relativistisch uitgevoerd. Wel zijn verschillende modellen voor de NN-wisselwerking gebruikt: er zijn berekeningen gedaan met de Bonn-B, CD ('ladingafhankelijk') Bonn, Nijmegen-93 en met de Argonne v_{18} interactie-modellen.

De gemeten $^3\text{He}(e,e'pp)$ werkzame doorsnede laat een sterke correlatie zien tussen de hoeken van beide uitgezonden protonen. De grotere uitstootwaarschijnlijkheid komt overeen met de emissie van twee protonen onder een hoek van 180° in hun massa-middelpunts systeem, waarbij het (ongedetecteerde) neutron met een lage impuls achterblijft. Dit vormt een aanwijzing voor 'directe' twee-proton uitstoot. De breedte van de gemeten verdeling is een gevolg van de impulsverdeling van het neutron. Weergave van de gemeten werkzame doorsnedes als functie van deze neutron-impuls p_m laat zien, dat de werkzame doorsnede exponentieel afvalt als functie van p_m.

In het neutronimpuls gebied onder de 100 MeV/c en voor een energie overdracht ruim onder het Δ-resonantiegebied, wordt de werkzame doorsnede voor het $^3\text{He}(e,e'pp)$-proces waarschijnlijk gedomineerd door directe uitstoot van gecorreleerde protonparen. In dit gebied is namelijk de bijdrage van MEC's en Δ-excitatie onderdrukt. Berekeningen, uitgevoerd met uitsluitend één-deeltjesstromen, geven een redelijk goede beschrijving van de gemeten werkzame doorsnede voor het p_m gebied onder 100 MeV/c bij ω=220 MeV en q=305 MeV/c. Bovendien laten metingen bij q=375 MeV/c een soortgelijke overeenkomst tussen meetresultaten en berekening zien. Daarbij kan nog worden opgemerkt dat berekeningen, waarin de bijdrage van MEC's is meegenomen, in dit p_m-gebied slechts een beperkte toename van de werkzame doorsnede te zien geven. Derhalve kan worden geconcludeerd dat, bij ω=220 MeV en $p_m \lesssim$ 100 MeV/c, de werkzame doorsnede door directe uitstoot van twee protonen middels een één-deeltjesstroom wordt gedomineerd. Bij hogere waarden van de neutronimpuls, in het gebied van 120 tot 320 MeV/c, verschillen de metingen en één-deeltjesberekeningen ongeveer een factor vijf. Bijdrage van MEC's verhogen de berekende sterkte in dit gebied met ten hoogste 35%.

De invloed van tussentijdse Δ-excitatie hangt af van de invariante massa van het systeem van de twee nucleonen en het foton. Om deze invloed te onderzoeken zijn metingen uitgevoerd voor waarden van de energie overdracht van 170 tot 290 MeV. Dit komt overeen met een bereik van 2055 tot 2120 MeV/c^2 in invariante massa $W_{p_1'p_2'}$, wanneer p_m onder de 100 MeV/c blijft. De gemeten werkzame doorsnede neemt binnen dit interval met 50% toe, waarschijnlijk als gevolg van het toegenomen belang van Δ-exitatie bij hogere energie overdracht. Theoretische voorspellingen waarin bijdragen van MEC en Δ-excitatie worden meegenomen, onderschatten de gemeten sterkte bij hogere ω waarden met een factor twee, waarbij de bijdrage van MEC's bijna onafhankelijk is van de energie overdracht.

Van belang is te vermelden dat de Δ-bijdrage in de berekeningen is uitgevoerd binnen de zogenaamde 'statische' benadering. Hierbij worden de propagatie van de Δ en zijn vervalbreedte binnen de kern verwaarloosd. Berekeningen van de ^{16}O(γ, pn) werkzame doorsnede hebben aangetoond dat dit leidt tot een belangrijke onderschatting van de Δ-bijdrage. Bovendien wordt het resonante gedrag van Δ-excitatie niet door dergelijke statische berekeningen gereproduceerd.

Voor alle waarden van ω blijkt er een verschil tussen de gemeten en de berekende werkzame doorsnede te bestaan bij hogere neutronimpulsen. Dit verschil kan oplopen tot ongeveer een factor vijf. Binnen het meetbare bereik van energie overdracht is het te verwachten dat dit hoge p_m-gebied sterk wordt beïnvloed door Δ-excitatie binnen proton-neutron-paren (pn-paren). Dit proces is afhankelijk van de invariante massa van het betreffende systeem, hetgeen voor de onderhavige pn paren neerkomt op circa 2150 MeV/c^2. Deze massa komt overeen met de positie van de Δ-resonantie in de werkzame doorsnede voor deuteron-elektrodesintegratie.

Een andere aanwijzing voor het belang van de Δ-bijdrage in het p_m-gebied boven 100 MeV/c vormt de afhankelijkheid van de werkzame doorsnede van de hoek van het voorwaarts uitgezonden proton. De snel toenemende werkzame doorsnede voor grotere hoeken lijkt een weerspiegeling van de hoekafhankelijkheid van Δ-excitatie, zoals gezien wordt in berekeningen van de ^{16}O(γ, pn) werkzame doorsnede en van coherente pion-fotoproductie.

Het is derhalve noodzakelijk dat het raamwerk van de 'continuum-Faddeev'-vergelijkingen wordt uitgebreid met een volledige beschrijving van Δ-excitatie.

Pas daarna kunnen kwantitatieve conclusies worden getrokken omtrent de gemeten werkzame doorsnedes bij hoge p_m of hoge ω.

In de 'continuum-Faddeev'-berekeningen wordt herverstrooiing tussen de uitgaande nucleonen volledig meegenomen. De berekeningen zijn gebaseerd op een zogenaamde verstrooiings-reeks die herhaalde interacties tussen de nucleonen omvat, waarbij gebruik wordt gemaakt van realistische modellen van de NN-interactie. In kinematische gebieden waar twee nucleonen met vergelijkbare impuls worden uitgezonden, zijn herverstrooiingsprocessen de dominante factor die de werkzame doorsnede beïnvloeden. Dergelijke gebieden worden aangeduid als 'FSI-configuraties', naar de Engelse term voor eindtoestands-wisselwerking: *Final State Interaction.* Metingen rond 'FSI-configuraties' zijn derhalve een goed middel om de beschrijving van herverstrooiing in de berekeningen te testen.

In het gemeten deel van de fase-ruimte voor ω=220 MeV en q=445 MeV/c komt een 'FSI configuratie' voor tussen het voorwaarts uitgezonden proton en het neutron. In dit gebied blijkt een goede overeenkomst tussen meetresultaten en de berekening te bestaan. Ook gegevens verzameld bij ω=275 MeV en q=375 MeV/c laten overeenkomst tussen de vorm van de gemeten werkzame doorsnede en de berekening zien, hoewel in dit gebied de absolute sterkte door de berekening zeer wordt onderschat. Dit is waarschijnlijk het gevolg van het ontbreken van Δ-excitatie in de gebruikte stroom-operator.

Informatie over de golffunctie van ^{3}He kan in beginsel uit de $(e, e'pp)$-reactie worden verkregen, wanneer een direct uitstoot-mechanisme via een één-deeltjesstroom en koppeling aan één specifiek proton wordt aangenomen. In het onderhavige experiment geldt dit voor het gebied bij $\omega \approx$ 220 MeV en voor $p_m <$ 100 MeV/c. Berekeningen geven aan dat, binnen de grenzen van dit experiment, de werkzame doorsnede gedomineerd wordt door koppeling aan het voorwaarts uitgezonden proton. Hierdoor kunnen de impulsen van de nucleonen in de begintoestand worden teruggerekend, mits wordt aangenomen dat herverstrooiing in dit gebied verwaarloosd mag worden. In dat geval kan het nuttig zijn de werkzame doorsnede weer te geven als functie van de observabele $p_{\mathit{diff},1}$, daar deze grootheid gerelateerd kan worden aan de relatieve impuls van de nucleonen van het geraakte paar in de begintoestand.

De gemeten werkzame doorsnede laat, bij $p_m <$ 100 MeV/c, als functie van $p_{\mathit{diff},1}$ een dalende trend zien, hetgeen een afspiegeling vormt van de golffunctie. Deze trend wordt goed gereproduceerd door de ‘continuum-Faddeev’-berekeningen. Berekeningen, uitgevoerd met diverse modellen van de NN-interactie, geven verschillende voorspellingen omtrent zowel grootte als helling van de werkzame doorsnede in dit gebied. De invloed van de MEC-bijdrage op de werkzame doorsnede is echter groot en de bijdrage van Δ-excitatie nog onduidelijk. Daarbij is, op dit moment, de statistische en systematische onzekerheid van de gemeten werkzame doorsnede nog aanzienlijk. Het is derhalve nog niet mogelijk een voorkeur uit te spreken voor een van de interactie-modellen.

De berekeningen met diverse interactie-modellen laten zien dat er grotere verschillen tussen de golffuncties bestaan bij hogere waarden voor de massa-middelpuntsimpuls en voor relatieve impulsen hoger dan 400 MeV/c per nucleon. Om uit de ^{3}He$(e,e'pp)$-gegevens kwantitatieve conclusies te kunnen trekken omtrent details van de NN-interactie, zullen metingen gedaan moeten worden over een groter bereik in pp relatieve impuls, maar wel binnen het kinematisch gebied waar de werkzame doorsnede door directe twee-protonuitstoot wordt gedomineerd. Gebruik van hogere impulsoverdracht kan hierbij behulpzaam zijn, aangezien dit leidt tot een vermindering van het belang van Δ-excitatie en tot minder herverstrooiingseffecten. Dit leidt echter tot problemen met de huidige berekeningen, die in een niet-relativistisch raamwerk worden uitgevoerd.

Ook de studie van het hoge p_m-gebied biedt nog mogelijkheden, hoewel op dit moment nog geen goede theoretische beschrijving hiervan mogelijk is. Berekeningen laten zien dat de invloed van het interactie-model op de golffunctie hier groot is. Het is echter vooral noodzakelijk dat er ofwel verbeterde theoretische modellen komen, ofwel dat een experimentele methode wordt gevonden om de bijdrage van Δ-excitatie aan de werkzame doorsnede in dit gebied te bepalen. Meer experimentele gegevens, in het bijzonder een ontbinding van de ^{3}He$(e,e'pp)$-werkzame-doorsnede in de bijdragende structuurfuncties en studie van de complementaire reactie ^{3}He$(e,e'pn)$, zijn van groot belang. Zij kunnen meer licht werpen op de processen die aan twee-nucleon-uitstoot ten grondslag liggen en leiden tot een beter begrip van nucleon-nucleon-correlaties.

Nawoord

De beperkte omvang van dit proefschrift staat in geen verhouding tot de hoeveelheid werk die door zoveel mensen in de uitvoering en verwerking van het experiment is gestoken. Aan al diegenen die – bewust of onbewust – hun essentiële bijdrage hebben geleverd aan het succes van dit experiment en aan hen, die de afgelopen jaren tot een onvergetelijke tijd voor mij hebben gemaakt, is dit nawoord gericht.

Beste Eddy, je begeleiding in deze jaren heb ik enorm gewaardeerd. Je stond altijd klaar om vragen en problemen te bediscussieren van allerlei soort, waar niet alleen het onderzoek maar ook ikzelf veel aan heb gehad. Ook hebben je enthousiasme en je manier van samenwerken mijn verblijf tot een bijzonder leuke en aangename tijd gemaakt. Voor alles: bedankt!

Beste Peter, met bewonderenswaardige snelheid en precisie heb je steeds mijn manuscripten doorgelezen. Jouw brede benadering en je aandacht voor de juiste balans hebben bijgedragen aan de algehele begrijpelijkheid van dit werk. Bedankt voor de bijdrage die je aan dit proefschrift geleverd hebt.

Beste Gerco en Ronald, de enthousiaste ontvangst die ik van jullie kreeg als student heeft er mede toe geleid dat jullie vier jaar aan mij vast zaten. Met veel plezier denk ik terug aan de discussies, de etentjes, de dot-war's en de uitdagingen en aan alle tijd die we, aan deze en gene zijde van de grote plas, hebben doorgebracht. Ik zal de herinnering aan het triple-point niet snel vergeten.

Beste Willem, je bijdrage aan de HADRON- en triple-experimenten valt niet te onderschatten. Jouw enthousiasme voor het onderzoek, waarmee ik zowel tijdens mijn afstudeertijd als ook later veelvuldig heb mogen kennismaken, heb ik enorm gewaardeerd.

Beste Antonio, Jeff, Jos, Koos, Martijn en Willem, jullie bijdragen hebben een reeks van HADRON experimenten tot een groot succes gemaakt. De bijzonder prettige sfeer die er altijd heerste heeft hierbij een voorname rol gespeeld. Beste Frans, jij en je collega's van de VU verdienen bewondering voor het op de meest vreemde tijdstippen komen verslepen, verbouwen en verbeteren van hadronen.

Dear Jacek and Walter, your contributions to the interpretation of this work have been many. I would like to thank you for all useful discussions and the almost instantaneous responses to my ever increasing requests for calculations. Without your calculations interpretation of these measurements would have been impossible.

Beste Louk, hartelijk dank voor je inzet bij alle elastische analyses en het begrijpelijk maken van de spectrometer analyse. Beste Henk, van je inzicht in electronenverstooiing heb ik veel geleerd.

Graag wil ik ook de leden van de beoordelingscommissie, Jo van den Brand, John Tjon en Jos Engelen, bedanken voor de tijd die zij in het lezen van het manuscript hebben gestoken en voor de waardevolle suggesties.

It takes a lot of people to get or keep an experiment running smoothly over a period of weeks. To those who made it happen, Andrew, Dave, David, Eddy, Evaristo, Franco, George, Guido, Hans, Henk, Larry, Lello, Louk, Marcel, Martijn, Mauro, Peter, Roberto, Ronald, Salvatore, Thomas and Willem: thanks!

Dank ook aan alle versneller technici, en aan Ber Kuijer in het bijzonder, voor de inspanningen om het laatste EMIN seizoen tot (een van) de beste te maken. Herman en Jan, de bundel die jullie voor dit experiment hebben neergezet is het beste bewijs dat het stoppen van het stretcherbedrijf te vroeg gekomen is. Bedankt voor de vele onaangekondigde bezoeken, nachtelijke sessies en de hands-on cursus versneller- en ringtechniek. Gert-Jan en Rob, bedankt voor jullie bijdragen aan het ontwerpen respectievelijk installeren van het cryotarget. Cocky, zonder jouw inventiviteit en hulpvaardigheid had ik niet zo'n originele targetcontructie gehad en had er bovendien geen spectrometer meer recht gestaan.

Beste Alex, Bas, Eric, Joke, Kees, Natalia, Paul, Ronald, Ruud, Tom en Wim, bedankt voor alle hulp en de leuke tijd, al dan niet achter een scherm. Ronald, je bijzondere bijdrage aan dit werk is van essentieel belang geweest. Ook daarvoor: bedankt! Ook dank aan alle (digitale) electronici en in het bijzonder Albert, Ed, Henk en Jelle.

Beste Jochen, bedankt voor het verlevendigen van koffie- en lunchdiscussies, het verspreiden van zowel Xblast als buitenaards leven en voor het doorlezen van de bèta-versie van dit boekje. Beste Martijn, bedankt voor het leveren van de eerste levensbehoefte. Beste Marcel, als theemeester heb je een mooie traditie in ere gehouden. Ook alle andere spare-ribs eters en China-experts: Chiara en Hans, Marco, Willem en Karin: bedankt. Dear Pablo, I hope you will enjoy your time here as much as I did mine. That your follow-up to the series of $(e, e'NN)$ experiments may be as successful as all previous ones.

Ook André, Bart, Benno, Dirk-Jan, Doug, Ed, Egbert, Elise, Elke, Elly, Erik, Eveline, Gail, Gerard, Hans-Roeland, Hans, Henk-Jan, Igor, Irene, Joppie, Jo, Kees, Laurens, Maria, Massi, Maurice, Muhsin, Niels, Piet, Pim, Rainer, Rinus, Robert, Rob, Rosella, Tancredi, Tjeerd, Wim, alsmede iedereen die ik niet hier genoemd maar wel gewaardeerd heb, van harte bedankt!

Gelukkig zijn er ook mensen geweest die me er zo af en toe aan herinnerden dat er ook buiten de fysica nog een wereld was. Jullie goede adviezen, zoals omtrend het eten van groene groenten, heb ik misschien niet altijd ter harte genomen, maar wel gewaardeerd.

Mijn ouders hebben op meer manieren aan dit werk bijgedragen dan in enkele woorden valt uit te drukken. Jullie steun, letterlijk en figuurlijk, bij dag en (soms) bij nacht, jullie voortdurende interesse en jullie aanmoediging, het heeft ook de afgelopen jaren tot een leuke tijd gemaakt. Hiervoor, en voor al dat andere dat verder ongenoemd zal blijven, hartelijk dank.

Sommige dingen zijn niet te beschrijven – en al helemaal niet in de beperkte ruimte van een dankwoord. Lieve Marianne, voor alles en nog veel meer, bedankt; de komende jaren worden minstens net zo leuk.

Curriculum vitae

De auteur werd geboren op 6 september 1973 te Zaandam. Na zijn schooltijd aan het Murmellius Gymnasium te Alkmaar, afgesloten met het behalen van het diploma Gymnasium-B, begon hij in 1990 de studie Natuurkunde aan de Vrije Universiteit te Amsterdam. Hierin legde hij de nadruk op de experimentele fysica en de natuurkundige informatica. Tijdens zijn afstudeer-stage in 1995 aan het Nationaal Instituut voor Kernfysica en Hoge-Energie Fysica (NIKHEF) te Amsterdam ontwikkelde hij een geautomatiseerde inregelprocedure voor de instellingen van de HADRON trigger electronica. In april 1995 sloot hij de studie cum laude af met het behalen van het doctoraal diploma Experimentele Natuurkunde met aantekening Natuurkundige Informatica. Aansluitend verrichtte de auteur het in dit werk beschreven onderzoek aan het NIKHEF.